Harmonics Retrieval for Sensorless Control of Induction Machines

Binying Ye

SPIM

Thèse de Doctorat

école doctorale **sciences pour l'ingénieur et microtechniques**

UNIVERSITÉ DE TECHNOLOGIE BELFORT-MONTBÉLIARD

THÈSE présentée par

Binying YE

pour obtenir le
Grade de Docteur de
l'Université de Technologie de Belfort-Montbéliard
Spécialité : Génie électrique

HARMONICS RETRIEVAL FOR SENSORLESS CONTROL OF INDUCTION MACHINES

le 16 février 2015

Soutenue le devant le Jury :

Prof. Patrice Wira	Rapporteur	Université de Haute Alsace
Prof. Pericle Zanchetta	Rapporteur	University of Nottingham
Prof. Hamid Gualous	Examinateur	Université de Caen Basse Normandie
Dr. Salah Lagrouche Maître de Conférences, HdR	Examinateur	Université de Technologie de Belfort-Montbéliard
Prof. Maurizio Cirrincione	Directeur de thèse	The University of the South Pacific, UTBM
Dr Giansalvo Cirrincione Maître de Conférences, HdR, IEEE SM	Co-directeur de thèse	University of Picardie Jules Verne
Dr. Marcello Pucci Senior Researcher, IEEE SM	Co-directeur de thèse	ISSIA-CNR

ACKNOWLEDGEMENTS

I would like to express my most sincere gratitude to Professor Maurizio Cirrincione, for his guidance, advice and patience during the course of my study, without his brilliant and illuminating instructions on my research and even about the writing, this thesis could not have reached its present form. I wish also to acknowledge the assistant from my co-supervisors Dr. Marcello Pucci of ISSIA-CNR and Dr. Giansalvo Cirrincione of University of Picardie Jules Verne, for their useful comments and strong theoretical suggestions, both on the machine drive as well as neural-based signal processing. Meanwhile, I am also very grateful to Dr. Gianpaolo Vitale of ISSIA-CNR for his great help and Dr. Angelo Accetta of ISSIA-CNR on his continued assistance with my experimental part.

I would further like to give my gratitude to the financial support from the program of China Scholarships Council (CSC) (2011008090), to ISSIA-CNR for the hardware access for the performance evaluation of the proposed algorithms, and to UTBM where I did my thesis.

Finally, I wish to take this opportunity to express my appreciation and thanks to all my friends for their emotional support. I would also like to thank my parents who provide me the mental support and encouragement to explore the unknowns. Thanks are especially due to Jiayin for her love.

Binying YE

Belfort, 2015

RÉSUMÉ

Les avantages de contrôle de la machine asynchrone sans capteur de vitesse sont les suivants : réduction de la complexité du matériel, moins d'exigences en termes d'entretien, coût moindre et une fiabilité accrue. Cette thèse propose l'utilisation d'un modèle harmonique plus élevée du moteur à induction qui prend en compte les effets de fente de rotor et son utilisation pour le calcul de la vitesse du rotor des moteurs à induction (IM). Elle se caractérise par une très faible sensibilité aux variations des paramètres.

La thèse étudie tout d'abord la relation entre les harmoniques à fentes du rotor (RSHs) et la vitesse du rotor instantanée. Pour suivre directement l'RSH, les exigences du système sont pleinement prises en compte.

Dans un deuxième temps, les travaux de thèse ont permis de développer un système sans capteur en fonction de boucle à verrouillage de phase (PLL): La largeur de bande centrale est réglée en ligne sur la base des valeurs de référence, des fréquences d'alimentation et de glissement prévues au convertisseur PWM, la PLL est réglée pour suivre le rotor de la machine à RSH sans la nécessité de toute injection de signal à haute fréquence, ni en rotation, ni de pulsation. Ce système d'estimation de vitesse, qui est approprié pour le contrôleur scalaire, avait été intégré avec le lecteur scalaire, conduisant à un simple calcul peu exigeant, à faible coût de l'entraînement de la machine à induction sans capteur à faible coût. Les résultats expérimentaux montrent que le système est en mesure de suivre la vitesse de la machine dans une plage de vitesse très étendue.

Enfin, un système sans capteur amélioré basé sur l'analyse de composant mineur (MCA) neurones est décrit. Selon la théorie de Pisarenko, il a été vérifié que le MC qui se trouve dans le sous-espace de bruit est orthogonale au sous-espace de signal, par conséquent, les fréquences de signal contenues dans l'entrée peuvent être calculées à partir d'un polynôme formé par la MC. Classiquement, ce qui nécessitera la décomposition propre encombrants, néanmoins, la méthode de neurones proposée dans cette thèse peut récupérer le MC de façon récursive avec moins de calculs et des performances améliorées d'erreur (la solution est sur un total de moins sens carré). En outre, l'estimateur de vitesse est appliquée

à l'entraînement scalaire avec vérification expérimentale, l'ensemble du système se comporte bien, et la méthode MCA renforcée par réseaux neuronaux a fourni un bon potentiel dans l'application des harmoniques récupérer.

Mot clés: moteurs à induction, entraînements électriques, PLL, analyse de composant mineur, extraction des harmoniques

ABSTRACT

The advantages of speed-sensorless IM drives are reduced hardware complexity, fewer maintenance requirements, lower cost and increased reliability. This thesis proposes the use of a higher harmonic model of the induction motor which takes into account the rotor slot effects and its use for the computation of the rotor speed of induction motors (IMs). It is characterized by a very low sensitivity to the parameters variations.

The thesis first studies the relation between the rotor slot harmonics (RSHs) and the instantaneous rotor speed. To directly track the RSH, the requirements of the system are fully addressed.

Second, the thesis presents a sensorless scheme based on phase-locked loop (PLL): The centre bandwidth is tuned on-line on the basis of the reference values of the supply and slip frequencies provided to the PWM converter, the PLL is tuned to track the machine rotor slotting harmonic without the need of any high frequency signal injection, neither rotating nor pulsating. This speed estimation scheme, which is suitable for the scalar controller, had been integrated with the scalar drive, leading to a simple, computationally not demanding, low cost sensorless IM drives. The experiment results show that the system is able to track the machine speed in a very wide speed range.

Finally, an improved sensorless scheme based on minor component analysis (MCA) neurons is described. According to the Pisarenko's theory, it has been verified that the MC which lies in the noise subspace is orthogonal to the signal subspace, thus, the signal frequencies contained in the input can be computed from a polynomial formed by the MC. Conventionally, this will require the bulky eigen-decomposition, nevertheless, the neural method proposed in this thesis can retrieve the MC recursively with less computation and improved error performance (the solution is of total least square meaning). Moreover, the speed estimator is applied to the scalar drive with experimental verification, the overall system is well behaved, and the MCA method enhanced by neural networks has provided a good potential in the application of harmonics retrieve.

Key words: induction motors, electrical drives, PLL, minor component analysis, harmonics retrieval

CONTENTS

LIST OF TABLES

LIST OF FIGURES

CHAPTER 1. INTRODUCTION

In high performance electrical drives with induction machine (IM) for traction applications, one of the key problems is the sensorless control of the speed and the position. The advantages of speed-sensorless IM drives are reduced hardware complexity, fewer maintenance requirements, lower cost and increased reliability. To replace the mechanical speed sensor, information on the rotor speed is extracted from measured stator currents and voltages at the motor terminals. Fundamental and anisotropy model based algorithms are used for this purpose [1-12]. They differ with respect to accuracy, robustness, and sensitivity against model parameter variations.

This research work explores the speed estimation algorithms based on tracking the rotor slot harmonics (RSHs) of the IM, which are created by machine anisotropy and directly related to the real-time rotor speed. Like the other anisotropy-model based approaches, they are independent of machine parameters, like stator and rotor resistances, yet no extra signal injection is required. Moreover, the proposed algorithms have been applied to a sensorless drive, showing a good behavior in a very wide speed range from rated speed down to 2% of the rated speed.

1.1 Sensorless Control of Induction Motors

Literature about sensorless control of IM drives is huge [1-37]. The sensorless techniques for IM can be mainly divided into two categories: methodologies based on fundamental models and methodologies based on anisotropies models, see fig. 1-1.

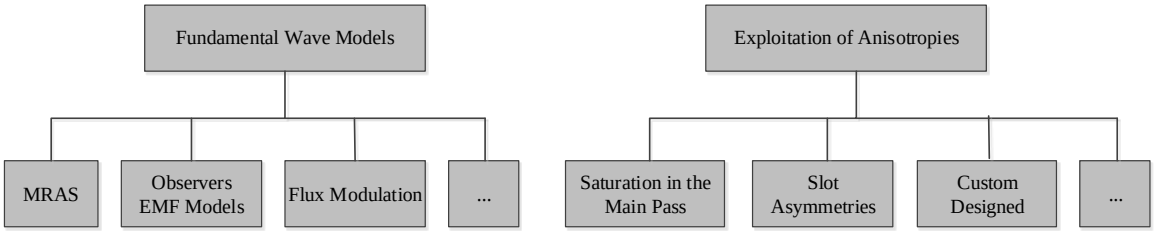

Fig 1-1 Classification of the sensorless control of machine

The former, such as model reference adaptive system (MRAS) and observers in the synchronous or stationary reference frame, present good results in the middle and high speed regions, but they suffer problem at low speeds where the back EMF fade out, and the IM becomes an unobservable system.

The latter have a better performance at very low and zero speed, they either exploit the magnetic saliency by signal injection, or exploit the use of PWM switching signals, and can be more efficient at low and zero speed than any other sensorless estimation due to its uncorrelated property with the machine parameter. Yet the latter tends to fail at increasing speed because of the necessary signal processing system (filtering etc.). In general, it can be stated that they can hardly be adopted at rated or close to rated speed.

Some typical methods belong within the two categories as described in the following:

1.1.1 Model-Based Sensorless Approach

1.1.1.1 Open-Loop Speed Estimators

Various rotor speed and slip speed open-loop estimators can be obtained by rewriting the stator and rotor equations of the IM. The accuracy of the algorithms is largely dependent on the machine parameters; however, due to their simplicity and robustness, some of them are also currently employed in commercial sensorless drives. In [1], five open-loop sensorless schemes are described, which are all based on the stator and rotor equations of the IM, differing from one another by the reference frame in which the equations are expressed. In practice, the choice among them is usually made according to the machine parameters at hand.

If the stator flux-linkage has been estimated, one straightforward way for speed estimation is to estimate the stator flux-linkage speed ω_{ms} and the slip speed ω_{sls} [1], and take the difference as follows:

$$\omega_r = \omega_{ms} - \omega_{sls} = \underbrace{\frac{\left(\psi_{sD} d\psi_{sQ}/dt - \psi_{sQ} d\psi_{sD}/dt\right)}{\left|\overline{\boldsymbol{\psi}}_s\right|^2}}_{\omega_{ms}} - \underbrace{\frac{L_s}{T_r}\frac{\sigma T_r di_{sy}^{\Psi_s}/dt + i_{sy}^{\Psi_s}}{\left|\overline{\boldsymbol{\psi}}_s\right| - \sigma L_s i_{sx}^{\Psi_s}}}_{\omega_{sls}} \tag{1.1a}$$

Or correspondingly, if the rotor flux-linkage has been estimated, then the rotor speed cab be obtained as the sum of the speed of the rotor flux (ω_{mr} relative to the stator) and the slip ω_{slr},

$$\omega_r = \omega_{mr} - \omega_{slr} = \underbrace{\frac{\left(\psi_{rd} d\psi_{rq}/dt - \psi_{rq} d\psi_{rd}/dt\right)}{\left|\overline{\boldsymbol{\psi}}_r\right|^2}}_{\omega_{mr}} - \underbrace{\frac{L_m(-\psi_{rq} i_{sD} + \psi_{rd} i_{sQ})}{T_r\left|\overline{\boldsymbol{\psi}}_r\right|^2}}_{\omega_{slr}} \quad (1.1b)$$

Where,

ψ_{sD}, ψ_{sQ} instantaneous values of the direct and quadrature axis stator flux linkages expressed in the stator reference frame

ψ_{rd}, ψ_{rq} instantaneous values of the direct and quadrature axis rotor flux linkages expressed in the rotor reference frame

$i_{sx}^{\Psi_s}, i_{sy}^{\Psi_s}$ instantaneous values of the direct and quadrature axis stator current expressed in the stator flux-oriented reference frame

L_m, L_s, L_r 3-phase magnetizing inductance, 3 phase total self-inductance of stator and rotor respectively

$\sigma = 1 - L_m^2/L_r L_s$ global leakage factor

$T_r = L_r/R_r$ rotor time constant

In (1.1a), the stator flux-linkage speed is obtained by taking the derivative of the stator flux-linkage angle θ_{ms}, with the division between the vector product of the stator flux-linkage vector and its derivative and the square of the stator flux amplitude itself. The slip speed (the speed of the stator flux-linkage space vector relative to the rotor) is obtained on the basis of the direct and quadrature components of the stator current in the stator flux-oriented reference frame. For this reason, a coordinate transformation is needed for this estimator. While in (1.1b), the rotor flux-linkage speed is obtained with the division between the vector product of the rotor flux-linkage vector and its derivative and the square of the rotor flux amplitude. The slip speed is obtained on the basis of the vector product of the rotor flux and the stator current vectors. The rotor flux linkage, however, is usually obtained from the stator flux linkage, and the stator flux linkages can be obtained by using monitoring stator currents and voltages. From (1.1), it can be known that the accuracy of the speed estimator depends greatly on the machine parameters, and the model used for the estimation of the rotor flux linkage.

The correct field orientation is affected by the accuracy in estimating the angles θ_{ms} or θ_{mr} that, depending on the open-loop flux estimation (see fig.1-2), suffer from both the integration problem and the sensitivity to the stator resistance variation. Many literature

papers refer improving the integration problem, i.e. the time derivation, parameter estimation [13-16]. At low stator frequency, in particular, a reduction of the speed estimation accuracy is to be expected in all these schemes due to a mismatch between the real and the estimated flux linkage caused by a wrong model of the stator resistance. The poor knowledge of the rotor time constant, on the contrary, mainly influences the estimation of the slip speed and therefore is critical at high loads.

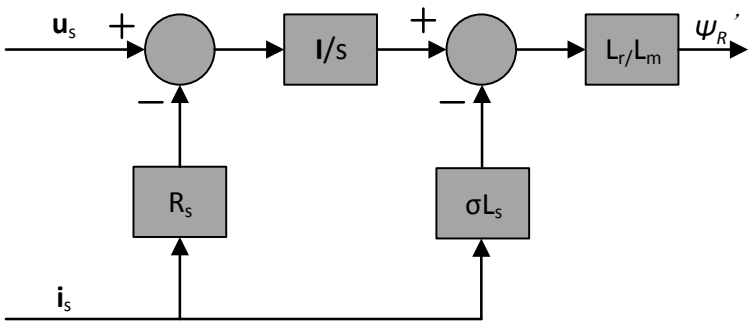

Fig 1-2 Basic structure for determination of the flux of the IMs

1.1.1.2 Model Reference Adaptive Systems

Both the steady-state and transient accuracy of the speed estimation can be significantly increased by adopting closed-loop speed estimation algorithms instead of the open-loop ones. An important category is that of MRASs (model referencing adaptive systems), in which an error vector is formed from the outputs of two models both dependent on different state variables of the IM. The error is driven to zero by an adaptation mechanism, through adjustment of a parameter that influences the adaptive model so that its output eventually coincides with that of the reference model.

In [10][17-21], several MRAS schemes have been developed. They differ from one another by the state variables being employed. Fig. 1-3 shows the basic scheme of a MRAS based speed estimator, in this case, the parameters to be estimated is the rotor speed ω_r. Some state variables, x_d, x_q(e.g. rotor flux-linkage components, ψ_{rd}, ψ_{rq}, or back e.m.f. components, e_d, e_q, etc.) of the induction machine, which are obtained by using measured quantities, are estimated in a reference model. Meanwhile, in the adjust model, the same state variables are estimated using the measured quantities and the rotor speed. The corresponding speed tuning signals ε are, respectively, $\varepsilon_\omega = \mathrm{Im}(\boldsymbol{\psi}'_r \hat{\boldsymbol{\psi}}'^{*}_r)$, $\varepsilon_e = \mathrm{Im}(\mathbf{e}\hat{\mathbf{e}}^{*})$, or

$\varepsilon_e = \mathrm{Im}[(\mathbf{e} - \hat{\mathbf{e}})\mathbf{i}_s^*]$: the quantities with '^' are related to the adaptive model and the '*' operator denotes the complex conjugate.

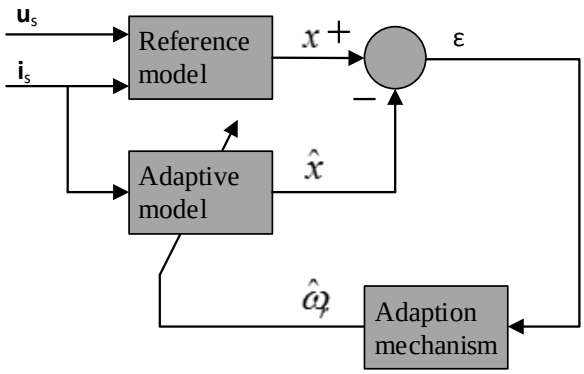

Fig 1-3 Basic MRAS-based speed estimator scheme

In designing the adaptation mechanism for a MRAS, it is important to take account of the overall stability of the system and to ensure that the estimated quantity will converge to the desired value with suitable dynamic characteristic. The appropriate adaptation law can be derived by the Popov's hyperstability criterion [1].

If the classic MRAS scheme based on the rotor flux error is considered, the reference model is described by the stator voltage equations in stator reference frame (DQ), re-written here for the sake of simplicity:

$$\begin{cases} \dfrac{d\psi_{rd}}{dt} = \dfrac{L_r}{L_m}(u_{sD} - R_s i_{sD} - \sigma L_s \dfrac{di_{sD}}{dt}) \\ \dfrac{d\psi_{rq}}{dt} = \dfrac{L_r}{L_m}(u_{sQ} - R_s i_{sQ} - \sigma L_s \dfrac{di_{sQ}}{dt}) \end{cases} \tag{1.2}$$

The adaptive model is based on the rotor equations in the stator reference frame, which is the so-called current model:

$$\begin{cases} \dfrac{d\hat{\psi}_{rd}}{dt} = \dfrac{1}{T_r}(L_m i_{sD} - \hat{\psi}_{rd} - \omega_r T_r \hat{\psi}_{rq}) \\ \dfrac{d\hat{\psi}_{rq}}{dt} = \dfrac{1}{T_r}(L_m i_{sQ} - \hat{\psi}_{rq} + \omega_r T_r \hat{\psi}_{rd}) \end{cases} \tag{1.3}$$

The differences between the state variables estimated, respectively, with the reference and adaptive models are fed to a speed tuning signal ε, and then processed by a PI (proportional integral) controller, whose output is the rotor speed. In this case, the speed is estimated as

$$\hat{\omega}_r = K_p(\psi_{rq}\hat{\psi}_{rd} - \psi_{rd}\hat{\psi}_{rq}) + K_i\int(\psi_{rq}\hat{\psi}_{rd} - \psi_{rd}\hat{\psi}_{rq})dt \tag{1.4}$$

Fig. 1-4 shows the block diagram of the classic MRAS scheme. The MRAS structure has numerous advantages: it is physically explicit and the PI controller in the adaptive loop is easy to design for a given estimation bandwidth. The result is accurate except for very low speeds when the voltage-model-derived flux vector becomes inaccurate.

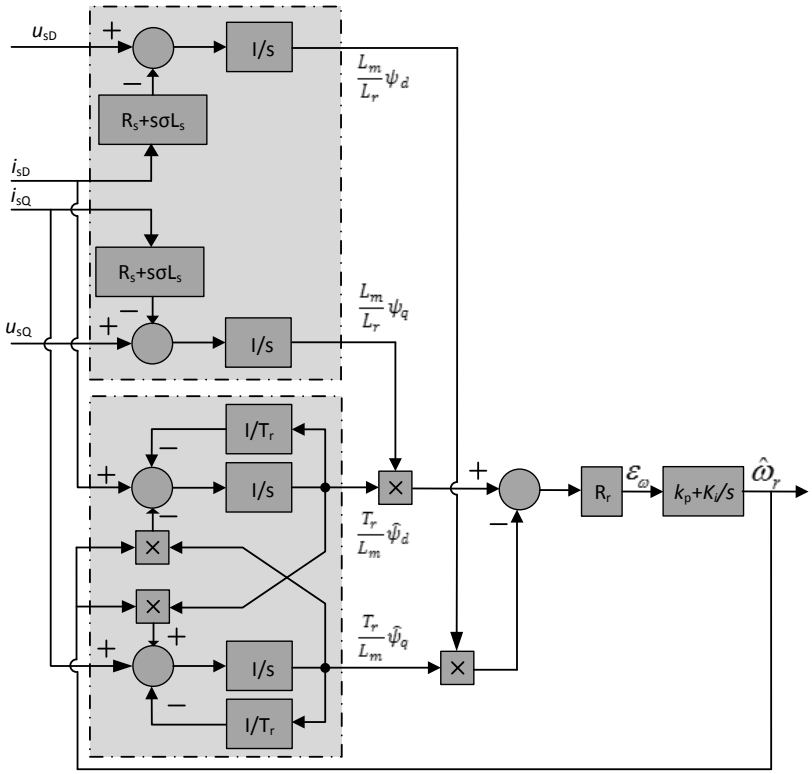

Fig 1-4 Block diagrams of MRAS based on rotor flux error.

However, like the open-loop estimators, the MRASs depend on the stator machine model: the block diagrams of the reference and adaptive models clearly highlight that the reference model suffers from the open-loop integration problem: this problem was addressed in [17] by adopting an LPF (Low Pass Filter) instead of a pure integrator, which causes, however, a poor flux amplitude and angle estimation as well as a poor speed estimation at low frequency, around the cut-off frequency of the LPF (usually a few Hertz).

This consideration highly limits the minimum working speed of the drive and the correct field orientation, with consequent reduction of the torque performances at low speed. Alternative solutions to be adopted for the open-loop flux integration have been shown in [2], in particular the adaptive integration based on a linear neural network [22]. Furthermore, at low speeds, the stator voltage amplitude is small, thus an accurate value of the stator resistance is required by the model to have a satisfactory response.

Other attempts includes: A MRAS scheme based on the back emf error [10], where no integration is needed so that satisfactory performance can be achieved even at low speeds, with resulting wider bandwidth of the speed loop; A MRAS-based system with a linear ANN (artificial neural network) adaptive model [23] has been presented which enhances the stability. The closed-loop types of MRAS are described in [2] (p.282), where the characteristics of a closed-loop flux observer (CLFO) are integrated with those of an MRAS, including also a mechanical system model. In general, they improve the performance of the speed estimation while increasing the complexity of the observer.

1.1.1.3 Adaptive Observers

For the open-loop estimators and MRAS described in the previous sections, the limit of acceptable performance depends on how precisely the model parameters can be matched with the corresponding parameters in the actual machine. The robustness against parameter mismatch and signal noise, however, can be improved by employing an adaptive observer. The observer based method aims at providing a real-time estimation of the state variables of a system, using only the input and output signals, both of which are assumed to be known. They can further be classified into two categories: the one based on the deterministic model, such as the Luenberger observer [24], extended Luenberger observer [25], and sliding model observer [26]; the other based on stochastic theory, such as Kalman filter and extended Kalman filter [27].

If the stator current and the rotor flux-linkage space-vectors are chosen as state variables, the state equations of the IM in the stationary reference frame can be written as [2]

$$\frac{d}{dt}\begin{bmatrix}\mathbf{i}_s \\ \boldsymbol{\psi}_r'\end{bmatrix} = \frac{d\mathbf{x}}{dt} = \begin{bmatrix}\mathbf{A}_{11} & \mathbf{A}_{12} \\ \mathbf{A}_{21} & \mathbf{A}_{22}\end{bmatrix}\begin{bmatrix}\mathbf{i}_s \\ \boldsymbol{\psi}_r'\end{bmatrix} + \begin{bmatrix}\mathbf{B}_1 \\ 0\end{bmatrix}\mathbf{u}_s = \mathbf{A}\mathbf{x} + \mathbf{B}\mathbf{u}_s \tag{1.5}$$

$$\mathbf{i}_s = \mathbf{C}\mathbf{x} \tag{1.6}$$

Where

$$\begin{cases} \mathbf{A}_{11} = -\{R_s/(\sigma L_s) + (1-\sigma)/(\sigma T_r)\}\mathbf{I} \times a_{11} \\ \mathbf{A}_{12} = L_m/(\sigma L_s L_r)\{(1/T_r)\mathbf{I} - \omega_r \mathbf{J}\} = a_{12}\{(1/T_r)\mathbf{I} - \omega_r \mathbf{J}\} \\ \mathbf{A}_{21} = \{L_m/T_r\}\mathbf{I} = a_{21}\mathbf{I} \\ \mathbf{A}_{22} = -(1/T_r)\mathbf{I} + \omega_r \mathbf{J} = a_{22}\{(1/T_r)\mathbf{I} - \omega_r \mathbf{J}\} \\ \mathbf{B}_1 = 1/(\sigma L_s)\mathbf{I} = b\mathbf{I} \end{cases} \quad (1.7)$$

With

$$\mathbf{i}_s = \begin{bmatrix} i_{sD} & i_{sQ} \end{bmatrix}^T,\ \mathbf{u}_s = \begin{bmatrix} u_{sD} & u_{sQ} \end{bmatrix}^T,\ \boldsymbol{\psi}_r^{'} = \begin{bmatrix} \psi_{rd} & \psi_{rq} \end{bmatrix}^T,$$

$$\mathbf{C}^{'} = \begin{bmatrix} \mathbf{0} & \mathbf{I} \end{bmatrix}, \mathbf{C} = \begin{bmatrix} \mathbf{I} & \mathbf{0} \end{bmatrix},\ \mathbf{I} = \begin{bmatrix} 1 & 0 \\ 0 & 1 \end{bmatrix},\ \mathbf{J} = \begin{bmatrix} 0 & -1 \\ 1 & 0 \end{bmatrix}$$

In the above state representation, $\mathbf{x} = \begin{bmatrix} \mathbf{i}_s, \boldsymbol{\psi}_r^{'} \end{bmatrix}$ is the state vector, composed of the stator current and rotor flux-linkage direct and quadrature components in the stationary reference frame, $\boldsymbol{u}_s$ is the input vector composed of the stator voltage direct and quadrature components in the stationary reference frame, **A** is the state matrix (4 × 4 matrix) depending on the rotor speed ω_r, **B** is the input matrix, and finally **C** is the output matrix.

The observer can be established by adding an error compensator to the machine model. If a full-order Luenberger observer is considered, the state observer estimates the stator current and the rotor flux, involving only the error vector on the stator current between the measured and model output one, $e_{rr} = (\mathbf{i}_s - \hat{\mathbf{i}}_s)$, as given in the following:

$$\frac{d\hat{\mathbf{x}}}{dt} = \hat{\mathbf{A}}\mathbf{x} + \mathbf{B}\mathbf{u}_s + \mathbf{G}(\hat{\mathbf{i}}_s - \mathbf{i}_s) \quad (1.8)$$

Where '^' means the estimated values, **G** is the observer gain matrix which is designed so that the observer is stable [2]. The speed signal $\hat{\omega}_r$ is required to adapt the matrix$\hat{\mathbf{A}}$.

The speed of IM, can be achieved by using a PI controller as

$$\hat{\omega}_r = K_p(e_\omega) + K_i \int (e_\omega) dt \quad (1.9)$$

Where the error term $e_\omega = \dfrac{d\hat{\omega}_r}{dt} = \dfrac{L_m}{\sigma L_s L_r}\left[\psi_{rq}(i_{sD} - \hat{i}_{sD}) - \psi_{rd}(i_{sQ} - \hat{i}_{sQ})\right]$ is the speed tuning signal found by utilizing Lyapunov's theorem [2].

The block diagram of the full-order Luenberger adaptive observer is shown in Fig. 1-5.

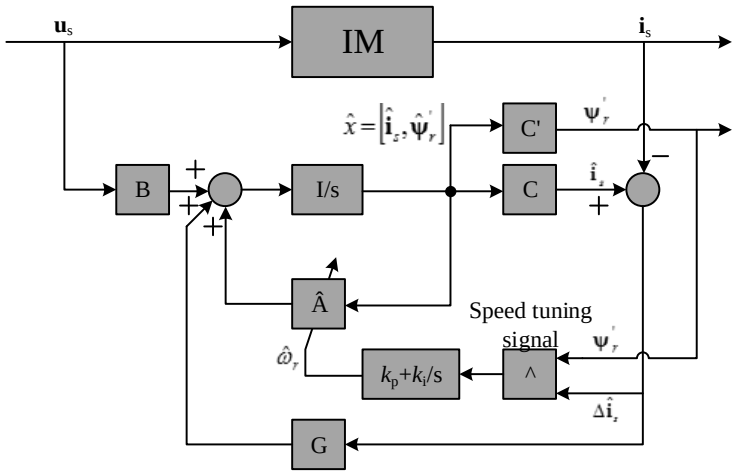

Fig 1-5 Block diagram of the full-order Luenberger adaptive observer

The full-order Luenberger observer based methods yield a reasonably accurate value for the speed. In general, the robustness against parameter mismatch and signal noise can be improved by employing stochastic observers for the estimation of the state variables, although the algorithm and design complexity are increased. Among them, the Kalman filter, although being computationally cumbersome, permits a joint estimation of state variables and parameter providing a better accuracy at low speed.

1.1.1.4 Limitations of Model-Based Approach

Most of the fundamental model based schemes involve estimating both flux and speed from the information available at the stator terminals, i.e., voltage and current. Such schemes will always be marginally stable for zero excitation frequency, when the back e.m.f. decreases to null or it is so low to be comparable with the voltage drop caused by the stator resistance: the speed then becomes unobservable at the stator terminals and the controllability at zero speed is expected only for a short time duration.

Furthermore, machine parameters are necessary for constructing the speed information, which means that the performance of all model-based speed estimators degrades under incorrect motor parameters. It is especially the stator resistance that determines the estimation accuracy of the stator flux vector. Although a correct initial value of the stator resistance is easily identified during initialization, considerable variations of the resistance take place when the machine temperature changes at varying loads. Besides, the bad knowledge of the

rotor time constant influences the estimation of the slip speed and therefore is critical at high loads.

To further improve the performance of model-based methods, online parameter identification is required. Besides that, a more precise model of the PWM inverter and flux can improve the accuracy at low speed range.

1.1.2 Anisotropy-Based Sensorless Approach

1.1.2.1 Signal Injection

Signal injection methods exploit machine anisotropy properties that are not employed by the fundamental machine model. The injected signal usually excites the machine at a much higher frequency than the bandwidth of the machine, and generates flux linkages that close through the leakage paths in the stator and rotor, leaving the mutual flux linkage with the fundamental almost unaffected [28-33].

Manufactured cage IMs usually do not have the inherited rotor saliency like permanent magnet synchronous machines (PMSMs); The magnetic saliency, however, can be caused by many reasons, such as discrete rotor bars in a cage rotor [28,29], saturation effect of the leakage paths through the fundamental field [32][34]. Otherwise the saliency effect can also be enhanced by using a custom designed rotor so as to exhibit periodic variations of local magnetic or electrical characteristics within a fundamental pole pitch [30]. The interaction of the HF (high frequency) signal with the rotor magnetic saliency produces a rotor position dependent signal that can be tracked by a properly designed observer [31-34].

Considering the case of saturation-induced saliency, the maximum flux density occurs in the *d* axis of a field-oriented coordinate system. The fundamental field saturates the stator and rotor iron close to *d* region, and therefore produces a higher magnetic impedance to the local leakage paths, the stator and rotor currents in the conductors around the saturated *d*-region excite leakage fluxes having a dominating *q*-component. The total leakage inductance component $L_{\sigma q}$ then reduces, while the component $L_{\sigma d}$ of the unsaturated q axis remains unaffected, leading to $L_{\sigma q} < L_{\sigma d}$ [35]

$$L_{\sigma}^{X} = \begin{bmatrix} L_{\sigma d} & 0 \\ 0 & L_{\sigma q} \end{bmatrix} \tag{1.10}$$

Being defined with reference to a coordinate system (X) that rotates at the speed of anisotropy ω_x to be detected, the x axis coincides with the most saturated region.

To extract the speed information from the machine anisotropy, a poly-phase rotating carrier at pulsation ω_c is usually added to the fundamental voltage generated by the pulse-width modulation (PWM) system. The term is of the type,

$$\mathbf{u}_c = u_c e^{j\omega_c t} \tag{1.11}$$

where $\mathbf{u}_c$ is the amplitude of the revolving carrier.

The interaction of such a voltage component with the machine anisotropies causes the presence of a current space-vector $\mathbf{i}_c$ at carrier frequency ω_c appearing as a component of the stator current space-vector $\mathbf{i}_s$. To compute the resulting current space vector $\mathbf{i}_c$, the carrier voltage has to be transformed into the same reference frame by multiplying it by exp(-$j\omega_x$),

$$u_c^X = u_c e^{j(\omega_c-\omega_x)t} = L_\sigma^X \frac{d\mathbf{i}_c^X}{dt} \tag{1.12}$$

This formula can be used to solve for $\mathbf{i}_c^X$, considering that $\omega_c \gg \omega_x$, this leads to the following solution:

$$\mathbf{i}_c^X = \frac{-ju_c}{2\omega_c L_{\sigma d} L_{\sigma q}}\left[(L_{\sigma d}+L_{\sigma q})e^{j(\omega_c-\omega_x)t} + (L_{\sigma d}-L_{\sigma q})e^{-j(\omega_c-\omega_x)t}\right] \tag{1.13}$$

which is then transformed back to the stationary reference frame

$$\mathbf{i}_c = \frac{-ju_c}{2\omega_c L_{\sigma d} L_{\sigma q}}\left[(L_{\sigma d}+L_{\sigma q})e^{j(\omega_c)t} + (L_{\sigma d}-L_{\sigma q})e^{j(-\omega_c-\omega_x)t}\right] = \mathbf{i}_p + \mathbf{i}_n \tag{1.14}$$

This result shows the existence of a current space vector $\mathbf{i}_\mathrm{p}$, rotating at carrier frequency ω_c in a positive direction, and a space vector $\mathbf{i}_\mathrm{n}$ that rotates at the angular velocity $\omega_c - 2\omega_x$ in a negative direction. This last component has the information on the speed ω_x of the anisotropy to be detected.

When carrier-signal excitation is used for sensorless control, the overall stator current consists of the fundamental current and the positive and negative sequence carrier signal currents. The separation of these components is necessary for both the fundamental current regulator operation and the extraction of the spatial information from the negative-sequence carrier signal. To be further processed by the speed estimation algorithm, the $\mathbf{i}_c$ component

is extracted by a heterodyning technique or a band-pass filter centred at the carrier frequency, which separates it from both the fundamental current component and the high-frequency components due to the switching. Fig.1-6 shows the basic structure of the signal injection method.

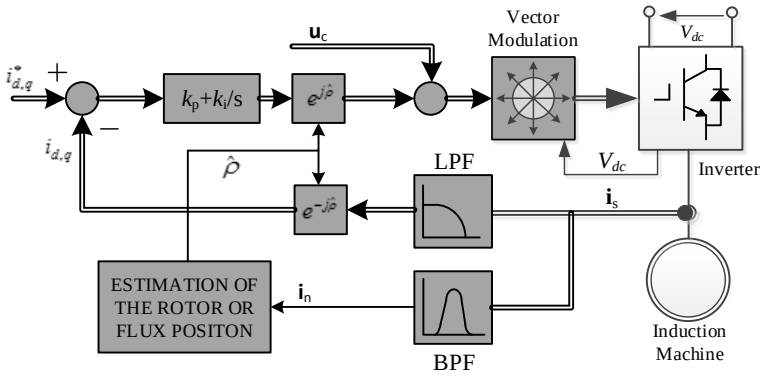

Fig 1-6 Basic structure for the determination of the flux or rotor position by using an injection method

Other methods in this category include high frequency pulsating carrier injection instead of the rotating one [1][4], which introduces a voltage vector on one of the axes of an estimated *dq* coordinate (synchronous frame). One of the problems of the signal injection technique is the low magnitude of the modulated signal. A method overcoming this is to impose to the machine a set of repetitive short reversal PWM voltage vector [36]. Correspondingly, the transient flux components cannot penetrate the rotor sufficiently to create a mutual flux linkage, the response of this short-term voltage disturbance is therefore of high magnitude.

1.1.2.2 PWM Harmonics

In this method [37], the PWM harmonics are used as an 'injected' HF excitation signal, therefore no extra signal injection is needed. It was found that at low speed, the 2nd PWM carrier harmonic (denoted as PWM2) has the largest amplitude, so it has been used as the 'injected' signal in the paper. The 2nd PWM carrier harmonic can be actually described as a pulsating vector, rotating approximately synchronously with the fundamental voltage vector in the stator fixed αβ frame as below,

$$v_{PWM2\alpha\beta} = \frac{2}{3}\frac{V_{DC}}{\pi}\left(\sin(\pi m_A) + a\sin(\pi m_B) + a^2\sin(\pi m_C)\right)\cos(2\omega_{PWM}t) \quad (1.15)$$

Where V_{DC} is the DC voltage, $m_x = \frac{2v_x}{V_{DC}}$ (x=A, B, C), v_x, ω_{PWM} are respectively the PWM output voltage and angular frequency.

Then, similar to HF pulsating injection approach, the resulting current PWM2 carrier harmonic $i_{PWM2\alpha\beta}$ together with the "injected" HF can be used for detecting the impedance related to the rotor speed. However as the HF pulsating vector amplitude and phase are now determined by the fundamental operation, the speed is retrieved from the impedance vector but not the resulting current. Paper [37] has proposed a novel position observer shown in the following (Fig. 1-7).

Fig.1-7 shows the demodulation block. The stator voltage and current vectors ($\mathbf{v}_{\alpha\beta}$, $\mathbf{i}_{\alpha\beta}$) are first band pass filtered with the centre frequency set to twice the PWM switching frequency. The filtered signals are further demodulated by a heterodyning technique. The HF carrier frequency component is removed by a discrete average filter. As a result only the amplitude modulation signal $\mathbf{v}'_{PWM2}$ and $\mathbf{i}'_{PWM2}$ of frequency f_{PWM2} are derived. An equivalent impedance vector $\mathbf{z}'_{PWM2}$ can be defined on the basis of the demodulated voltage and current PWM carrier harmonic vectors $\mathbf{v}'_{PWM2}$ and $\mathbf{i}'_{PWM2}$ as,

$$\mathbf{z}'_{PWM2} = \frac{\mathbf{v}'_{PWM2}}{\mathbf{i}'_{PWM2}} \quad (1.16)$$

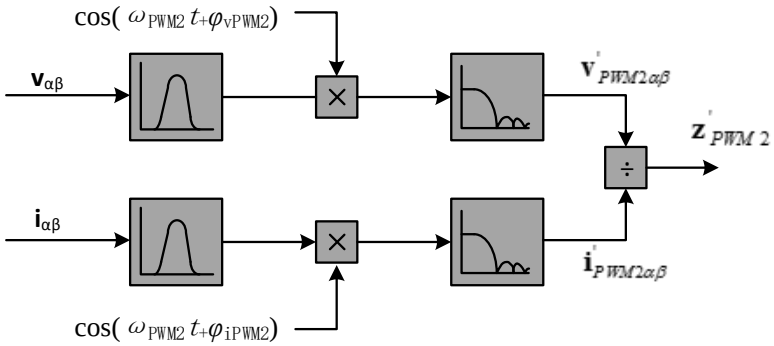

Fig 1-7 Block diagram of PWM2 signal demodulation

To retrieve the flux angle information from the impedance vector, it is assumed that the rotor bars (RB) cause a circular equivalent impedance modulation with the amplitude $\Delta Z'_{RB}$.

The angle θ_{RB} is the rotor bar position within one rotor bar period, which is the distance between 2 adjacent rotor bars. The idea is to detect the asynchronous modulation due to the conductor bars embedded in the rotor iron package of the machine. The resulting voltage equation system for the demodulated PWM2 variables is given by,

$$\begin{bmatrix} v'_{PWM2\alpha} \\ v'_{PWM2\beta} \end{bmatrix} = \begin{bmatrix} Z' - \Delta Z'_{RB}\cos(\theta_{RB}) & \Delta Z'_{RB}\sin(\theta_{RB}) \\ \Delta Z'_{RB}\sin(\theta_{RB}) & Z' + \Delta Z'_{RB}\cos(\theta_{RB}) \end{bmatrix} \begin{bmatrix} i'_{PWM2\alpha} \\ i'_{PWM2\beta} \end{bmatrix} \tag{1.17}$$

The impedance vector is shown as an equivalent impedance vector with an offset Z' and a circular modulation with the radius $\Delta Z'_{RB}$ rotating backwards with $\theta_{RB} + 2\angle i'_{PWM2\alpha\beta}$ occurs,

$$\mathbf{z}'_{PWM2} = Z' - \Delta Z'_{RB}\cos(\theta_{RB} + 2\angle i'_{PWM2\alpha\beta}) + j\Delta Z'_{RB}\sin(\theta_{RB} + 2\angle i'_{PWM2\alpha\beta}) \tag{1.18}$$

After compensating for the offset [37], the additional $2\angle i'_{PWM2\alpha\beta}$ phase modulation can be easily removed since the HF current vector position $2\angle i'_{PWM2\alpha\beta}$ is directly known. Fig.1-8 shows the corresponding signal tracking algorithm. A basic look up table (LUT) compensation scheme is implemented to extract only the desired rotor bar modulation. One PLL (PLL1) is used to track and filter the measured $\Delta\mathbf{z}'_{PWM2RB}$ modulation, which contains the rotor bar modulation signal. A second PLL (PLL2) is used to condition the final derived rotor bar position signal and construct the speed information.

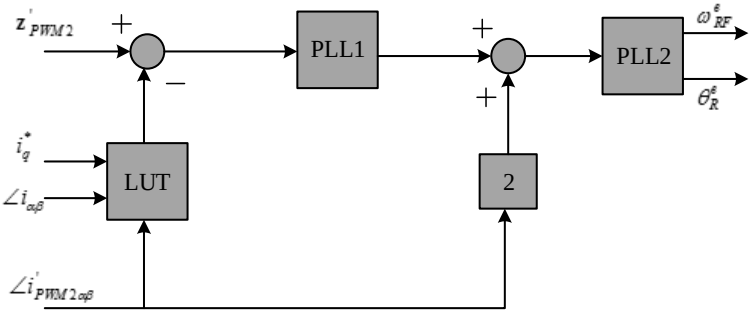

Fig 1-8 Signal tracking PLL's in the sensorless algorithm

1.1.2.3 Limitations of Anisotropy-Based Approach

Although problems at very low speed can be partly solved by these methods, in a real machine, the stator current signature presents a great quantity of harmonics: e.g., the saturation saliency resulting from the interaction of different fluxes in the machine will lead up to secondary saturation space harmonics [31]; The discrete nature of the windings and the non-ideal manufacturing process generally produce other space harmonics. The inherit high

frequency PWM harmonics. Moreover, there is generally more than one anisotropy in an IM with different spatial orientations: the response to an injected high-frequency signal necessarily reflects all anisotropies, and therefore contains more than one resulting harmonics close to each other. In order to separate the useful signals with noise, complicate signal processing methods are needed. This is usually achieved by using a band-pass and a band-stop filters, but they limit the bandwidth of both the current controller and the observer.

The tracked saliency depends on the overall saturation effect and will shift under a load [31]. Robust operation across the whole torque and low/zero frequency regions is not always possible. Besides, the modulating signal represents itself an additional harmonic of high amplitude to be cancelled [35]: this will cause instability of the control system at the extreme condition. Although PWM harmonic methods [37] do not have this problem, more complicate signal processing is needed due to the low amplitude of the useful signal.

1.2 Contributions

Since the fundamental-model based method has limited performance due to the non-observability of the model at low speed and sensitivity to the machine parameters, there has recently been considerable interest in anisotropy-based methods for the sensorless control of AC machines. However, the anisotropy information is usually retrieved by signal injection, where extra harmonics have to be introduced into the machine and complicate signal processing is required to retrieve the speed information. Other problems are related with the possible saliency shift problem, and finally the robustness of the method is not always satisfactory. PWM harmonics methods, which do not have to inject extra signal to the machine, alleviate the problem of signal injection, but their performance is highly determined by the PWM inverter pattern.

Thus, extensive research has been carried out in the extraction of the speed related rotor slot harmonics (RSHs) to estimate the speed. These algorithms require no extra signal injection, are independent of machine parameters, like stator and rotor resistances, and are mainly focused on the feasibility in steady-state or quasi steady-state. This thesis, on the contrary, will develop methods for tracking the RSH which are able to work online with high rejection ability to load torque changes. The proposed RSH speed estimators have also been applied to the scalar control system, they can work in a wide speed range, yet the

entire system is simple, computationally not demanding, and low cost. It is characterized by a very low sensitivity to the parameters variations.

To directly track the RSH, the capability of the proposed system is tied to the following features of the detection system:

1). High pull-in capability so as to track the RSH in the entire speed range of the machine, where the loop gain at RSH frequency is high, while decreasing sharply as the frequency deviates away;.

2). A flexible and selective bandwidth so as to simultaneously track the RSH in a wide range of variation without permitting any noise to enter in the band of the detector.

These issues have been fully addressed and solved in the thesis. The proposed method can continuously and accurately track the rotational speed of IM at both dynamic or steady-state conditions, and the centre frequency do not have to be changed manually at each computation cycle.

1.3 Organization

This thesis considers the sensorless control of IMs using RSH in wide speed range, a background introduction on RSHs and literature review are presented in Chapter 2. Issues related to the RSH based speed estimator are discussed.

Chapter 3 presents the scheme of scalar control. It is not new, but it is included for the sake of readability. Also some improvements are made on the basis of the conventional scalar control scheme.

Chapter 4 describes RSH tracking method using the phase-locked loop, and the corresponding sensorless scalar drive. Simulation and experimental results are presented to verify the algorithm.

Chapter 5 describes the framework of RSH speed estimator based on minor component analysis, particularly by using the MCA EXIN neurons.

Finally, Chapter 6 summarizes and gives recommendations for future work.

In Appendix A, the IM model including the rotor slotting effect is presented. Its validity has been verified in simulation.

In Appendix B, the eigen-decomposition of the autocorrelation matrix is discussed, it is the fundamental of the Pisarenko' method.

In Appendix C, a graphical User Interface for TLS EXIN neurons is included, with an analysis of the MCA EXIN algorithm.

Appendix D includes the generalization of linear regression problems, where the differences are described mathematically among the OLS, DLS, and TLS.

CHAPTER 2. SPEED DETECTION USING ROTOR SLOT HARMONIC

Rotor slot harmonics (RSHs) are found in the stator current waveforms for most induction motors. Algorithms have long ago been developed to track the speed of a motor given a dedicated stator current measurement, for example [38][39]. These methods are insensitive to motor parameter changes with frequency, temperature, or any other external disturbances. Besides being used for nonintrusive speed estimators, harmonic analysis has also been applied to diagnostic detection of electro-mechanical faults such as rotor eccentricity and damaged bearings [40].

In the control of an electric drive, accuracy and speed of response are the main two criteria describing the performance of a speed sensor. This chapter introduces the RSHs and issues around the extraction of RSH. Moreover, the limitations of previous literature that use RSHs for speed tracking or sensorless drive will be fully addressed. The improved methods developed in this thesis can estimate the speed with reduced time and improved accuracy, and they are suitable for sensorless drives, which will be described in the next chapters.

2.1 Rotor Slot Harmonics

2.1.1 Introduction

In an induction motor, the speed related RSHs present in the stator current signature arise from the interaction between the permeance of the machine and the associated magnetomotive force (MMF). As the motor turns, the rotor slots alter the effective length of the air-gap periodically, thereby the permeance of the machine. This behavior is visible in the flux wave, which is the product of the MMF (the fundamental component) and the permeance across the air-gap. The resulting harmonic components of the machine flux move with respect to the stator and induce corresponding voltage harmonics and hence current harmonics in the stator winding.

Besides the fundamental MMF, the odd harmonics present in the stator and rotor current introduce a series of space and time MMF harmonics, producing the additional RSH of higher order.

Static and dynamic eccentricity harmonics also appear in the stator current as a result from rotor rotating irregularly in relation to the stator axis.

These harmonics are essentially a function of the number of pole pairs, the number of rotor slots per pole pair, and the speed, as it results from the following equation [41]:

$$f_h = (r\,q_r \mp n_d / p)(1-s) f_1 \mp v\, f_1 \tag{2.1}$$

Where

f_1 fundamental harmonic of the supply voltage;

s slip;

p number of pole pairs;

q_r number of rotor slots per pole pair;

n_d eccentricity order (n_d = 0 in case of static eccentricity and n_d = 1, 2, 3… in case if dynamic eccentricity),

r order of the space harmonic, r = 1, 3, 5, …;

v the order of the stator time harmonics present in the power supply driving the motor. v = 1, 3, 5, …

It is worth mentioning that the stator slots, on the other hand, also affect the air gap permeance; the air-gap flux harmonics therefore result from the variation of the permeance due to both rotor and stator slotting. However, it has been found that there is no time harmonics in the air-gap field which is related to the stator slots. This means that the number of stator slots affects only the space distribution of the flux harmonics relative to the stationary stator, and will not induce new frequencies in the current signature: a detailed discussion can be found in [42,53] .

The principal slot harmonic (PSH) which refers to the first and the prominent harmonic in the RSH series, is obtained by (2.1), with r = 1 and n_d = 0, v = 1 if the time harmonics of the stator and rotor currents together with the static and dynamical eccentricities are neglected. In this case the rotor slotting effects are located at frequencies:

$$f_h = q_r f_1 (1-s) \mp f_1 \tag{2.2}$$

For most of the data presented in this thesis, there is little rotor imbalance so the most visible RSHs are given by (2.2), known as PSHs. However the motor is supplied by the

inverter and the higher time harmonics cannot be neglected, so v can have higher values than 1.

It should be noted, however, that the harmonics, as described by (2.2), are not present in a real machine for any combination of the number of rotor slots and pole pairs [43-47]. The time harmonics obtained with (2.2) result from the corresponding space harmonics of the resulting MMF, which are of order $q_r \mp 1$. Since $q_r = 3m \pm 1$, this also implies that one of the two space harmonics is always a multiple of three, and therefore, it never induces a time harmonic in a healthy machine (e.g., balanced three-phase winding). This will lead to the fact that, the lower PSH (upper sign) in (2.2) exists in the stator current spectrum when q_r satisfies,

$$q_r = 3n - 1 \quad n = 0,1,2,... \tag{2.3}$$

The higher PSH (lower sign) exists when q_r satisfies,

$$q_r = 3n + 1 \quad n = 0,1,2,... \tag{2.4}$$

In the case under study, the adopted motors have 2 pole pairs, 36 stator slots (q_s=18=3m, as in most cases) and 28 rotor slots (q_r=14=3n-*1*), meaning only the lower PSH frequency is noticeable in the stator current signature.

Fig.2-1 depicts how the PSH follows slip changes at constant speed. The experimental motor is operating in steady-state at mechanical speed of 10rad/s with a scalar controller, under load varying from 0 to 30% of rated value. It can be observed that the fundamental and the time harmonics frequencies increase with the slip. The PSH however, overlap with the time harmonics under some condition, e.g. the PSH lies higher than the 11th harmonic, and approaches the 7th at 30% load, making it difficult to be tracked dynamically. From (2.2) the frequencies where PSH meets the other harmonics can be further calculated when $f_h = 11f_1, 7f_1, f_1$, whereby the slips are s=$\frac{1}{7}$, $\frac{3}{7}$, $\frac{6}{7}$ respectively. On the other hand, the amplitude of the RSH fades as the load decreases, since the slot permeance hardly changes with the load, so the slot current is almost proportional to the fundamental current.

Fig. 2-2 illustrates how the PSH changes with the motor speed. The adopted machine runs at low speed range, under no load condition. The operating speed varies from 1 to10 rad/s. It is shown that the PSH decreases with the machine speed; in particular at very low speed, isolating the PSH from the other harmonics is really challenging as the PSH become

closer to the other time harmonics. This difficulty is even harder considering that the working condition of the machine is unpredictable.

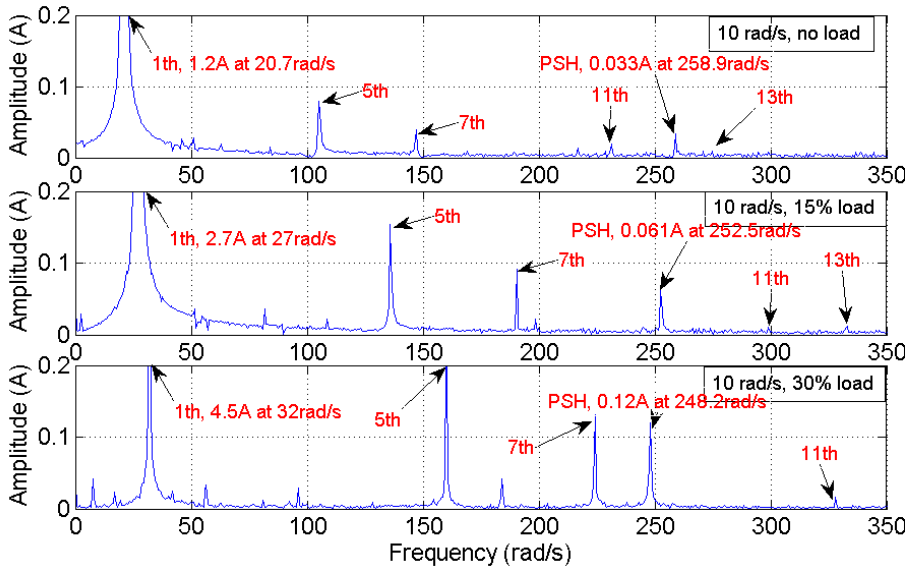

Fig 2-1 Current signature of the experimental motor runs at 10 rad/s, under different load

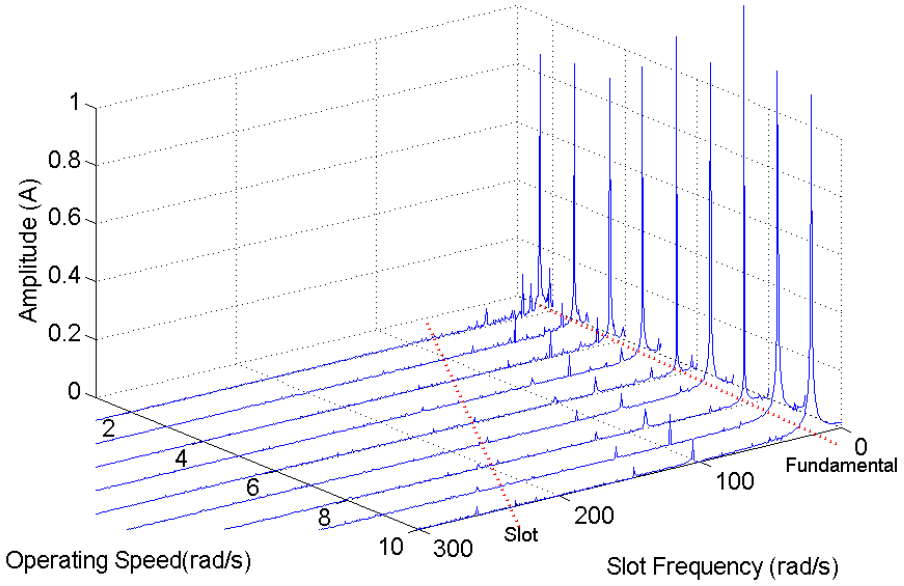

Fig 2-2 Current signature of the experimental motor at low speed from1-10 rad/s, at no load

2.1.2 Experimental results

A more complete harmonic analysis on the stator current signature has been performed at different operating speeds as well as at no load and with load. This has been done with

the goal to verify which are the limits of the observer to properly extract only the RSH from the whole stator current signature. The experimental harmonic analysis has been made by employing the Real Time Signal Analyser Tektronics RSA5103A instrument, which permits the frequency range and the frequency accuracy to be analyzed even at very low frequency.

The Real Time Signal Analyser Tektronics RSA5103A has been equipped with an attenuator of 40 dB to measure the voltage signals coming from current sensors; to obtain the amplitude of the measured current, the value read on the screen is to be added to 43 dB (the presence of the attenuator of 40dB+3dB to convert the RMS into amplitude).

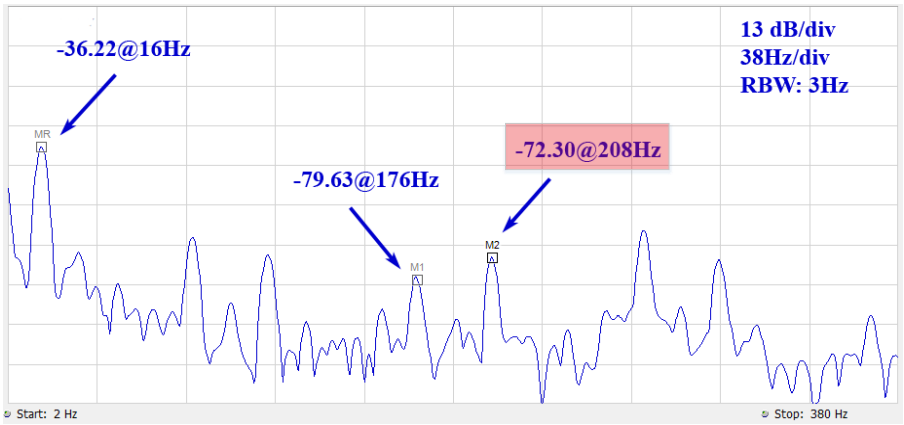

Fig 2-3a. Spectrum of the stator current signature at constant speed of 50 rad/s with no load

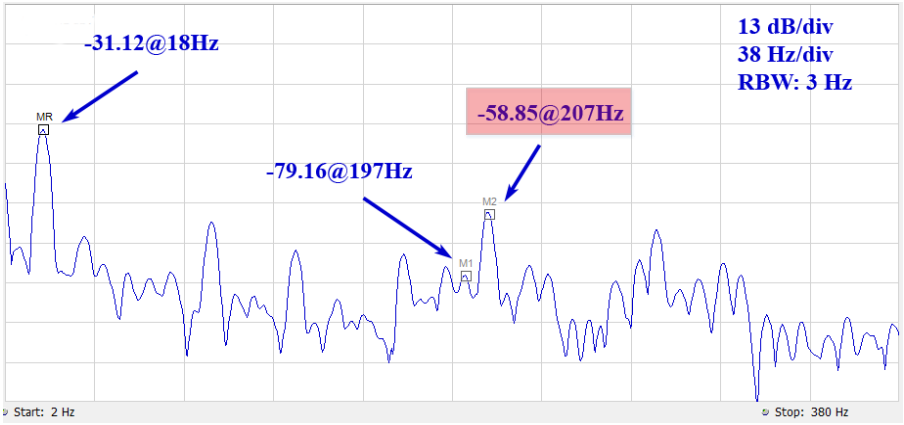

Fig. 2-3b. Spectrum of the stator current signature at constant speed of 50 rad/s with 10 Nm load torque

Fig.s 2-3 a and b show the stator current signature spectrum, measured with the above cited instrument, obtained at steady-state during a constant speed of 50 rad/s, respectively at no-load and at rated load (10 Nm torque). The RSH at no-load is correctly detected by the system at 13·50/π=208 Hz, while it moves to 207 Hz at rated load according to (2.2), maintaning the working speed at 50 rad/s with a slip pulsation of ω_2=13 rad/s. At this working speed, the closest harmonic to RSH is the 11th , which lies at 176 Hz at no-load, while it moves to 197 Hz at load.

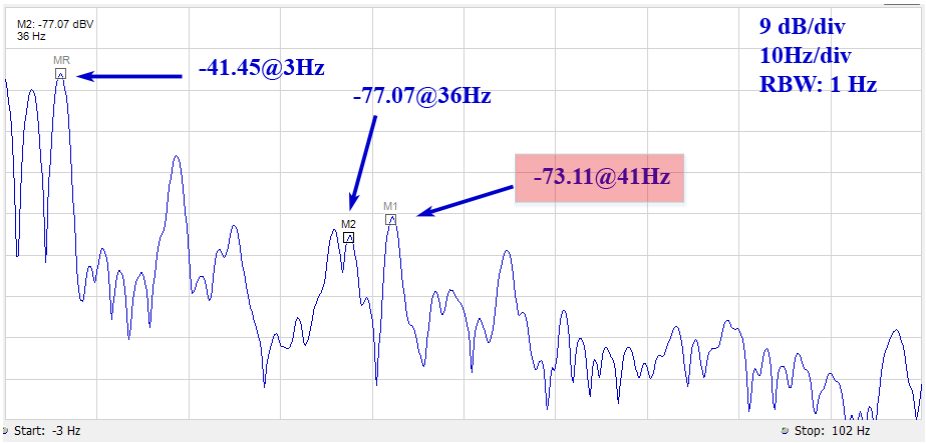

Fig 2-4a. Spectrum of the stator current signature at constant speed of 10 rad/s with no load

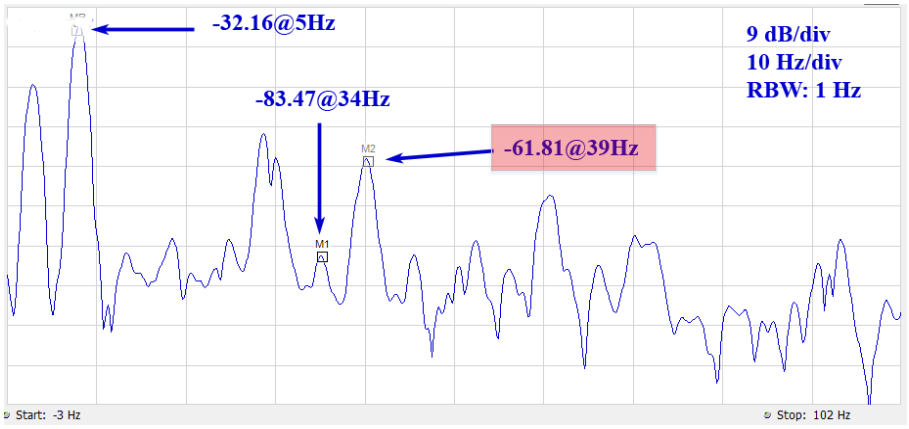

Fig. 2-4b. Spectrum of the stator current signature at constant speed of 10 rad/s with 10 Nm load torque

Fig.s 2-4 a and b show the current signature spectrum obtained at steady-state during a constant speed of 10 rad/s, respectively at no-load and at rated load (10 Nm torque). The RSH at no-load is correctly detected by the system at 13·10/π=41 Hz, while it moves to 39

Hz at rated load according to eq. (2.2), maintaning the working speed at 10 rad/s with a load slip pulsation of ω_2=11.41 rad/s. At this working speed, the closest harmonic to RSH is the 11th at no-load, which lies at 36 Hz, while it is the 7th at load, which lies at 34 Hz.

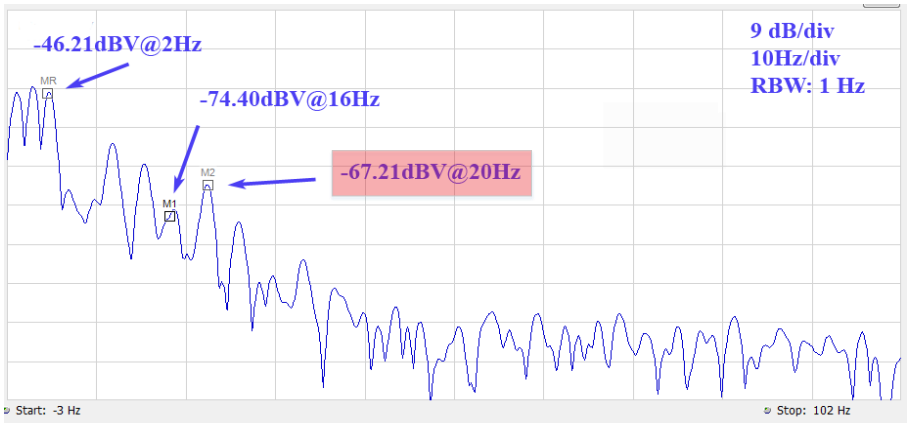

Fig 2-5a. Spectrum of the stator current signature at constant speed of 5 rad/s with no load

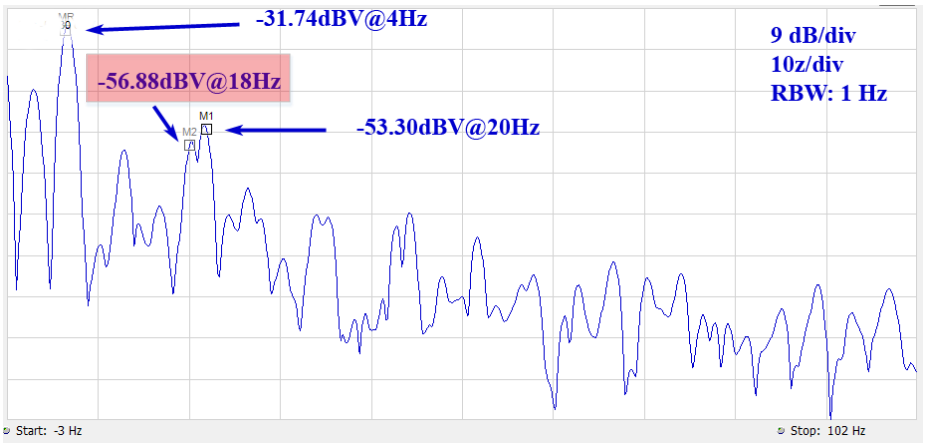

Fig. 2-5b. Spectrum of the stator current signature at constant speed of 5 rad/s with 10 Nm load torque

Fig.s 2-5 a and b show the current signature spectra obtained at steady-state during a constant speed of 5 rad/s, respectively at no-load and at rated load (10 Nm torque). The RSH at no-load is correctly detected by the system at 13·5/π=20 Hz, while it moves to 18 Hz at rated load according to eq. (2.2), maintaning the working speed at 5 rad/s with a load slip pulsation of ω_2=15 rad/s. At this working speed, the closest harmonic to RSH is the 11th at no-load, which lies at 16 Hz, while is the 5th at load, which lies at 20 Hz.

All these results are summarized in Table 2-1. It can be found that all the slot harmonics appear at frequencies in accordance with the theoretical values calculated from (2.2). For example, while at no-load the closest harmonic to RSH is the 11^{th}, as expected, at rated load the closest harmonic remains the 11^{th} at 50 rad/s, while it becomes the 7^{th} at 10 rad/s and the 5^{th} at 5 rad/s. This can be explained, considering that at low speed and high load, the slip pulsation ω_2 becomes comparable or higher than the fundamental one; correspondingly the 7^{th} or 5^{th} harmonic can become closer to RSH than the 11^{th} .

TAB 2-1 AMPLITUDE AND FREQUENCIES OF RSH AT VARIOUS SPEED

	f_1		f (closest harmonic.)		f_{RSH}	
	f [Hz]	I [A]	f [Hz]	I [mA]	f [Hz]	I [mA]
5 rad/s no load	2	1.38	16(11^{th})	53	20	123
5 rad/s 10Nm	4	7.31	20(5^{th})	611	18	404
10 rad/s no load	3	2.39	36(11^{th})	39	41	62
10 rad/s 10 Nm	5	6.96	34(7^{th})	19	39	229
50 rad/s no load	16	4.36	176(11^{th})	29	208	69
50 rad/s 10 Nm	18	7.85	197(11^{th})	31	207	323

2.2 Review of Literatures on Speed Estimation via RSH

When the location of the speed dependent PSH is found, the speed of the electric motor can be computed rather easily: assuming f_h is known, from (2.2), the rotor speed (expressed in electrical rad/s) is given by,

$$\hat{\omega}_r = 2\pi f_1(1-s) = \frac{2\pi(f_h + f_1)}{q_r} = \frac{\omega_h + \omega_1}{q_r} \tag{2.5}$$

Thus, the difficulty of speed estimation via PSH lies in the retrieve of PSH, for in a healthy machine the air-gap field and the stator current signal present a great quantity of

harmonics caused by winding distribution, slotting effect, air gap eccentricity, PWM supply, etc [42][48-52]. Among all these harmonics, PSH is located at rather high ranges in the stator current spectrum, but it moves toward the fundamental frequency when the slip increases. Especially at low speed, the slip s increases dramatically even if the load torque remain constant (considering the slip frequency $f_2 = sf_1$ remain constant, at low speed f_1 decreases, thus s will increase), the PSH could lie at the same region of the 1^{th}, 5^{th} and 7^{th} harmonics, see tab.2-1 for example. Thus, in practical drives, the PSH varies in a very wide range (from a few hertz to hundreds of hertz) and rapidly (it is dependent of the applications, normally within a few milliseconds) and moreover the retrieval of PSH is made harder by the other harmonics arising both from the inverter and the motor itself.

As far as the direct RSH tracking is concerned, two main approaches have been followed in literature:

A. *Frequency domain methods*, which are mainly based on FFT (Fast Fourier Transform)-like approaches;

B. *Time domain methods*, which are mainly based on PLL (Phase-Locked Loop)-like approaches.

2.2.1 Frequency Domain Methods

As for the frequency domain approaches, the main contributions are the [53-58].

A pioneering work has been made in [53], where a speed detector based on fast Fourier transform (FFT) has been described. As shown in fig. 2-6, the conditioned phase current is first decomposed into frequency components by using FFT. Then the algorithm search the location of supply frequency $f_1$within the range close to the fundamental inverter frequency f_0. Following (2.2), the component found is then used to define another two harmonic index ranges where the slot harmonics component might be located. The first range, [18($f_0/\Delta f$), 19 ($f_0/\Delta f$)-1], allows for under-load condition and the second one, [18($f_0/\Delta f$), 19($f_0/\Delta f$)+1], for near no-load condition ($s \approx 0$), where Δf is the frequency resolution of the algorithm. The load condition is determined by setting a threshold on the amplitude of the RSH. The isolated RSH component and fundamental component are used to compute the rotor speed using (2.5). The FFT approach has shown a good estimation accuracy and can effectively work in a wide range with the help of fast digital signal processing. However, the resolution of the FFT depends on the data sampling frequency f_s and the data block

length N (or f_s/N exactly), its speed of response is very limited due to the long data records required to produce a good frequency resolution. Fast tracking of RSHs, particularly during high slew rate transients, is a real challenge. As consistently shown in the paper, a single cycle speed estimation (including data acquisition, spectral estimation, harmonic extraction, etc.) time reaches about 3*s* at 10-kHz sampling rate.

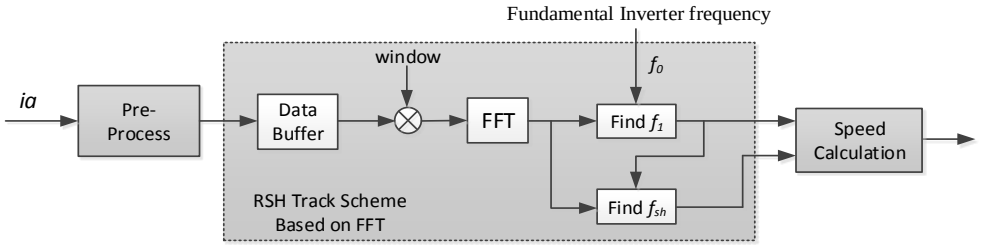

Fig 2-6 FFT based speed detector

Some modern spectral estimation methods (mainly parametric methods), such as the covariance method [54], the Prony method [55], have been used to improve the speed of response of FFT, with the accuracy of FFT being retained. An example can be found in [56], where Hurst proposed a speed estimation algorithm employing maximum entropy spectral estimation (MESE) method [57]. Many improvements have been made compared to the FFT approach: a notch filter is added to eliminate the fundamental current (see fig. 2-7); Down-sampling of the current sequence is used to increase the effectiveness of subsequent filtering operations; Before the MESE, a 26th-order band-pass filter is used to eliminate all spectral harmonics outside the range containing expected RSH, etc. The main improvement, however lies in the MESE itself, which is based on linear prediction model whose impulse response best matches the data, by least-square minimization. It is able to compute the frequency with less points of data (36 points as used in the paper), as a consequence, it largely reduces the required sampling time and provides increased robustness to noise. Yet the drawbacks is obvious as well: the model order p has to be selected a priori with the experience of the author, it is required that the machine operates at a certain speed range, so the harmonics close to PSH is predictable. Besides that, the ratio between sampling frequency and fundamental frequency remain fixed, resulting in a long converging time at low speed.

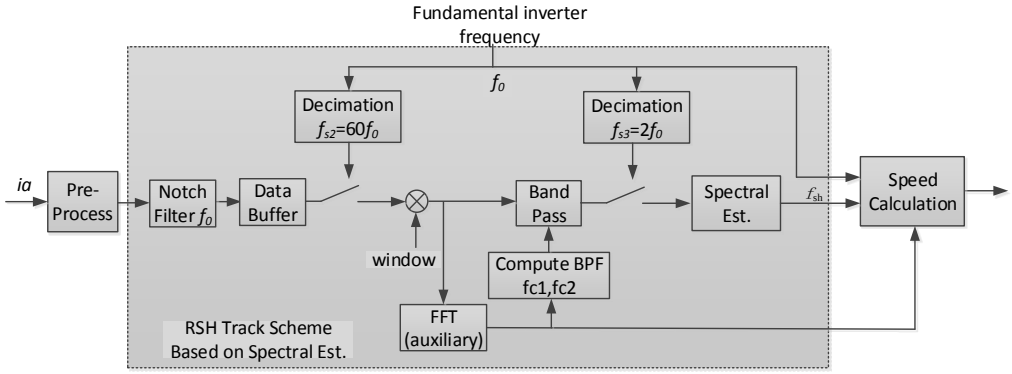

Fig 2-7 Speed detection algorithm based on spectral estimation.

Apart from the modern spectral estimation approach, some papers have exploited the use of other types of transformation. One example can be found in [58], where the harmonic analysis of the machine current is taken by means of the chirp-Z transform (CZT). Compared to the FFT, the frequency transformation is limited to certain restricted frequency bands. In the case of RSH tracking, they are frequency bands centered at the fundamental inverter frequency f_0 and the expected RSH frequency f_{sh}. Thanks to this constraint, the frequency resolution increases to f_w/N, where f_w is the bandwidth of the selected window, and *N* is the data length. It has been shown in the paper that, Chirp-Z transform reduces sampling and process time to 1.5s from 4.1s of the standard FFT approach with the same resolution. Despite this improvement, the response time remains too long for a real-time speed detector. Moreover, a shorter observation window is required for the CZT, if the RSH frequency jumps out of the expected frequency range, the algorithm fails.

With all the frequency domain approaches under consideration, they generally provide good accuracy and linearity over a very wide speed range and load conditions, but a compromise has to be made between the required frequency resolution, to allow speed detection, and the response time versus changes of speed. A desired high frequency resolution imposes the acquisition of a large amount of samples and a corresponding high acquisition time. It means that the information on the RSH estimation can be updated only when the sampling window is completed. Besides that, the spectral analysis algorithm can only work with the help of band-pass filters: In steady-state, these filters will only increase the computation burden, but as long as the transient is concerned, the band of the filters has to be adapted according to the expected frequency of PSH, the transient of these filter during the

parameters changing stage is complicate, together with the sensitive frequency analysis method, this implies that speed tracking during transients could provide insignificant results.

2.2.2 Time Domain Methods

As far as the time domain approach is concerned, the main contributions are the following [59-61].

The speed identifier, which was proposed in [59], has used an adaptive digital filter to estimate the frequency of RSH (see fig. 2-8). The phase current is first pre-filtered by a high pass and band pass filter so that only the harmonics close to RSH are left, the cut-off frequencies of these filters are tuned online based on the fundamental inverter frequency f_0 and slip s, which is estimated by torque current i_q (it is very closely proportional to slip frequency for operation up to base speed). f_{sh} is then computed as follows: by tuning the centre frequency of an infinite impulse response (IIR) notch filter to minimize the remainder of the filtered output spectrum, so at steady-state, the center frequency of this notch filter will be equal to the RSH frequency f_{sh}. This method provides a sample by sample estimation of the rotor speed, and since the RSH is defined directly by the notch filter parameters but not its output, it is claimed that the RSH frequency can be identified in 0.2 ms at 5-kHz sampling rate. The computational burden of this method is low as well. However, one difficulty might be the redesign of band-pass filter, because the motor speed changes fast, and the centre frequency of this filter has to adapt with the expected location of RSH. Unlike the frequency domain method, [59] highly relies on the on-line tuning of filter parameters, and such tuning often requires comprehensive understandings of the convergence properties of filters and increases the amount of computation considerably.

A similar RSH frequency detection approach using filtering has been proposed in [60], where a digital IIR band-pass filter is used to let only the PSH pass through. The cut-off frequency of the filter is directly linked with its parameters, so it can be tuned quickly online. The frequency of the extracted RSH is determined by counting the number of zero-crossing, meaning the computation burden will be largely decreased, however with degraded accuracy. Although the idea of the easy tuning filter is novel, in practice, a sole band-pass filter is hardly able to isolate the RSH from the other harmonics, unsurprisingly, large oscillation of the estimated speed can be found in the results.

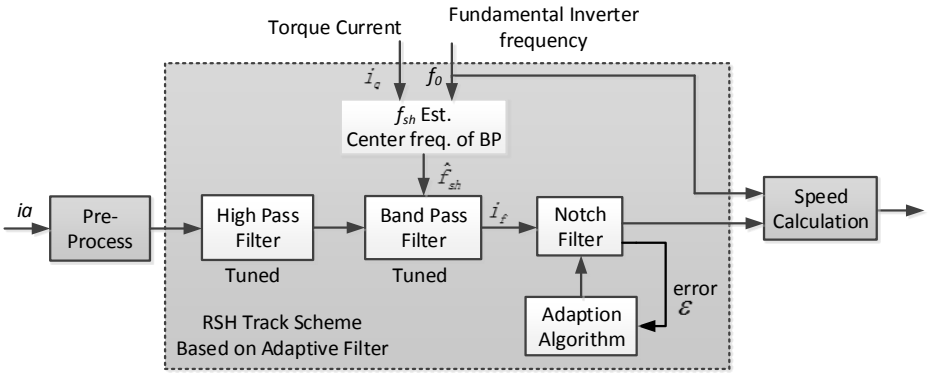

Fig 2-8 Speed detection algorithm based on adaptive filter

A frequency tracking method based on frequency demodulation approach, which is actually an opened-loop PLL has been introduced in [61]. Since it implements in complex domain, a complex current vector is first formed by phase currents, it is then fed to the frequency-demodulation block as shown in fig. 2-9, where the resulting RSH frequency is the sum of two component: the expected slot frequency $f_{sh,0}$ and the correcting term $f_{R,n}$. Given the parameters are well tuned, the output $f_{sh,n}$ should be accuracy and response fast, and the local oscillator frequency permits the band-pass filter to be properly tuned with constant bandwidth. One major drawbacks is that, the frequency of the local oscillator has to be chosen a priori, on the knowledge of RSH under constant (rated) supply frequency. As a consequence, such a method cannot be used in a variable speed drive case, since it requires an on-line adaptation of the local oscillator frequency according to the drive reference speed. This is the reason why results are presented only at rated or close to rated speed. Moreover, to guarantee the validity of this method, the instantaneous RSH should be clearly the largest signal in the varying frequency span between the rated and the current work condition, this is not always true in practical platform due to the presence of harmonics.

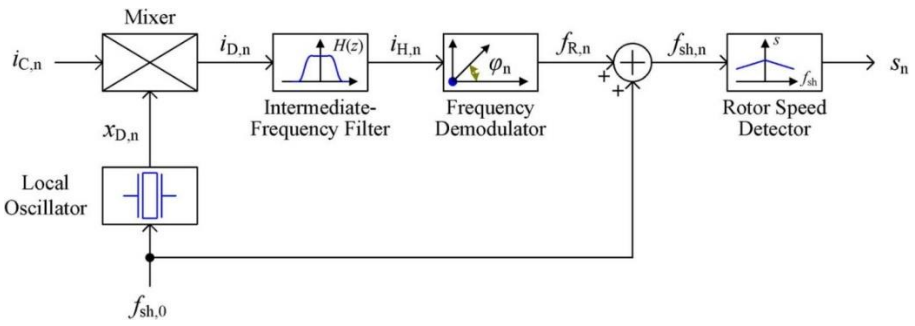

Fig 2-9 Speed detection algorithm based on a frequency modulation method ([61])

The time domain method provides a better real time performance than the frequency domain method, although the accuracy of the result will be affected by the noise level. They generally behave like such a band-pass filter: the gain is very large at the RSH frequency and very small away the RSH frequency, they usually need a better prior knowledge of the location of expected RSH frequency, so that the system operates only around a small band. If this band is not chosen correctly, this method fails. Therefore there is always the possibility of line frequency harmonics or harmonics from other sources being mistaken with RSH.

Considering all the pros and cons, this thesis mainly focused on the time domain method, making it better suited for real-time applications. Yet improvements have to be made on both the resolution and the on-line tuning, so that the system can work robustly in a very wide range.

2.3 Practical Tuning of the Observation Window

As stated earlier the current signature has a variable bandwidth directly related to the supply frequency f_1 and slip s. For high efficiency induction motors, the slip s usually does not exceed 5% and possibly less. This assumption leads to interesting simplifications when searching for the PSH. If the PSH was confined to a frequency window under the practical limitations of slip, there would be no ambiguity in determining the window in which the PSH is located. This is not always true however, at low frequency. This is because the output torque is proportional to slip frequency ($f_2 = sf_1$), the rated slip increases as f_1 decreases. It has not taken into the consideration the imperfect behavior of the controller, in practice, the slip can be large at low speed.

On the basis of the above discussion, the observing window should be further refined to exclude the other harmonics, permitting a better robustness and faster convergence, the real-time slip pulsation ω_2 can be estimated, in this case, on the basis of a simple rotor flux estimator, defined by the following equations written in the stator reference frame (see [1] p. 414):

$$\omega_2 = \frac{L_m}{T_r \left|\boldsymbol{\Psi}_r\right|^2}\left(\psi_{rd} i_{sQ} - \psi_{rq} i_{sD}\right) = \frac{2R_r}{3\left|\boldsymbol{\Psi}_r\right|^2} t_e \tag{2.6}$$

where i_{sD}, i_{sQ} are the stator currents components in the stator reference frame, $|\boldsymbol{\psi}_r|$ is the amplitude of the rotor flux and ψ_{rd}, ψ_{rq} its components in the stator reference frame, t_e is

the electromagnetic torque, L_m and T_r are respectively the three-phase magnetizing inductance and the rotor time constant. This simple flux estimator requires the knwoledge of just two electrical parameters and does not requires any computationally demanding vector rotation.

The slip pulsation calculated by (2.7) and the fundamental inverter freuquency can be used to update an estimated location of RSH by using (2.2), then it can be used as the center frequency of the observing window. The bandwidth of this window, should be as small as possible, to eliminate the disturbance of other harmonics.

2.4 Effect of Eccentricity of the Motor

One important issue to be considered is the influence on the rotor speed estimation of a potential dynamic eccentricity. In case of dynamic eccentricity, it is well known in literature that the stator current signature exhibits a couple of main sidebands, derived from (2.1) with n_d=1, r=1 and v=1:

$$f_h = (q_r \mp 1/p) f_r \mp f_1 \tag{2.7}$$

Where f_r is the rotor speed expressed in Hz, if (2.5), without considering any dynamic eccentricity, is adopted for speed estimation, an error on the estimated speed occurs. This error can be written as:

$$\frac{\Delta f_r}{f_r} = \frac{f_r' - f_r}{f_r} = \left(\frac{f_h + f_1}{q_r \pm 1/p} - \frac{f_h + f_1}{q_r} \right) \frac{1}{f_r} = \frac{1}{pq_r - 1} \cong 1/27 \tag{2.8}$$

With f_r' the rotor speed considering dynamic eccentricity. The percentage speed estimation error, with the 2 pole pairs and 14 rotor slots for pole pair machine, is constant and about 3.7 %. This error poses the sidebands out of the normal searching range, which means that the speed could not be properly estimated.

To overcome this problem, one way is to increase the searching range of the extraction algorithm. This, however, implies a worse performance, since other harmonics can easily enter the predefined bandwidth, and it is difficult to distinguish the RSH from the others

Another solution is, whenever it is known that a dynamic eccentricity occurs, to adopt a speed estimation formula directly taking into consideration the eccentricity, differently from (2.5), as:

$$\hat{\omega}_m = \frac{\omega_h + \omega_{1ref}}{q_r - 1/p} \tag{2.9}$$

The adoption of (2.9) instead of (2.5) permits the correct computation of the speed and consequently the correct on-line tuning of the centre RSH bandwidth.

2.5 Determination of the Number of Rotor Slot

The number of rotor slots, if unknown, can be determined by generating a set of stator current data records at rated supply frequency and under increasing load levels. A visual inspection in the spectrum reveals the speed-dependent harmonic as a component increasing in amplitude and decreasing in frequency. From the frequency of this component and the knowledge of the slip (only approximate value is needed), the number of rotor slots is easily determined according to (2.2). A long enough data records has to be used to guarantee the frequency resolution, so that the PSH can be easily distinguished.

A Matlab script can be designed to compute the number of rotor slot from the measured stator current. So long as the fundamental frequency is known, it is not difficult to compute the possible PSH range according to an estimated load condition. All the other time harmonics related to the fundamental can be excluded firstly, then the possible PSHs in the range can be selected by setting a threshold on the amplitude. With the help of those harmonics which comply with the selection criteria, the number of rotor slot can be determined by trying (2.2) with a reasonable integer rotor slots iteratively. Since most machines have a number of stator slots defined by their size and pole number, rotor slots are then marginally greater or less than this number.

CHAPTER 3. SCALAR CONTROL SCHEME

Control techniques of induction machines (IMs) can be divided into two main categories: scalar and vector controls[2][4][62-66]. Scalar control is based on the steady-state model of the IM and therefore permits regulating at steady-state only the magnitudes and frequency of the stator voltages, currents, flux linkages, and electromagnetic torque. Since it does not act on the angular position of the space vectors of the control variables, it does not permit the best dynamic performance to be achieved. On the contrary, vector controls are based on the dynamic model of the machine; they permit the drive to achieve its best dynamic performance in terms of electromagnetic torque control, thanks to their feature to take into consideration the instantaneous angular position of the stator voltages, currents as well as of the flux linkages.

Although vector control can provide higher dynamic performance, some kinds of mechanical loads exist which do not require a high dynamic performance. Typical examples are fans and pumps where it is sufficient to regulate the speed of the IM with adequate efficiency over a wide speed range. This implies that it is sufficient to use the steady-state model of the IM instead of the dynamic one, as far as the control system design is concerned. The machine is supposed to be supplied by a pulse width modulation (PWM) voltage source inverter (VSI), able to generate a set of three-phase voltages whose fundamental component is characterized by the desired amplitude and frequency. Scalar control of IMs was born with the idea to use as a simple control method for regulating the speed of an AC machine [67-69].

3.1 Steady-State modeling and V/f Control

3.1.1 Steady-State Modeling

The open loop voltage/frequency (V/f) control (scalar control) is described in numerous papers in literature [2][62][70][71], the main idea is described here for coherence.

The steady-state per-phase equivalent circuit of a symmetrical three-phase operation induction machine in steady-state is shown in fig. 3-1 [62]

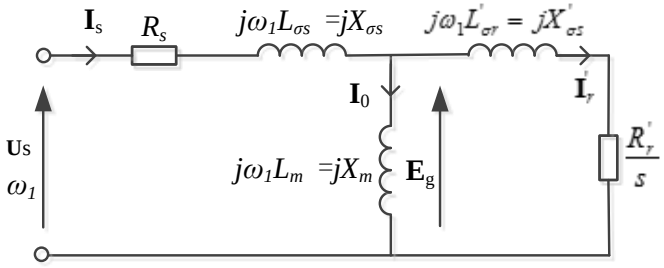

Fig 3-1 Steady-State per-phase equivalent circuits of IM

Where -$\mathbf{U}_s$, $\boldsymbol{E}_g$ are the phasors of supply voltage, air gap voltage respectively,

-$\mathbf{I}_s$, $\mathbf{I}_0$, $\mathbf{I}'_r$ are the phasors of stator, mutual, rotor current,

-R_s, R_r, $L_{\sigma s}$, $L_{\sigma r}$, are the resistance, leakage inductance of stator and rotor,

- $X_{\sigma s}$, $X_{\sigma r}$represents stator and rotor reactance,

-ω_1 represents the supply frequency in electrical rad/s,

- s=slip,

- variables with a superscript (') are rotor variable referred to the stator.

For simplicity's sake the core losses have been neglected.

Starting from the steady-state space-vector equations of the IM, the air-gap electromagnetic torque is related to the mechanical power and air gap power as

$$T_e = \frac{P_m}{\omega_m} = \frac{P_{gap}(1-s)}{\omega_1(1-s)} = 3\frac{\left|\mathbf{I}'_r\right|^2 R'_r}{\omega_1 s} \tag{3.1}$$

Where P_m and P_{gap} are the mechanical and air gap power, and ω_m is the rotor mechanical speed (in electrical radians).

The current can be obtained from fig. 3-1 as

$$\mathbf{I}'_r = \frac{\mathbf{U}_s}{(1+\sigma_s)\left\{R_s + R'_r/s + j\left[X_{\sigma s}/(1+\sigma_s) + X'_{\sigma r}\right]\right\}} \tag{3.2}$$

Where $\sigma_s = \frac{X_{\sigma s}}{X_m}$ is the stator leakage factor.

Thus by substitution of eqn. (3.2) into eqn. (3.1), the electromagnetic torque can be expressed in terms of the machine parameters as,

$$T_e = \frac{3}{\omega_1}\frac{\left|\mathbf{U}_s\right|^2}{(1+\sigma_s)^2}\frac{R_r^{'}/s}{(R_s+R_r^{'}/s)^2+X^{'2}} \tag{3.3}$$

Where

$$X^{'} = X_{\sigma r}^{'} + \frac{X_{\sigma s}}{1+\sigma_s} \tag{3.4}$$

is the transient rotor reactance of the induction machine.

It follows from (3.3), that by assuming the machine parameters constant, the electromagnetic torque is proportional to the square amplitude of the stator voltage for a given slip. By equaling the first derivative of (3.3) with respect to the slip to zero, $dT_e/ds = 0$, the critical slip (breakdown slip) is given by

$$s_{\max} = \frac{\pm R_r^{'}}{(R_s^2 + X^{'2})^{1/2}} \tag{3.5}$$

This slip corresponds to the maximum torque given by:

$$T_{e\max} = \frac{\frac{3}{\omega_1}\left(\frac{\left|\mathbf{U}_s\right|}{1+\sigma}\right)^2}{2\left[R_s \pm (R_s^2 + X^{'2})^{1/2}\right]} \tag{3.6}$$

Within (3.5) and (3.6), the 'positive' corresponds to the maximum motoring torque, which is also referred to as breakdown torque, the 'negative' is referred to as maximum generating torque. It can be seen that the maximum torque is proportional to the square of the stator voltage and it is inversely proportional to the transient rotor reactance $X^{'}$ of the IM. Considering only the motoring condition, it follows from (3.3) and (3.6) that the ratio of the torque and the breakdown torque can be expressed as

$$\frac{T_e}{T_{e\max}} = \frac{2(1+k)}{(s/s_{\max} + s_{\max}/s + 2k)} \cong \frac{2}{s/s_{\max} + s_{\max}/s} \tag{3.7}$$

Where

$$k = \frac{R_s}{(R_s^2 + X^{'2})^{1/2}} \approx 0 \tag{3.8}$$

Equation (3.7) implies that the steady-state torque, for the same value of the supply frequency and voltage, depends only on the slip; this relationship is almost linear for small values of the slip, where speed is close to the synchronous speed. In this case,

$$T_e \cong 2\frac{T_{e\max p}}{s_{\max}} s \tag{3.9}$$

Fig. 3-2 shows a typical torque-slip curve of IM in steady state for negative and positive slip *s*.

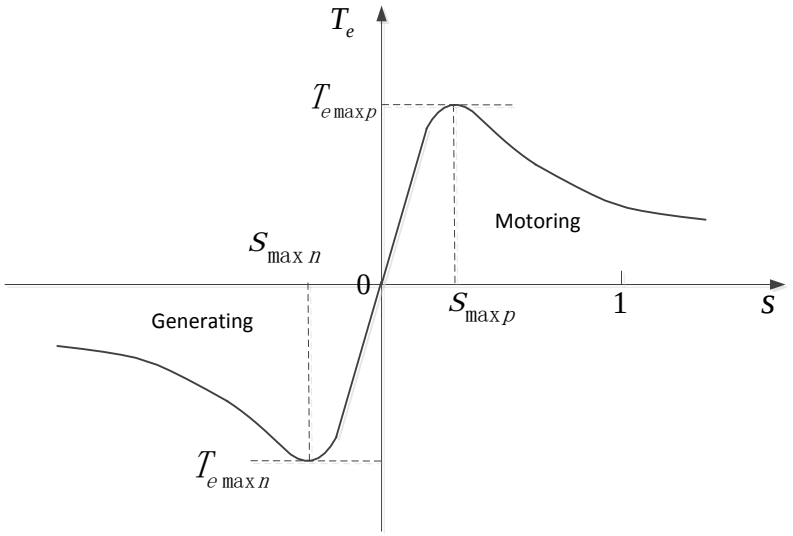

Fig 3-2 Torque-slip characteristic of an IM at steady-state

On the other hand, the flux linkage of an IM is related to air gap voltage as

$$\boldsymbol{\Psi}_m = \frac{\mathbf{E}_g}{j\omega_1} \tag{3.10}$$

The flux linkage can be maintained constant by keeping the ratio between air gap voltage and supply angular frequency constant. The rotor current can be rewritten from fig. 3.1 as a function of $\mathbf{E}_g$

$$\mathbf{I}_r^{'} = \frac{\mathbf{E}_g}{\frac{R_r^{'}}{s} + jX_{\sigma r}^{'}} \tag{3.11}$$

Meanwhile the expression for torque under the assumption of constant $\boldsymbol{\Psi}_m$, can be re-written as,

$$T_e^{E_g/f} = \frac{3}{\omega_1} \cdot \frac{\left|\mathbf{E}_g\right|^2}{\left(\frac{R_r^{'}}{s}\right)^2 + X_{\sigma r}^{'\,2}} \cdot \frac{R_r^{'}}{s} = 3\left(\left|\boldsymbol{\Psi}_m\right|\right)^2 \frac{s\omega_1 R_r^{'}}{R_r^{'2} + s^2\omega_1^2 L_{lr}^{'2}} \tag{3.12}$$

Where the superscript E_g/f denotes the assumption of constant flux linkage applied to (3.12). The slip at maximum torque can be given following the same procedure as (3.5)

$$s_{\max}^{E_g/f} = \frac{\pm R_r^{'}}{\omega_1 L_{lr}^{'}} \tag{3.13}$$

And the maximum torque is equal to

$$T_{e\max}^{E_g/f} = \frac{3}{2}\left(\frac{|\mathbf{E}_g|}{\omega_1}\right)^2 \frac{1}{L_{lr}^{'}} \tag{3.14}$$

A revised version of equation (3.9) under constant Ψ_m at speed close to the synchronous speed yields:

$$T_e^{E_g/f} \cong 2\frac{T_{e\max}}{s_{\max}} s = \frac{3}{2}\frac{|\mathbf{\Psi}_m|^2}{R_r^{'}} s \tag{3.15}$$

Equation (3.14) shows that the maximum torque is only dependent of the ratio E_g/f , and hence remains the same for constant E_g/f.

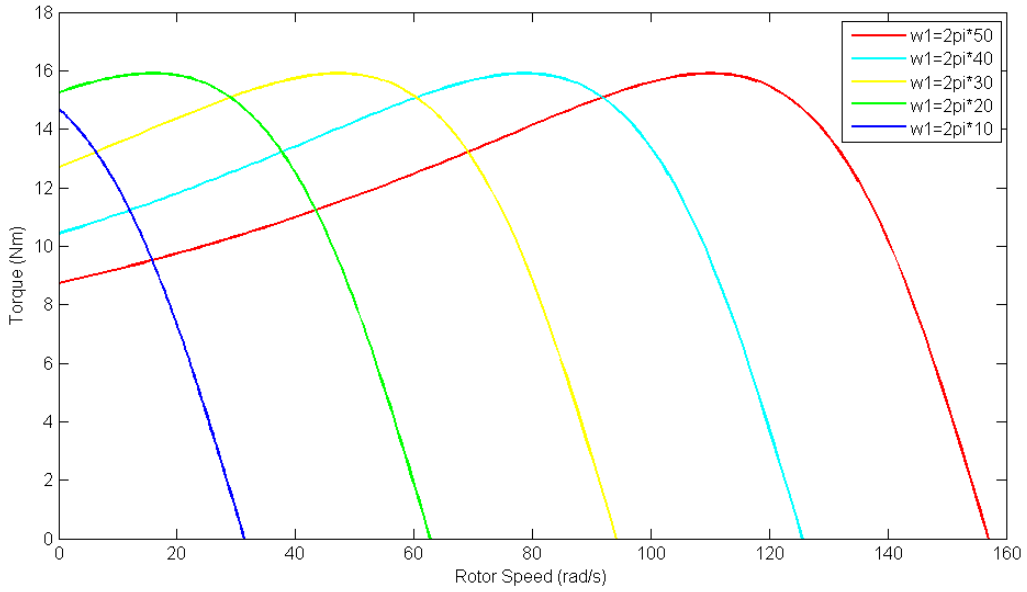

Fig 3-3 Torque-speed characteristic of an IM under constant E_g/f

Fig. 3-3 shows a set of the steady-state torque-speed characteristics of an IM under constant flux linkage for a 2.2kW machine, the parameters of this machine can be found in

chapter 4, section “test set-up”. This figure clearly shows that the higher the supply frequency, the higher the synchronous speed of the machine, as expected. Moreover, the lower the supply frequency, the higher the starting torque as long as the maximum torque is kept constant. The maximum torque remains almost constant while varying the frequency.

3.1.2 Open-Loop Scalar Control

Since it is impossible to control the air gap voltage E_g directly with a voltage-fed inverter, the practical way to control the speed of the IM is to open-loop regulate its supply frequency while simultaneously keeping constant the U_s/f ratio. So long as E_g is high enough, it is acceptable to ignore the voltage drop in the stator resistance and leakage inductance, and then to consider $U_s \approx E_g$: this happens for sufficiently high speeds.

Fig. 3-4 shows the block diagram of an open-loop scalar control scheme [2][72][73]. In this scheme, the gradient limiter reduces the bandwidth of the stator frequency reference. The band-limited stator frequency reference then generates the stator voltage reference magnitude while its integral determines the phase angle. The amplitude and phase of the reference stator voltage space-vector constitute the input of the space vector PWM system that, in turn, establishes the switching pattern of the inverter synthesizing the reference voltages.

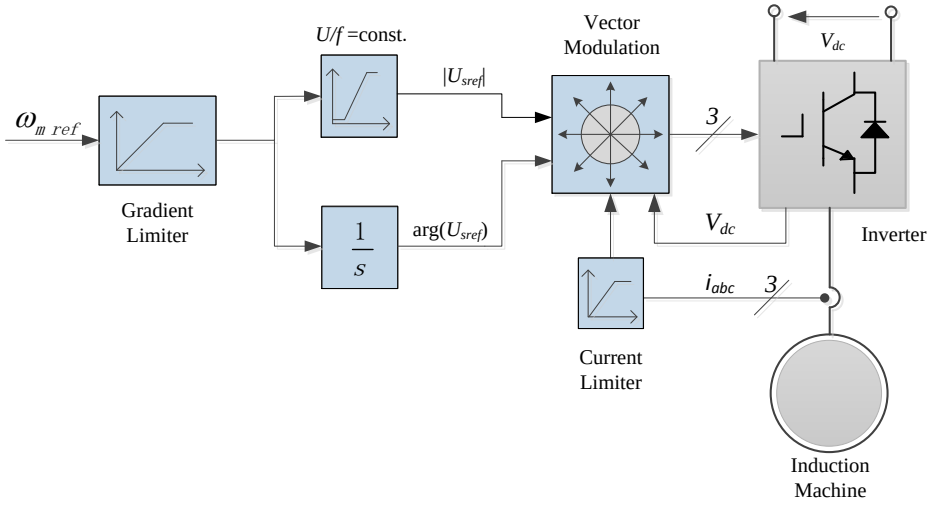

Fig 3-4 Block diagram of the open-loop scalar control.

The $|\mathbf{U}_s|/\omega_1$ ratio defines the rate of change of the linear function in fig. 3-4 and is usually set equal to the rated stator flux amplitude of the machine, $|\mathbf{U}_s|/\omega_1 = |\mathbf{\Psi}_{srat}|$, when the motor speed remains below the rated one. Above the rated speed, field weakening can be simply

achieved by limiting the voltage amplitude to the rated voltage of the machine, $|\mathbf{U}_s| = |\mathbf{U}_{srat}|$. At very low stator frequency, there is a pre-set minimum value of the supply stator voltage so as to account for the resistive stator voltage drop, $|\mathbf{U}_s| = |\mathbf{U}_{s\,min}|$. This is due to the fact that, because of a non-null value of the stator resistance, as long as the supply frequency reduces, the stator flux amplitude decreases too. A compensator can be deployed to take account of this voltage deeply as explained in 3.2.2.

Even if theoretically no stator current sensor is needed, since no direct current control is performed, in practical terms, it is frequently mounted to inhibit the switching of the inverter power devices for overload protection in the presence of over currents.

3.2 Closed-Loop Scalar Control

3.2.1 Closed-loop Scalar Control

Section 3.1 corresponds to varying only the synchronous speed of the drive, while maintaining U_s/ω_1 ratio constant, without the need of measuring the machine speed on the one hand, but without the possibility to compensate any variation of the speed caused by the load torque on the other hand. Thus, when more speed accuracy is required, the closed-loop control strategy should be adopted. The closed-loop control of the rotor speed can be achieved with the scheme in Fig. 3-5, where the speed PI controller employs the speed error signal to compensate the slip frequency.

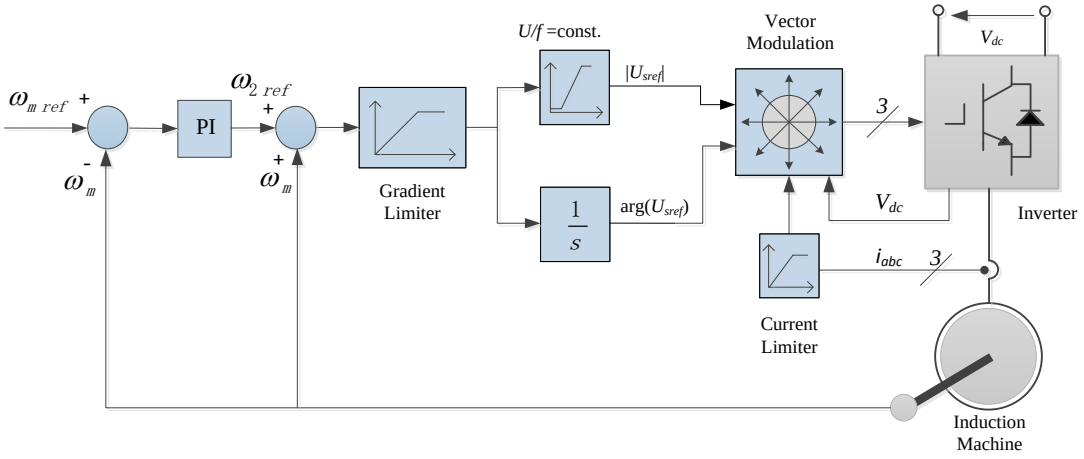

Fig 3-5 Block diagram of the closed-loop scalar control
with impressed voltages

In Fig. 3-5 to compensate for the slip frequency, the speed signal should be detected. The reference speed ω_{mref} is compared with the measured one ω_m, and the error is then

processed by a PI controller. The output of such a controller is the reference slip speed ω_{2ref} which, added to the measured speed, provides the stator pulsation reference ω_{1ref}. The reference slip speed must be properly limited to the range where the speed/torque relationship is almost linear, to avoid pull-out phenomena. Then the same structure explained in 3.2.2 is adopted.

3.2.2 Improved Closed-Loop Scalar Control

As explained in 3.1.2, the presumption that $U_s=E_g$ is not always true especially at low speed range, where E_g is not high enough, the voltage drop in the stator windings should also be considered. As a comparison, Fig 3-6 shows the torque-speed characteristics of the same 2.2 kW machine with constant U_s/ω_1.

From fig. 3-6, for a given supply frequency, it is clear that the breakdown slip is smaller than those in constant E_g/ω_1 condition and moreover the maximum torque cannot be kept constant; finally, the slip range corresponding to linear torque-slip characteristic becomes narrower. This becomes even worse at low speeds.

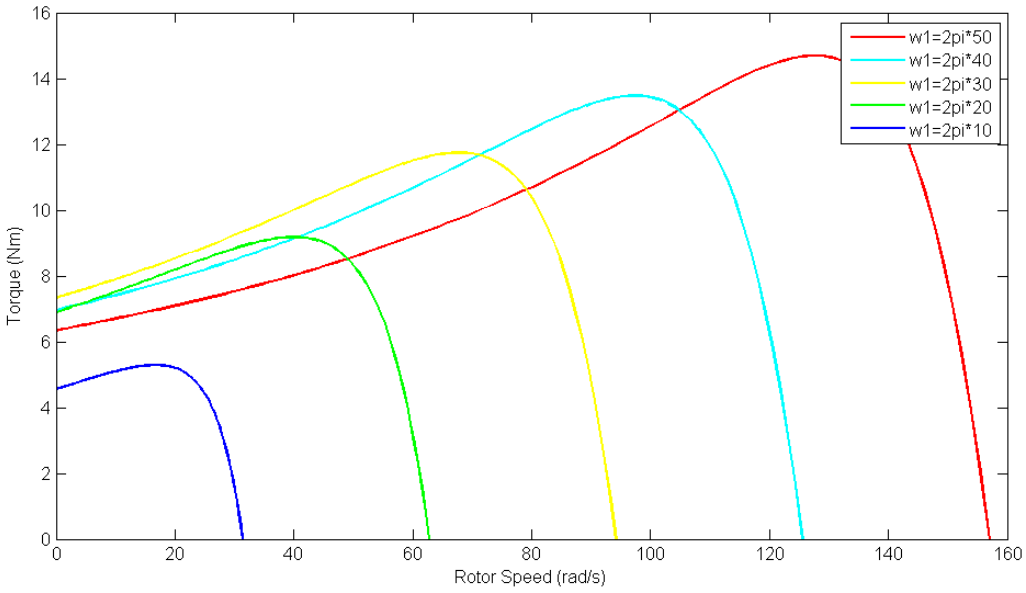

Fig 3-6 Torque-speed characteristic of an IM under constant U_g/f

A boost voltage is therefore required at low frequencies to compensate this voltage drop. However, if this voltage is high enough to give rated torque at standstill, when the excitation frequency is equal to the slip frequency, it will be too high however to allow the motor to

operate on no-load at this same excitation frequency for long periods, without excessive heating. In many drives this problem is circumvented by a special 'starting' procedure which applies a high boost voltage for only the few seconds required to start the motor while the running boost voltage is lower.

A more sophisticated method [68] is to correct the stator voltage reference on the basis of such a relationship, compensating the stator resistance ohm drop:

$$\mathbf{U}_s \cong \mathbf{\Psi}_m \left[\omega_1 + \frac{R_s}{R_r} \omega_2 \right] \tag{3.16}$$

where $\mathbf{\Psi}_m$ is the space-vector of the steady-state magnetizing flux, ω_2 is the slip pulsation, R_s and R_r are the stator and rotor resistances. On the basis of (3.16), the following simple stator resistance voltage drop compensation method has been adopted, to maintain the magnetizing flux amplitude constant, even under heavy load [68]:

$$\left|\mathbf{U}_s\right| = \frac{\left[\omega_1 + \frac{R_s}{R_r} \omega_2 \right]}{\left[\omega_{1rat} + \frac{R_s}{R_r} \omega_2 \right]} \left|\mathbf{U}_{srat}\right| \cong \frac{\left|\mathbf{U}_{srat}\right|}{\omega_{1rat}} \omega_1 + \frac{\left|\mathbf{U}_{srat}\right| R_s}{\omega_{1rat} R_r} \omega_2 = \mathbf{U}_{s1} + \mathbf{U}_{scomp} = \mathbf{U}_{stot} \tag{3.17}$$

This method relies on the realistic assumption that the rated pulsation in the denominator of the second term is much higher than the component dependant on the slip pulsation. The third term indicates that for low speeds the voltage component dependent of the slip pulsation is added.

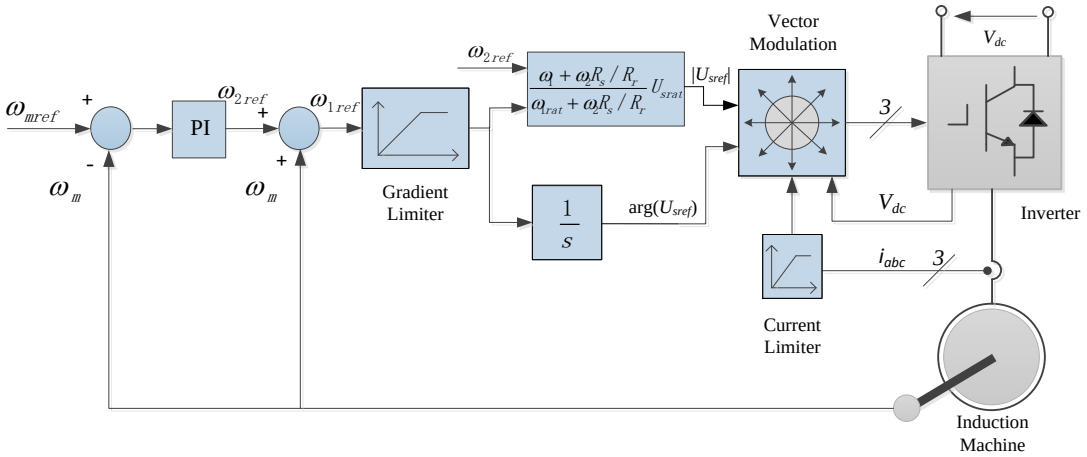

Fig 3-7 Block diagram of the improved scalar drive

Fig. 3-7 shows the block diagram of the proposed improved scalar controlled induction motor drive. The main difference here is that the voltage compensation part is introduced into the scheme.

3.3 Controller Design

The closed loop scalar control refers to the scheme of controlling the motor torque and speed by proportionally varying the voltage with supply frequency to keep the air-gap flux constant and achieve up to rated torque at any speed by controlling the slip pulsation. Equation (3.12) clearly shows that T_e is in proportional to the slip pulsation $s\omega_1 = \omega_2$, if E_g/ω_1 is kept constant. Thus, the torque developed by the machine could be controlled by acting on the slip pulsation ω_2. The closed-loop scalar control using a PI regulator can be modeled as in fig. 3-8:

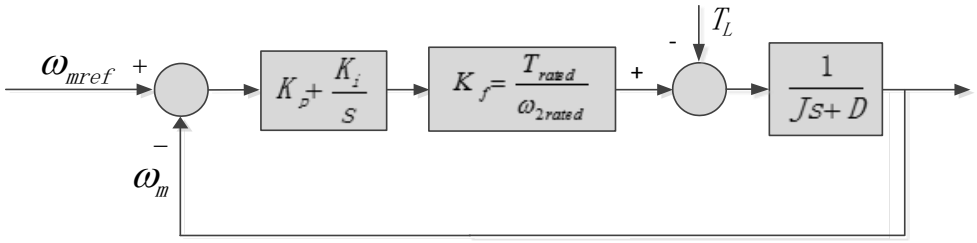

Fig 3-8 System model of IM with scalar controller

where J is the inertia of the motor and D is the friction coefficient The open loop transfer function of the machine under constant $|\mathbf{E}_g|/\omega_1$, assuming load torque T_L=0, is then given by the transfer function of the mechanic equation of the motor

$$G(s) = \frac{K_f}{Js + D} \qquad (3.18)$$

Where $K_f = \frac{T_{rated}}{\omega_{2rated}}$.

The design of the PI is therefore a simple exercise of compensation for linear system and any traditional compensator design technique can be used [74][75].

CHAPTER 4. SENSORLESS SCALAR CONTROL BY PLL SPEED ESTIMATOR

Extensive research has been done in sensorless control by using the retrieval of RSH. As far as the direct RSH tracking is concerned, two main approaches have been followed in literature [53][56][58-61][76-80]: Frequency domain methods, mainly based on FFT (Fast Fourier Transform)-like approaches, and time domain methods, most of which are PLL (Phase-Locked Loop)-like approaches. The sensorless techniques proposed in literature hardly comply with wide speed range operation, and actually results are usually presented only at rated or close to rated speed.

This chapter proposes a very simple sensorless technique based on a phase-locked loop (PLL) structure, suited for scalar controlled induction motor drives, where the centre bandwidth is tuned on-line on the basis of the reference values of the supply and slip frequencies provided to the PWM converter. The PLL is tuned to track the machine rotor slotting harmonic without the need of any high frequency signal injection, neither rotating nor pulsating. This results in tracking the machine speed in a very wide speed range (from rated speed down to as much as 2% of it) with a proper on-line adaptation of the centre frequency of the PLL. This has been made on the basis of the reference values of the fundamental supply pulsation and the on-line estimation of the slip pulsation. The methodology has been applied to a scalar controlled drive, with the aim of developing a low cost, computationally light sensorless drive, where the number of parameters to be tuned, both in the controller and in the estimator, is very limited in comparison with more performing sensorless drives. In particular, as for the control algorithm, only the PI control is to be tuned and only the stator and rotor resistances are to be known (only if voltage drop compensation is to be performed). As far as the PLL speed estimator is concerned, the only tuning parameters are the PLL gain and the cut-off frequency of its low pass filter while the only machine parameter to be known is the number of rotor slots per phase and per pole.

4.1 PLL Based Sensorless Scalar Control System

4.1.1 Phase-Locked Loop (PLL)

A PLL [81-88] is a circuit or software used heavily in communications engineering, radar, sonar, control engineering and many other applications. It makes an output signal synchronize with a reference input signal both in frequency and in phase. More precisely, the PLL is simply a servo system, which controls the phase of its output signal in such a way that the phase error between output phase and reference phase reduces to a minimum, so that the output and reference signal can operate at the same frequency.

A typical PLL is composed of a phase detector (PD), a low-pass filter (LPF), and a voltage-controlled oscillator (VCO) (see Fig. 4-1).

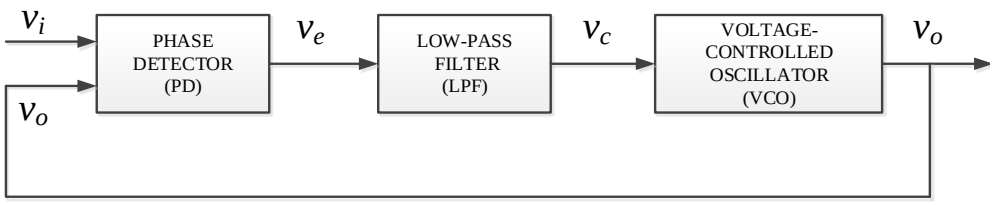

Fig 4-1 General Structure of PLL

The PD compares the reference signal v_i with the feedback signal v_o, producing a signal v_e that depends on the phase error between v_i and v_o. In this thesis a multiplier type PD is adopted, but other types of PD can be used [81].The PD is then followed by a low-pass filter (LPF), which eliminates higher frequency terms, so that only the DC component and lower harmonics v_e are left. The VCO generates an output signal v_o with frequency ω, which is dependent on the input voltage v_c. In general, without any input, the VCO generates by itself a signal of frequency ω_c, called centre frequency. When an input v_e is given, the VCO deviates from its central frequency ω_c, typically with a linear law, so that the output frequency is given by $\omega=\omega_c+Kv_e$. The output signal v_o will be then be $v_o=V_o\sin(\omega t+\varphi)$. Thus the complete system produces an output signal v_o synchronized in phase and frequency with the reference signal v_i once the PLL is in steady-state. Often the feedback signal v_o is a unit amplitude sinusoidal signal [81].

PLLs are often used because they provide filtering of a signal that is similar to what is provided to voltage or current waveforms by ordinary filters. The designer has some control over the manner in which the phase (or frequency) of the VCO follows a changing reference phase (or a changing reference frequency): the loop can be made to follow quickly or to

follow sluggishly, which is particularly valuable in removing the effects of noise on the reference. Actually PLLs can provide filtering that ordinary filters cannot do, because PLLs can follow a signal whose frequency varies slowly, that is, it acts like an adaptive filter that can track the signal frequency in a large range by adapting its center frequency, while rejecting all the noise provided that it is separated sufficiently in frequency from the signal.

In this chapter, PLL is introduced with carefully designed loop parameters and bandwidth so as to extract the rotor slot harmonics. Then a speed estimator based on it is adopted to estimate the rotor speed.

4.1.2 PLL Based Speed Estimator

The proposed PLL based speed estimator is based on processing the stator current waveform to track the rotor speed: the overall idea is to extract the rotor speed from the rotor slot harmonic f_h , as discussed in chapter 2. The centre bandwidth of the PLL is tuned online on the basis of the reference values of the synchronous and slip pulsation and is applied to the scalar control of induction motor drives, in which the supply and slip pulsation frequencies are obtained in the control loop (see chapter 3). The tuning of centre bandwidth is realized by changing the centre frequency of the VCO, like in conventional PLLs.

From eqn. (2.2), rewritten here for easy reference,

$$f_h = q_r f_1(1-s) \mp f_1 \tag{4.1}$$

the RSH appears at a certain frequency connected with the synchronous pulsation ω_1 and the slip pulsation ω_2. Considering that the rotor speed in electrical angle per second is given by $\omega_r = \omega_1(1\text{-}s)$, then the estimated mechanical rotor speed for a given RSH is given by,

$$\hat{\omega}_m = \frac{\hat{\omega}_r}{p} = \frac{\hat{\omega}_h + \omega_1}{pq_r} \tag{4.2}$$

Where ω_m is the estimated mechanical rotor speed (the symbol ^ refers to estimated) , the ω_1 is the reference supply pulsation, and p is the pole pairs Thus, a PLL speed estimator as the one shown in fig. 4-2 can be used to track the rotor speed.

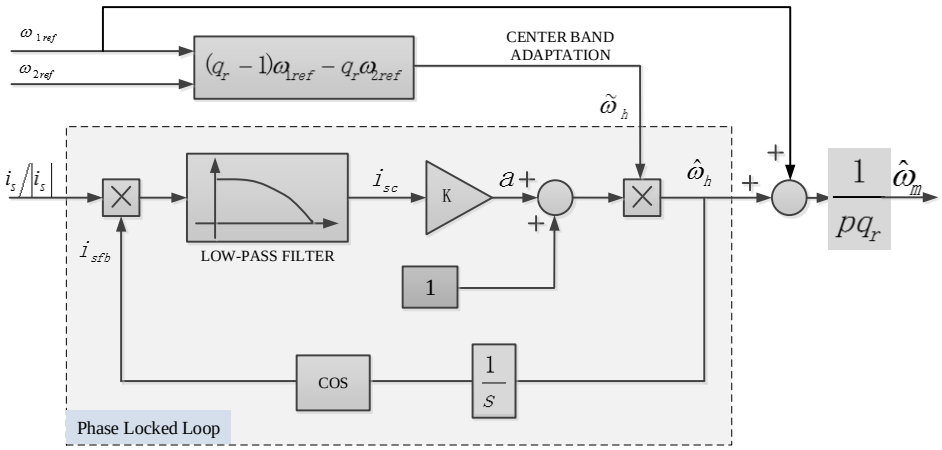

Fig 4-2 Block diagram of the PLL speed estimator

The induction motor stator current of one phase, including the slot harmonic, is firstly normalized to obtain a quantity of unitary amplitude. The PLL operates as a filter with a tunable band center $\tilde{\omega}_h$, computed by using the ω_{1ref} and the estimated slip pulsation ω_{2ref} on the basis of the following expression, directly derived by (2.2) using the lower rotor slot harmonic :

$$\tilde{\omega}_h = (q_r - 1)\omega_{1ref} - q_r\omega_{2ref} \tag{4.3}$$

In particular, a constant term equals to 1 is added to the variable *a*, obtained by the output of the low pass filter amplified by *K*. This sum is practically equal to the VCO of a common PLL, as seen in fig. 4-1 and accounts for the deviation from the central frequency: indeed this sum is denormalized by multiplication of the $\tilde{\omega}_h$, the central frequency, and is connected to the variation of the slot harmonics due to the speed variation. The output of this 'VCO' is the estimated pulsation $\hat{\omega}_h$ of the slot harmonics. The mechanical rotor speed is then computed on the basis of (4.2).

The only tuning parameters in the PLL are the gain *K* and the cut-off frequency of the low pass filter, while the only machine parameter to be known is q_r, number of rotor slots per phase and pole. The choice of gain *K* in fig.4-2 is critical for the PLL to work in a proper lock range narrow enough for including the slot harmonic frequency while rejecting the other harmonics as will be more clearly explained in section 4.2.2. As for the filter, a 4-order low-pass Butterworth filter has been chosen in this PLL scheme. Whenever the reference fundamental frequency ω_{1ref} coming from the scalar control part changes, or ω_{2ref}

changes because of the load condition, the PLL adapts itself to a new working band, but the loop gain and the cut-off frequency of the low-pass filter remain constant.

The whole PLL speed estimator is based on the PLL output which is the estimated frequency of the RSH $\hat{\omega}_h$, independently of the presence of the load and its amplitude, as well as of the drift of the machine parameters. Once the mechanical rotor speed $\hat{\omega}_m$ is computed on the basis of eq. (4.2), it is then given to the scalar control algorithm as the feedback signal.

4.1.3 PLL Based Sensorless Scalar Control Drive

Fig 4-3 shows the scheme of the adopted sensorless scalar control scheme based on PLL estimator. The scheme is exactly the same as the one in fig. 3-7 except that the measured speed is replaced by the proposed PLL speed estimator output.

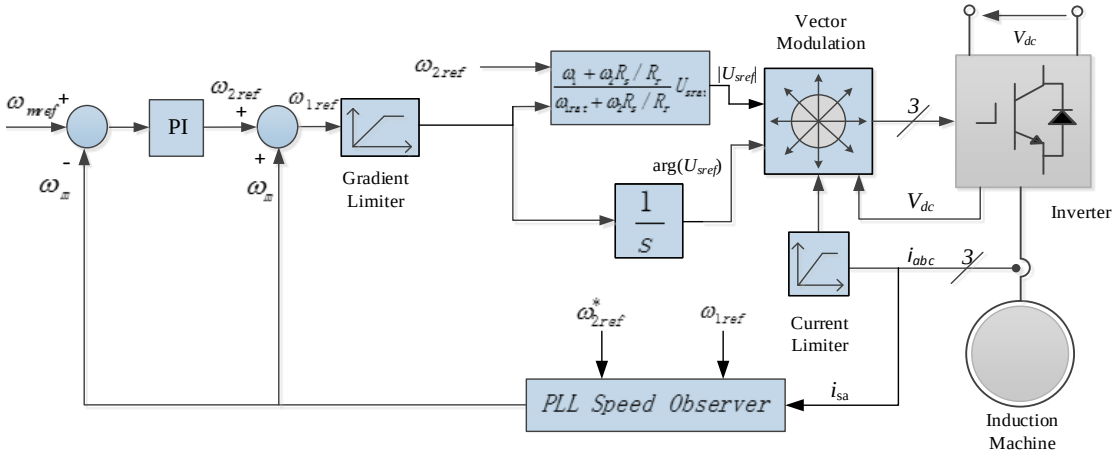

Fig 4-3 Scheme of Scalar Control Drive based on PLL

However, in the scheme, ω^*_{2ref} is not the one at the output of PI controller(see fig. 4-3 ω_{2ref}), but has been estimated using eq. (2.6) (see [1] pag. 414):

$$\omega^*_{2ref} = \frac{1}{p}\frac{L_m}{T_r|\Psi_r|^2}\left(\psi_{rd} i_{sQ} - \psi_{rq} i_{sD}\right) = \frac{1}{p}\frac{2R_r}{3|\Psi_r|^2} t_e \tag{4.4}$$

where i_{sD}, i_{sQ} are the stator currents components in the stator reference frame, $|\boldsymbol{\psi}_r|$ is the amplitude of the rotor flux and ψ_{rd}, ψ_{rq} its components in the stator reference frame, t_e is the electromagnetic torque, L_m and T_r are respectively the three-phase magnetizing

inductance and the rotor time constant. It should be noted that this flux estimator requires the knowledge of just two electrical parameters [2](p205).

It should further be noted that, in principle, the ω_{2ref} signal is already available at the output of the speed controller of the scalar control scheme. This signal cannot, however, be used in eq. (4.3) for the centre bandwidth adaptation since, otherwise, it would be used twice: 1) for the adaptation of the centre of the bandwidth, 2) for the compensation of the load torque in the control scheme. This means that the slip reference pulsation ω_{2ref} would be used to compute the estimated speed, by adapting the centre-band of the PLL, whose value would be then exploited to close the speed loop and therefore to compute the ω_{2ref} itself. As a result, the centre frequency of the PLL does not follow the slot harmonic, making then the PLL tracking a frequency which is not the correct one: thus the drive would have a weak load torque rejecting capacity.

4.2 PLL Mathematical Analysis

4.2.1 PLL Mathematical Description

As shown in Fig.4-2, the core of the PLL speed estimator includes a multiplier, a low-pass (LP) filter, and a pulsation produced by the signal i_{sc} and by the unit vector. In this case, a current controlled oscillator (ICO) rather than a VCO is to be envisaged.

The normalized phase stator current $i_s/|\mathbf{i_s}|$ (which is a periodical signal with maximal unit amplitude) can be expressed in steady state in harmonic form as:

$$i_s/|\mathbf{i}_s| = \left[\sum_{\substack{k=1 \\ k\neq h}}^{n} a_k \cos(\omega_k t + \theta_k)\right] + a_h \cos(\omega_h t + \theta_h) \tag{4.5}$$

Where a_h, ω_h, θ_h are the amplitude, frequency, and initial phase of the slot harmonic respectively; a_k, ω_k, θ_k are the same parameters for all of the harmonics, excluding the slot harmonic. At the start of the PLL action, if the central frequency $\tilde{\omega}_h$ is close enough to ω_h so that the PLL is inside the pull-in region and locks in (see below) , the feedback signal i_{sfb}, is given by:

$$i_{sfb} = \cos[(\tilde{\omega}_h + \Delta\tilde{\omega}_h)t + \varphi_0] = \cos(\omega_c t + \varphi_0) \tag{4.6}$$

Where $\tilde{\omega}_h$is the centre pulsating frequency, $\Delta\tilde{\omega}_h$is the correction of PLL ($\Delta\tilde{\omega}_h = a\tilde{\omega}_h$, where a is the normalized correction of the PLL), $\omega_c = \tilde{\omega}_h + \Delta\tilde{\omega}_h$, and φ_0 is the initial phase for $t=0$. After multiplication between $i_s/|i_s|$ and i_{sfb} , the signal i_{se} can be obtained as follows:

$$\begin{aligned} i_{se} = \frac{1}{2}\sum_{\substack{k=1 \\ k\neq h}}^{n} \left\{ \begin{matrix} a_k \cos\left[(\omega_k - \omega_c)t + \theta_k - \varphi_0\right] \\ + a_k \cos\left[(\omega_k + \omega_c)t + \theta_k + \varphi_0\right] \end{matrix} \right\} \\ + \frac{1}{2}\left\{ \begin{matrix} a_h \cos\left[(\omega_h - \omega_c)t + \theta_h - \varphi_0\right] \\ + a_h \cos\left[(\omega_h + \omega_c)t + \theta_h + \varphi_0\right] \end{matrix} \right\} \end{aligned} \tag{4.7}$$

When the PLL locks in, then $\omega_c \to \omega_h$, which means that, if the LP filter cut-off frequency is chosen low enough, all harmonic components of the first term of (4.7) and second component of the second term are cancelled out, and only the first component of the second term is present, since it is a DC component. The output of the LP filter is therefore.

$$i_{sc} = \frac{1}{2} K_f a_h \cos\left[(\omega_h - \omega_c)t + \theta_h - \varphi_0\right] \tag{4.8}$$

Where K_f is the gain of the LP filter.

The correction term a, once the PLL locks in at steady state (ss) is:

$$a^{ss} = \frac{1}{2} a_h K K_f \cos(\theta_h - \varphi_0) \tag{4.9}$$

During transient the correction term is simply:

$$a = K i_{sc} \tag{4.10}$$

From (4.6), it results that the feedback signal at steady state is

$$i_{sfb}^{ss} = cos[(\tilde{\omega}_h + \mathrm{a}^{ss}\tilde{\omega}_h)t + \varphi_0] \tag{4.11}$$

In transient

$$\omega_c = \tilde{\omega}_h + \Delta\tilde{\omega}_h = \tilde{\omega}_h + \mathrm{a}^{ss}\tilde{\omega}_h = \tilde{\omega}_h + K i_{sc}\tilde{\omega}_h \tag{4.12}$$

and in the steady state ($\omega_c = \omega_h$)

$$\omega_h = \tilde{\omega}_h + \mathrm{a}^{ss}\tilde{\omega}_h = \tilde{\omega}_h + K i_{sc}^{ss}\tilde{\omega}_h = \tilde{\omega}_h + \tilde{\omega}_h \frac{a_h K K_f}{2} \cos(\theta_h - \varphi_0) \tag{4.13}$$

From (4.13), the phase difference between input and the feedback signal can be expressed as

$$\varphi_0 = \theta_h - \cos^{-1}\frac{\omega_h - \tilde{\omega}_h}{\frac{1}{2}a_h K_f K\tilde{\omega}_h} \tag{4.14}$$

This means that when, for example, ω_h is exactly equal to the central frequency$\tilde{\omega}_h$, $\varphi_0 = \theta_h - \frac{\pi}{2}$, so $\theta_h - \varphi_0 = \frac{\pi}{2}$, or that the real slot harmonic is in quadrature with the feed-back signal (4.11). From (4.14), it is obvious that if $\omega_h - \tilde{\omega}_h$ exceeds the overall loop gain $\frac{a_h K_f K\tilde{\omega}_h}{2}$, the PLL cannot work.

4.2.2 PLL System Analysis

In the case under study, the output of the PLL $\hat{\theta}_h$ is the sum of terms, one depending on the PLL input θ_h, the other depending on the center band frequency $\tilde{\omega}_h$. Correspondingly, if the linearized system is represented as in Fig.4-4, two transfer functions can be defined as follows:

$$W_1(s) = \frac{\hat{\theta}_h(s)}{\theta_h(s)} = \frac{F(s)K(a_h/2)\tilde{\omega}_h}{s + F(s)K(a_h/2)\tilde{\omega}_h} \tag{4.15a}$$

$$W_2(s) = \frac{\hat{\theta}_h(s)}{\tilde{\omega}_h(s)} = \frac{1}{s + F(s)K(a_h/2)\tilde{\omega}_h} \tag{4.15b}$$

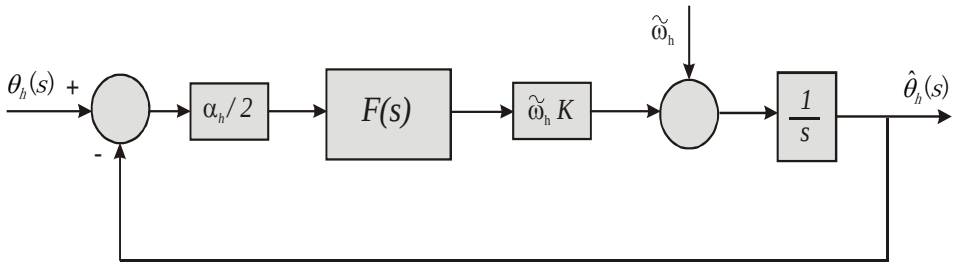

Fig 4-4 Linearized equivalent PLL transfer function

On this application a 4-th order Butterworth (Btw) LP IIR filter has been chosen as the low pass filter of the PLL, and the transfer function of the squared amplitude is given by:

$$F(s)F(-s)=\frac{1}{1+\left(s/j\omega_n\right)^8} \tag{4.16}$$

Where ω_n = 30 rad/s is the cut off frequency of the loop filter, K_f=1 is the gain of the filter. It should be noted that the choice of adopting a 4th order Butterworth filter instead of a simple 1st order one, as in the theoretical analysis shown above, is due to the necessity to obtain a stronger attenuation of the filter beyond its cut-off frequency. It does not in any case affect the reliability of the resulting analysis. The choice of a 4th order Butterworth filter is due to a trade-off between quick on-line and good high frequency attenuation.

The hold-in range is the span of frequencies from the centre frequency to the frequency where the PLL will remain locked after having been initially locked. This range can be shown to be in the region where the steady-state phase error remains linear. In the case under study the following relationship holds [81]:

$$\Delta\omega_{hold}=(a_h/2)\,K\,K_f\,\tilde{\omega}_h \tag{4.17}$$

where K_f=1 (gain of the 4th order Butterworth filter), K=0.04 (PLL gain) and a_h=0.05 (the amplitude of the fundamental of the measured stator current space-vector is equal to 1 and the RSH amplitude is almost as much as 2.5% of the fundamental).

The pull-in range is the span of frequencies from the centre frequency to the frequency where the system will initially lock in. This is a transient condition which is not easy to calculate exactly. For a type-I PLL with low-pass filter and sinusoidal phase detector, as the one adopted here, it can be approximated as follows [81]:

$$\Delta\omega_{pull}\cong 3\zeta\sqrt{\sqrt{0.423+1.2\zeta^4}-1.092\zeta^2}\,\Delta\omega_{hold} \tag{4.18}$$

where ζ is the damping ratio of the equivalent closed-loop 2nd order system.

Both $\Delta\omega_{hold}$ and $\Delta\omega_{pull}$ are very important parameters of the PLL. It is desirable to have those parameters as low as possible, to guarantee a suitable selectivity of the PLL: no other harmonics than the RSH should enter inside the band of the PLL. However, the lower the values of these parameter, the lower is the convergence speed of the PLL [81]. A trade-off between these two opposite exigencies should be then found.

In the case under study, $\Delta\omega_{hold}$ and $\Delta\omega_{pull}$ are both functions depending on the motor speed ω_m (Fig. 4-5). As expected, both of them increase linearly with the machine speed: at zero or close-to zero speed the hold-in range is almost null, which is the limit of PLL. At

rated speed the pull-in range is about 2 rad/s and the hold-in range is almost 1.3 times the pull-in one. The fact that the hold-in range reduces with the machine speed is an important issue, since the lower the machine speed, the closer to the RSH are the other harmonics: in this situation, a narrower hold-in range is desirable.

As for the dynamic behaviour of the proposed PLL, figs. 4-6, 4-7 show the Bode diagrams of the $W_1(s)$, $W_2(s)$ transfer functions. As for $W_1(s)$, it should be noted that, because of the variability of centre bandwidth, the cut-off frequency of the PLL and consequently its dynamics, varies with the supply frequency of the motor, ranging from 0.08 rad/s at f_1=1 Hz to 7 rad/s at f_1=50 Hz. This means that the capability of the PLL to work in a wide speed range is paid with the reduction of its dynamic behaviour at very low speed. As for $W_2(s)$, it should be noted that the presence of a variable centre bandwidth introduces a constant proportionality gain between $\hat{\theta}_h$ and $\tilde{\omega}_h$, which attenuates only when the PLL is out of its operating frequency region.

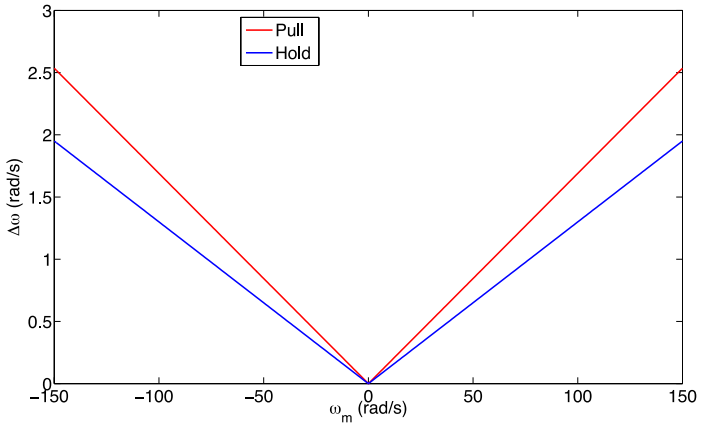

Fig 4-5 $\Delta\omega_{hold}$ and $\Delta\omega_{pull}$ versus ω_m

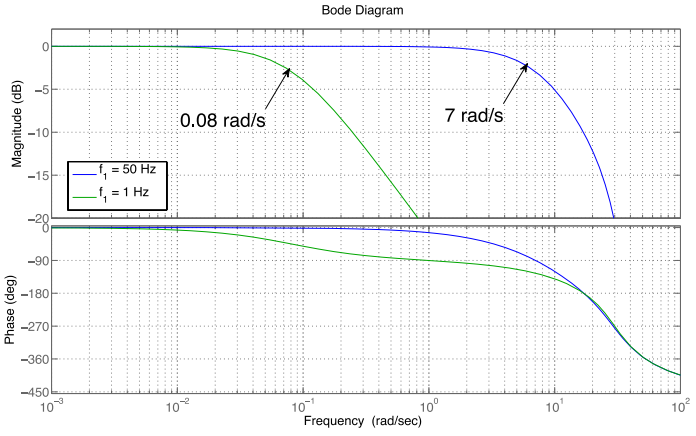

Fig 4-6 Bode diagram of the W_1(s) transfer function

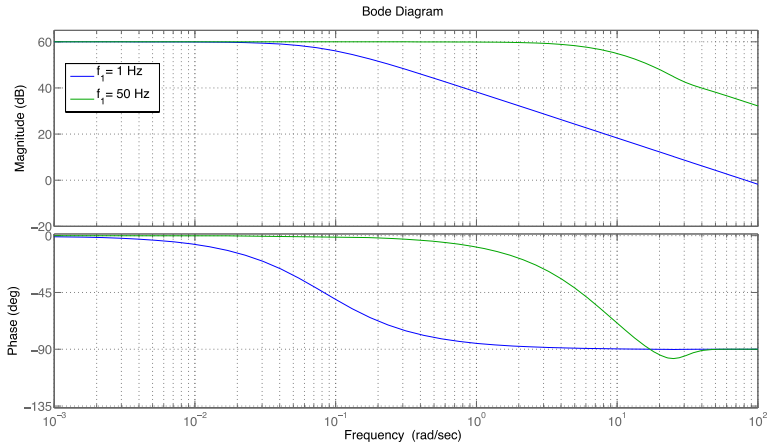

Fig 4-7 Bode diagram of the $W_2(s)$ transfer function

4.3 Simulation and Experiment Results

4.3.1 Test Set-up

The employed test set-up (see fig. 4-8) consists of:

- A three-phase induction machine with parameters shown in Table 4-1.

An 8 kVA, three-phase VSI for the control of the machine side inverter.

- A torque controlled brushless Interior Mounted Permanent Magnet (IMPM) machine drive for the load of 1.5kW.
- A dSPACE card (DS1103) with a PowerPC 604e at 400 MHz and a floating-point DSP TMS320F240 for the control of the machine side inverter.

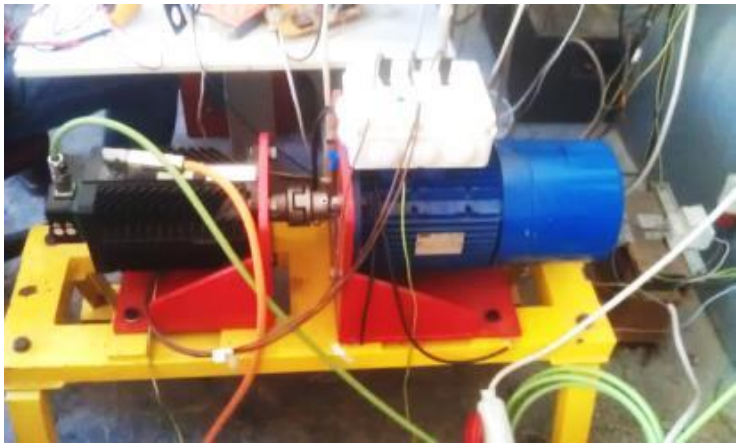

Fig 4-8 Photograph of the test set-up

Tab 4-1 Parameters of the induction machine

Rated power P_{rated} [kW]	2.2
Rated voltage U_{rated} [V]	220
Rated frequency f_{rated} [Hz]	50
Pole-pairs p	2
Stator resistance R_s [Ω]	2.9
Stator inductance L_s [mH]	223
Rotor resistance R_r [Ω]	1.52
Rotor inductance L_r [mH]	229
3-phase magnetizing inductance L_m [mH]	217
Moment of inertia J [kg·m^2]	0.0048

4.3.2 Simulation Results

The proposed PLL based scalar control system has been studied and tested in Matlab/Simulink environment and the same parameters of tab. 4-1 have been used. The space-vector dynamic model of the IM including rotor slotting effects, which was proposed in [41] is used for the simulation part (see Appendix A).

The simulation part is organized as follows. In part A, the proposed PLL speed estimator has been evaluated in the framework of the scalar control with measured speed feedback system (see fig. 3-7). Secondly, in part B, the measured speed was replaced by the PLL estimated one to close the loop so as to test the whole sensorless scalar drive system in a wide speed range with different load conditions (see fig 4-3).

A. The Verification of the Proposed PLL Speed Estimator

In this part, the speed tracking ability of the proposed PLL speed estimator has been evaluated, in the framework of the measured speed based scalar control system (see fig. 3-7): the PLL speed estimator is connected on-line along with the main scalar control loop, the centre bandwidth of the PLL $\widetilde{\omega}_h$ is calculated from ω^*_{2ref} and ω_{1ref}, where ω_{1ref} is the supply frequency of PWM and ω^*_{2ref} is estimated by (4.4). The output of the PLL is shown together with the measured speed for comparison. Both the robustness and the rapidity of response are then discussed.

However, to clearly illustrate the transient of the PLL estimator, a perturbation has been introduced into the value of ω^*_{2ref} obtained with eq. (4.4) (at t=3.5s deliberately), to show that the PLL is able to compensate the error. Moreover, since ω^*_{2ref} is merely a value estimated by eq. (4.4), and since this value can be disturbed by the noise, this test with a perturbation has also a real meaning. It should be noted that the slip pulsation in the output of PI remains unchanged in this test.

Figs. 4-9 show the results for rated speed at 10Nm load condition. The corresponding PLL estimator reference ω_{1ref} and ω^*_{2ref} are shown in fig. 4-9 a, the measured rotor speed ω_m and estimated rotor speed $\hat{\omega}_m$ are shown in fig. 4-9 b. Fig. 4-9 c shows the intermediate terms of the PLL estimator: the center bandwidth $\tilde{\omega}_h$, the estimated slot harmonics $\hat{\omega}_h$, the real slot harmonic ω_h, and the corresponding correction term a .

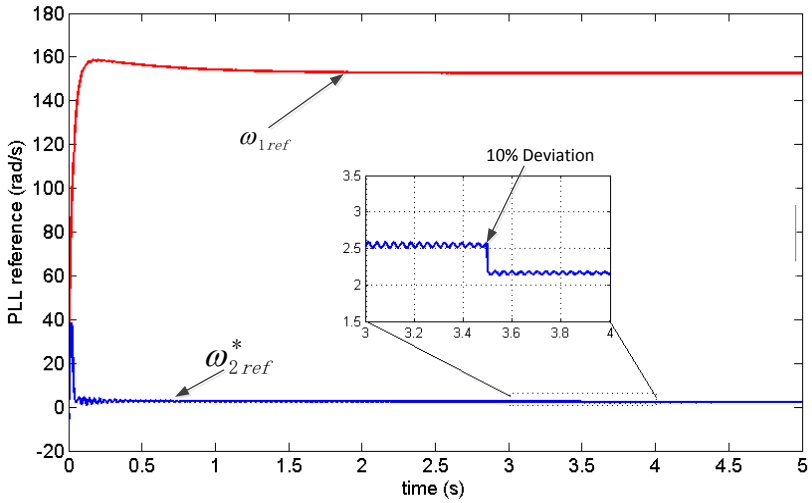

a) ω_{1ref} and ω^*_{2ref} (mechanical) with 150 rad/s reference full load

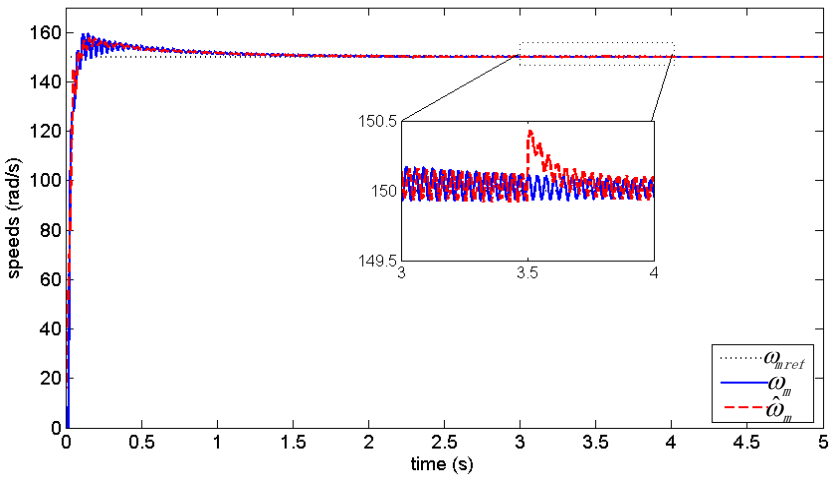

b) Rotor speeds at 150 rad/s reference full load

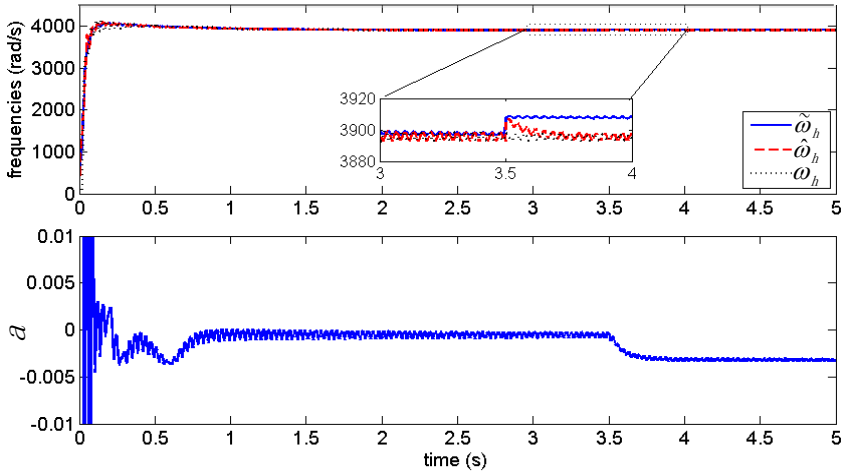

c) PLL intermediate terms

Fig 4-9 Verification of the PLL speed estimator at rated speed, 10Nm load condition

In fig. 4-9 a, a 10% deviation is added to ω^*_{2ref} on purpose at *t*=3.5s: ω^*_{2ref} steps down immediately from 2.5 rad/s to 2.2 rad/s , the value of ω_{1ref} remains unchanged, to the value of 153 rad/s at steady-state.

The magnified figure in fig. 4-9 b shows that the PLL estimated speed is very accurate at steady-state, and it restores the true speed within 0.4s after the disturbance of ω^*_{2ref}.

Fig. 4-9 c shows that the centre bandwidth $\tilde{\omega}_h$ is disturbed as much as 10 rad/s (0.3%), the estimated $\hat{\omega}_h$ however tracks ω_h within 0.4s, after the disturbance. Fig. 4-9 c shows the corresponding variation of the correction term a , which adjust itself after the perturbation of the centre bandwidth to track the slot harmonic ω_h.

The results also show that ω_h lies in the hold-in range of PLL even after $\tilde{\omega}_h$ is deviated, and during the transient after this deviation, the value of a varies to compensate the perturbation of ω^*_{2ref} (10% error in this case).

It should also be remarked that the hold-in and pull-in range of the PLL estimator cannot be too wide, otherwise the PLL would lock in other harmonics. In this study $\tilde{\omega}_h$ is a linear combination of ω_{1ref} and ω^*_{2ref}, or equivalently it is dependent on slip *s*. For small values of *s* (and for not too low speed) ω^*_{2ref} is small and has little impact on $\tilde{\omega}_h$: only 0.3% in the case under study (see fig. 4-9c, where $\tilde{\omega}_h$ =3910 rad/s and ω_h is 3900 rad/s). Since *s* is not too large, the RSH harmonics is far from the other harmonics, it is then not difficult to find a proper bandwidth for the PLL estimator.

Figs. 4-10 show the results at reference speed of 10 rad/s, with 10Nm load. With such low speed and load (great value of *s*) the RSH is much closer to the other harmonics, so any strong perturbation can make the PLL lose lock, so a deviation of 5% is given in this case.

Fig. 4-10a shows the waveform of PLL reference ω_{1ref} and ω_{2ref}^{*}, fig. 4-10b shows the measured rotor speed ω_m and estimated rotor speed $\hat{\omega}_m$ respectively, the center bandwidth of PLL $\tilde{\omega}_h$ and estimated RSH $\hat{\omega}_h$ are shown in fig. 4-10c, together with the corresponding correction term a .

From fig. 4-10a, ω_{2ref}^{*} steps down from 2.7 rad/s to 2.6 rad/s at 3.5s, after a 5% deviation is added, ω_{1ref} remains at 12.8 rad/s at steady-state.

Compared to the results at rated speed, the magnifying curve in fig. 4-10b) shows that the PLL estimator output is still satisfactory but worse than the one at rated speed. The restoring time of the PLL estimator is now near 0.7s in this case, which is slower than 0.4s for the rated speed. This is caused by two reasons: 1) the bandwidth of the proposed PLL estimator is smaller at low speed, 2) although ω_{2ref}^{*} changes less, ω_{1ref} in this case is much smaller, thus the disturbance introduced into $\tilde{\omega}_h$ is about 2%, which is larger than the rated case 0.3%.

Fig. 4-10c shows the value of $\tilde{\omega}_h$ and the estimated $\hat{\omega}_h$, the PLL output is always exactly equals to the real RSH frequency, which is at 254 rad/s in spite of the deviation of ω_{2ref}^{*}, which causes $\tilde{\omega}_h$ shift from 256 rad/s to 259.8 rad/s. The corresponding correction term a decreases simultaneously to compensate the error.

In the low speed range, any error in ω_{2ref}^{*} will affect $\tilde{\omega}_h$ significantly, and large ripples can occur in $\tilde{\omega}_h$. Thus on the one hand *K* should be increased to have a good Signal/Noise ratio, but on the other hand, *K* should be kept small to avoid other harmonics to enter the PLL: a compromise between these two aspects is therefore to be found.

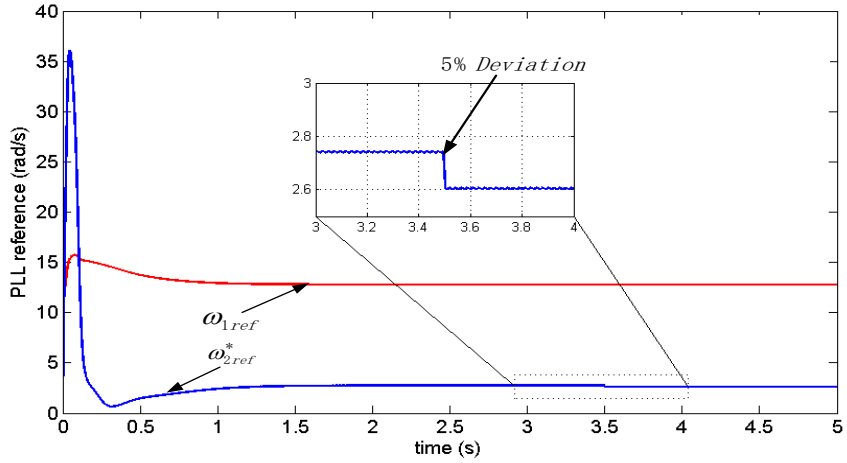

a) ω_{1ref} and ω^*_{2ref} (mechanical) with 10 rad/s reference full load

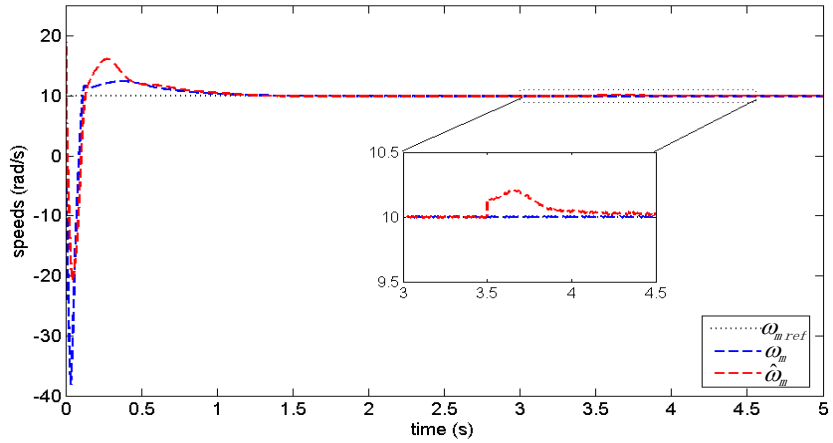

b) Rotor speeds at 10 rad/s reference, full load

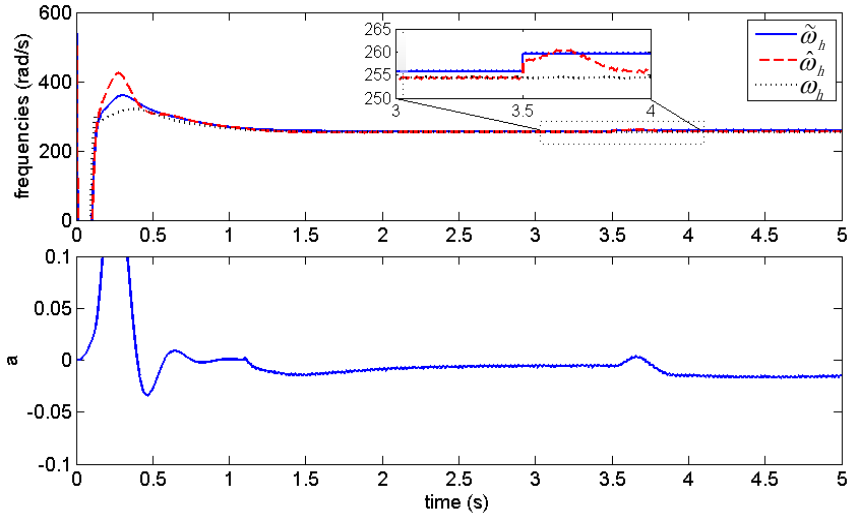

c) PLL intermediate terms

Fig 4-10 Verification of the PLL speed estimator at 10rad/s, 10Nm load condition

B. The Performance of the Sensorless Scalar Drive Based on PLL Estimator

The sensorless scalar drive based on PLL estimator has been tested in a wide speed range from 150 rad/s down to 2 rad/s, to evaluate the performance of the PLL based scalar control scheme. In these tests, the PLL estimated speed has been used as the feedback signal, while the measured speed has been shown in the figures for comparison.

The first set of tests refers to a speed step , both at no-load and full-load working conditions.

Fig 4-11a shows the speed step result at high speed range: the reference speed steps up from 50 rad/s to 100 rad/s at no load. The drive behaves properly: the rotor speed ω_{m} converges to the reference speed ω_{mref}, and the estimated speed $\hat{\omega}_m$ tracks the measured speed ω_m accurately in less than 0.5s.

The corresponding controller intermdiate terms, which are the supply pulsaton $\omega_{1\mathrm{ref}}$, the slip pulsation ω_{2ref} (mechanical angular pulsation), the supply voltage U_{s1}, the compensating voltage U_{scomp} (see eq. (3.17)), and the compensated voltage U_{stot} (the sum of U_{s1} and U_{scomp}), are shown in fig. 4-11b and fig. 4-11c. This figure clearly shows that the slip pulsation, very low at steady-state since at no load condition with only friction (its D=0.025), rises up during the transient. The supply U_{s1} follows ω_{1ref}, the compensating voltage U_{scomp} is close zero at steady-state, so that the compensated voltage U_{stot} is practically equal to U_{s1}.

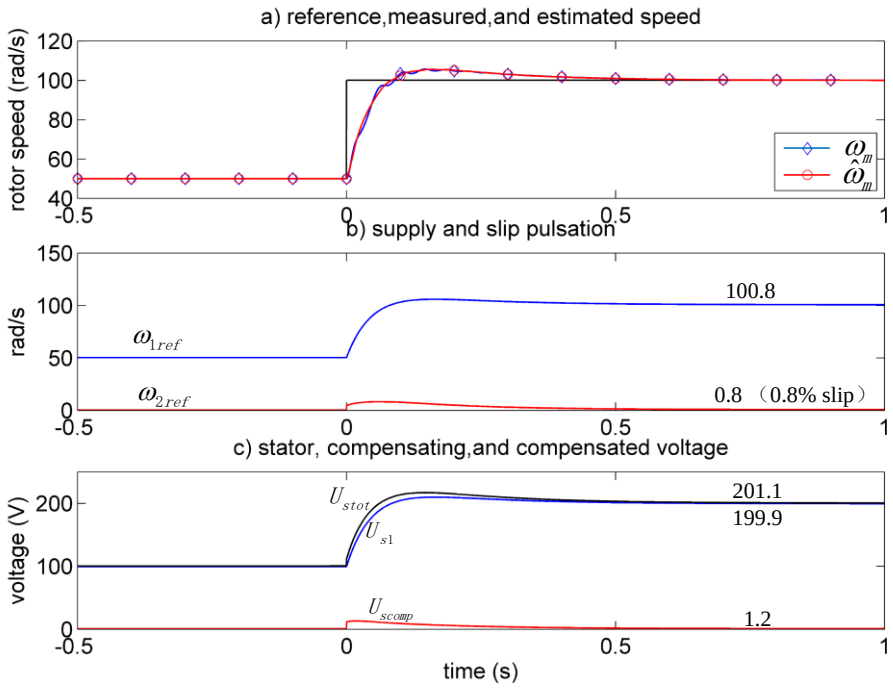

Fig 4-11 Reference speed steps from 50 to 100 rad/s at no-load

Fig. 4-12a , b and c show results for the same speed step test, however, at full-load(15Nm). From fig. 4-12a, the speed response curve is similar to the one for no-load case, and the drive behaves well with full-load.

Figs 4-12 b, c show the same test at full-load condition. In this case, ω_{2ref} and U_{scomp} are not zero anymore because of slip.

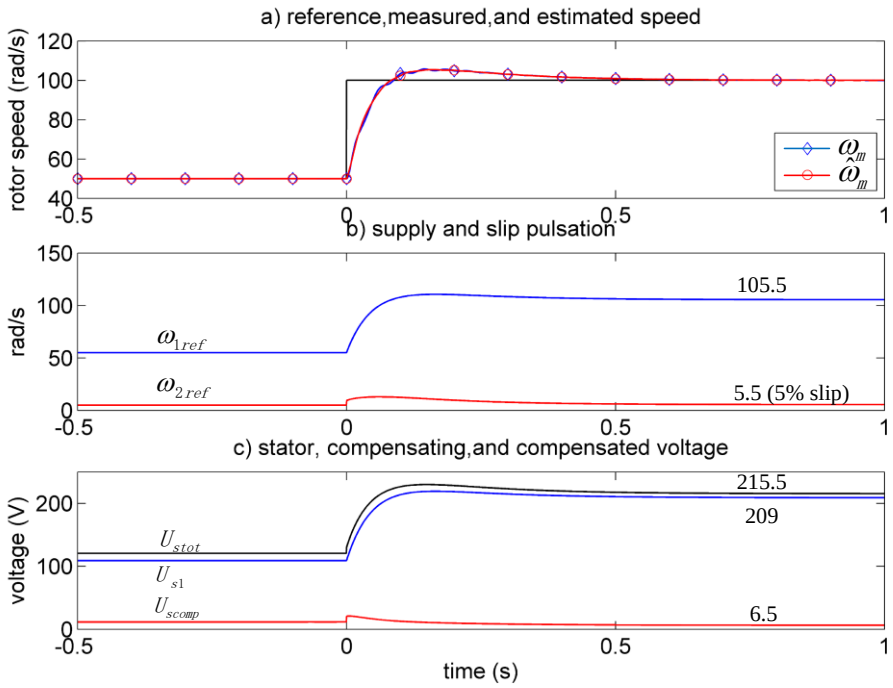

Fig 4-12 Reference speed steps from 50 to 100 rad/s at full-load

Figs 4-13 show the results for a speed step at low speed range, ω_{mref} goes up from 5 rad/s to 10 rad/s at no-load.

Fig. 4-13a shows that the drive works properly at steady-state, and during the transient an error is spotted between the estimated and measured speed, which however becomes almost null at steady-state. This behaviour is satisfactory since only the steady-state perfomance is of importance, since a scalar control is dealt with.

The corresponding intermediate terms are shown in fig. 4-13b and fig. 4-13c: the PI output ω_{2ref} is equals to zero and, correspondingly the zero compensating voltage.

Figs. 4-14 show the same results for full-load condition. Fig. 4-14a shows that the speed tracking performance is similar to the one at no-load, with an overshoot resulting in a longer settling time. However, the estimated speed converges to the measured speed before and quickly. Figs.4-14b, c present the corresponding intermediate terms of the controller. The

PI output $\omega_{2\text{ref}}$ is about 5.5 rad/s at steady-state, meanwhile, the compensating voltage increases because of the slip, along with the increase of $\omega_{2\text{ref}}$. For the same reason, the compensated voltage for the PWM is higher than the one for no-load.

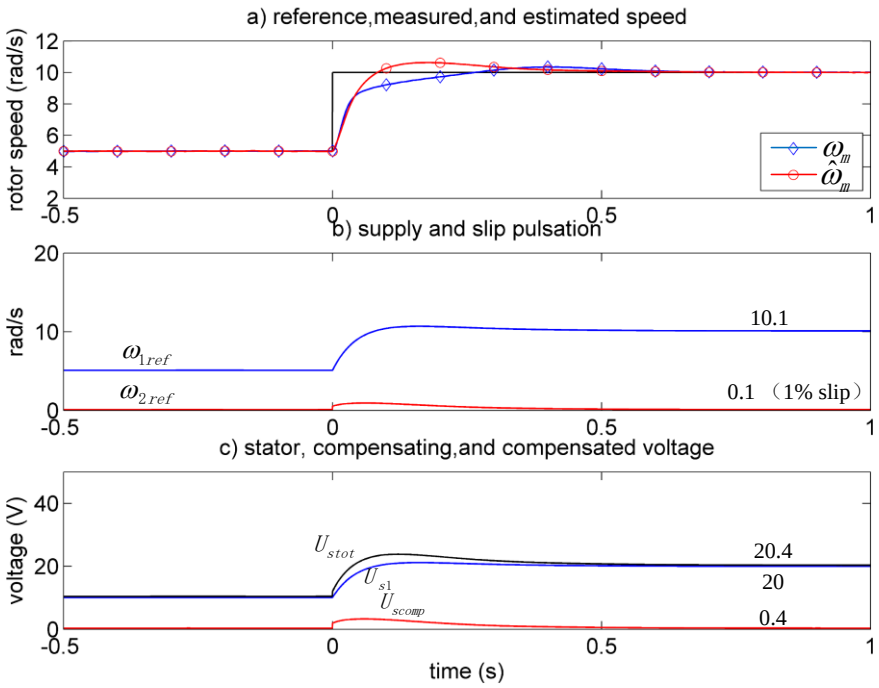

Fig 4-13 Reference speed steps from 5 to 10 rad/s at no-load

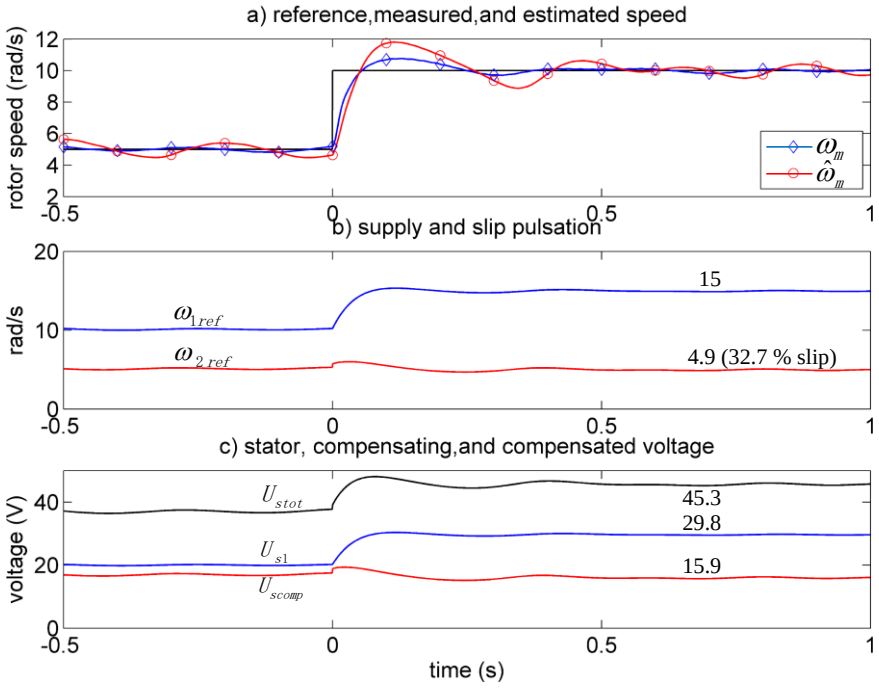

Fig 4-14 Reference speed steps from 5 to 10 rad/s at full-load

The second set of drive tests refer to the speed reversal, both at high and low speed range.

Fig. 4-15a, shows the speed reversal at rated speed from150 to -150rad/s, at no load condition. It can be found that the speed tracks the reference properly, although some oscilations can be observed during the trasient: this is largely due to the small inertia of the rotor; however no steady-state error is observed.

Figs. 4-15b and c show the corresponding PI output which is null all the time since $s \approx 0$. The compensated voltage U_{stot} is simply a constant multiple of the supply frequency. Actually the amplitude of the supply voltage remains constant before and after the reversal, but the phase sequence changes after the reversal, which does not affect the voltage terms.

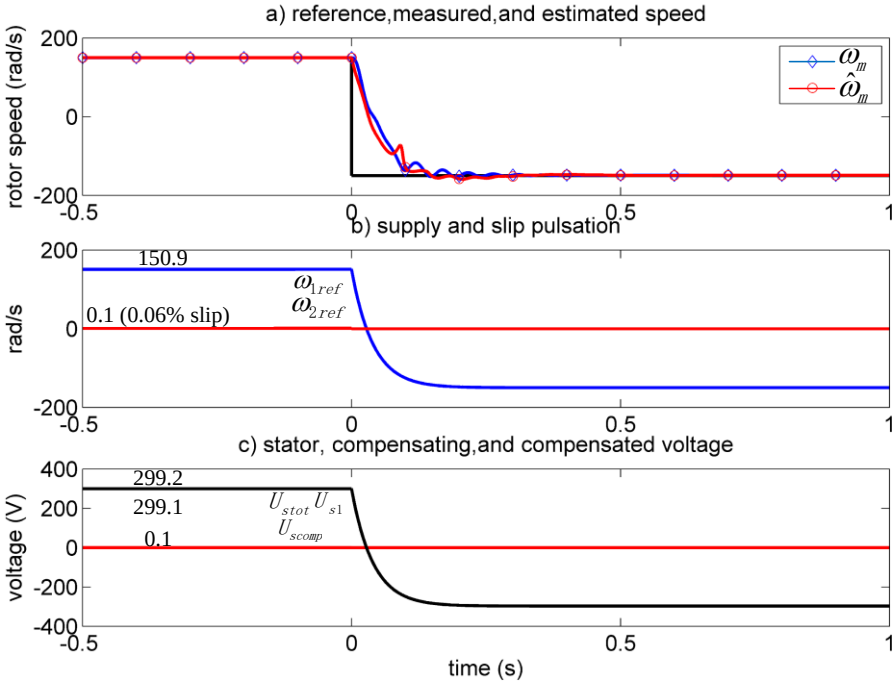

Fig 4-15 Reference speed reverses from 150 to -150 rad/s at no-load

Figs. 4-16 show the results for low speed reversal, from -5 rad/s to 5 rad/s, at light load (2Nm). Fig.4-16 a shows the esitmated speed $\hat{\omega}_m$, and the measured speed ω_m oscillate but they converge to the reference: $\hat{\omega}_m$ fluctuate more than the measured ω_m, making the speed tracking performance is still quite satisfactory at low speed.

Fig. 4-16 b presents a small ripple in ω_{2ref}, which is in accordance with the waveform of rotor speed response. The compensating voltage oscillates in the same way as ω_{2ref}, and eventually it converges to 1.1rad/s at steady-state.

Figs. 4-17 show the results for low speed reversal, from -10 rad/s to 3 rad/s, lightly loaded (2 Nm). The speed response performance is similar to the one from -5 rad/s to 5

rad/s. However, fig.4-17b shows that at steady-state the slip increases when the rotor speed decreases, while the slip pulsation remain ω_{2ref} almost the same, i.e. under the assumption of constant ψ_m, the output torque is in propotional to the slip pulsation $\omega_2 = s\omega_1$.

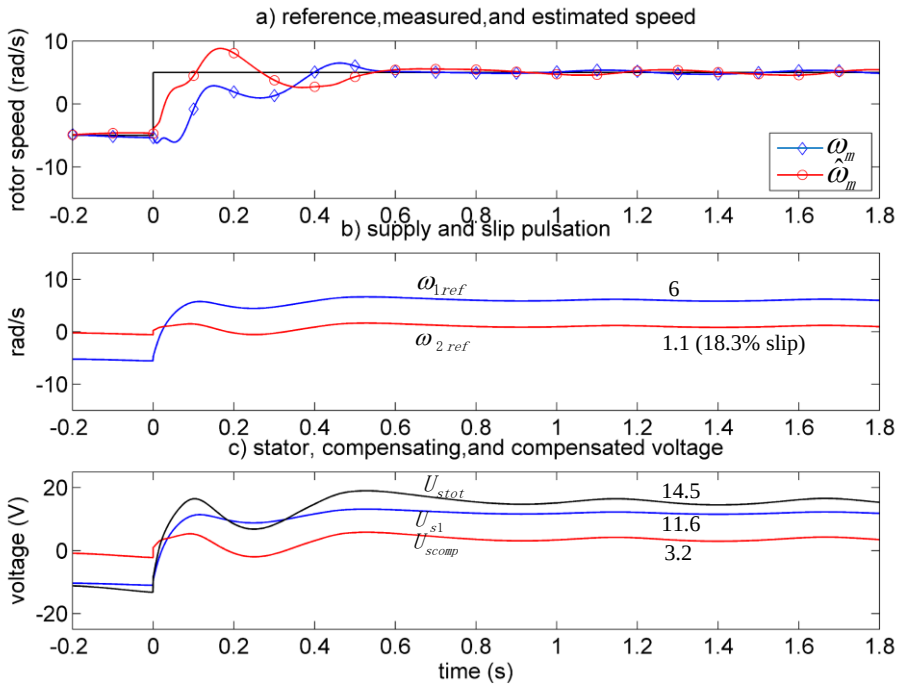

Fig 4-16 Reference speed reverses from -5 to 5 rad/s at 2Nm-load

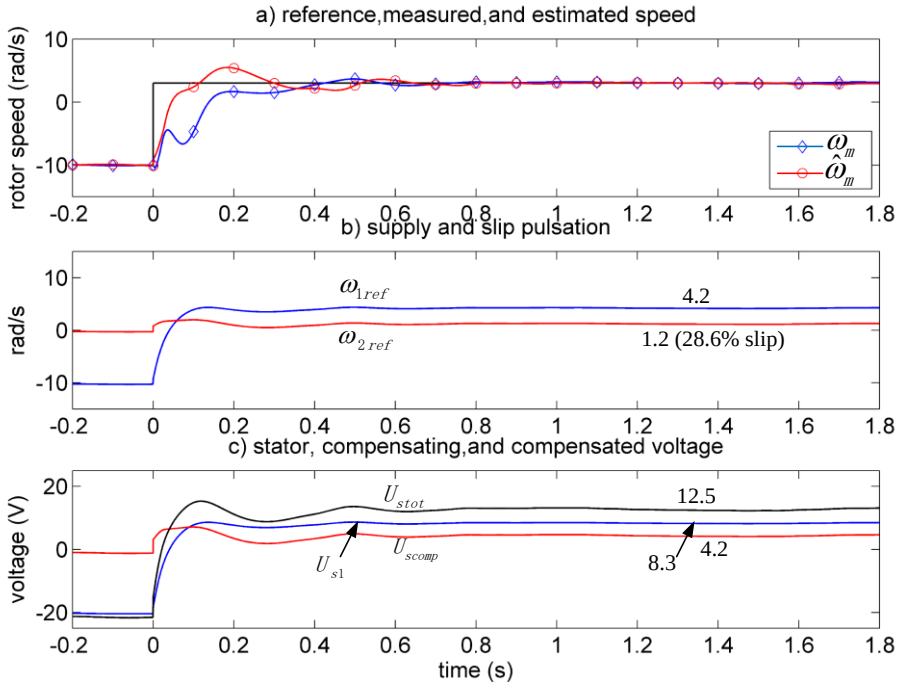

Fig 4-17 Reference speed reverses from -10 to 3 rad/s at 2Nm-load

The third set of tests refer to rejection to load torque steps: different load torques have been applied to the machine, operating at constant speed of 10 rad/s. The load torque steps occur according to fig.4-19, and the amplitudes range from 0 to 10 Nm.

Figs 4-18 show respectively the estimated and measured rotor speed ($\hat{\omega}_m$, ω_m),and the controller intermediate terms.

From fig. 4-18a, it can be found that the drive is robust to all the load torque step variations, the estimated speed tracks the measured and reference speed properly in about 0.4s. The compensating voltage term presented in fig. 4-18c increases with the high slip pulsation, which is exactly what was expected.

Even though the drive has a simple scalar control, fig. 4-19 shows that the electromagetic torque of the machine t_e responds quickly to load torque variations. A small bias is present due to friction.

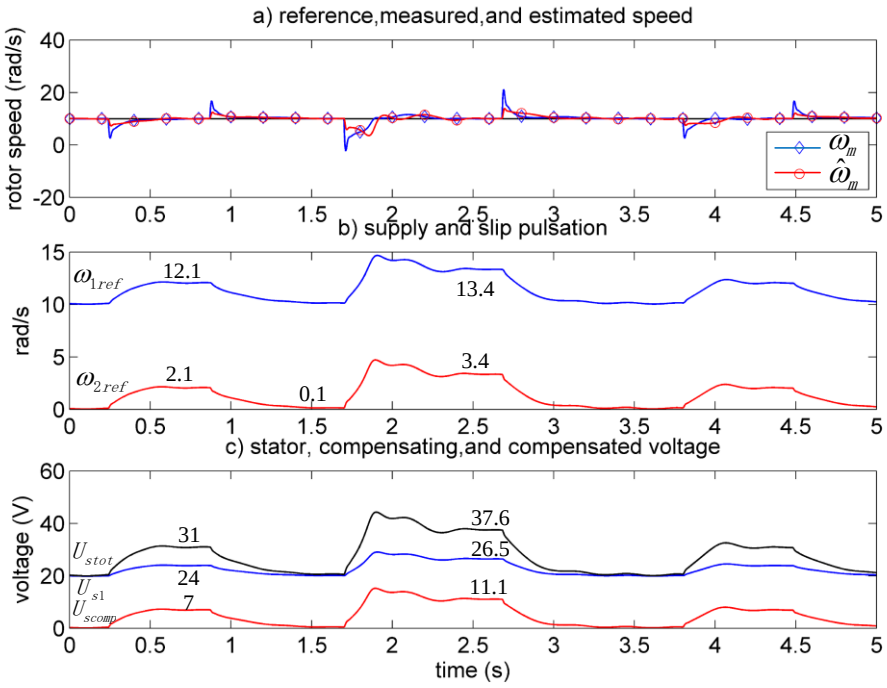

Fig 4-18 Rotor speed at 10 rad/s reference speed during load steps

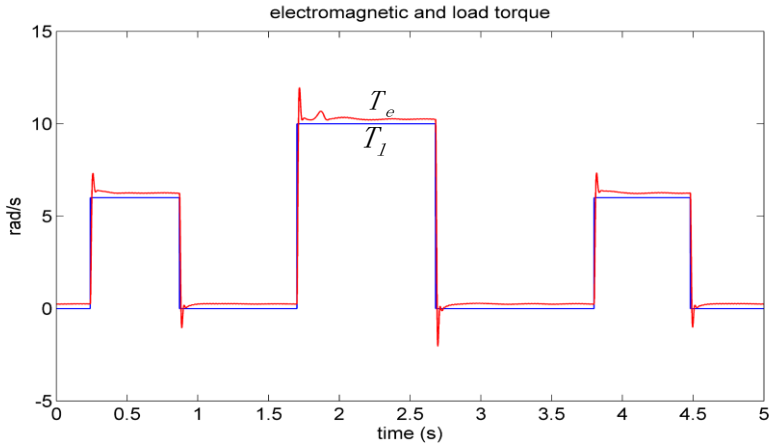

Fig 4-19 Electromagnetic and load torque at 10 rad/s reference speed during load steps

The last set of tests refers to the minimum possible working speeds of the drive.

Fig. 4-20 shows the reference, measured and the estimated speed during a constant speed reference of 3 rad/s (2% of the rated speed), at no-load and 5Nm load. They show clearly a very good behavior of the drive at 2% of the rated speed. The ripples for the full load condition is larger due to the bigger ripples in the $\tilde{\omega}_h$ as discussed in part A.

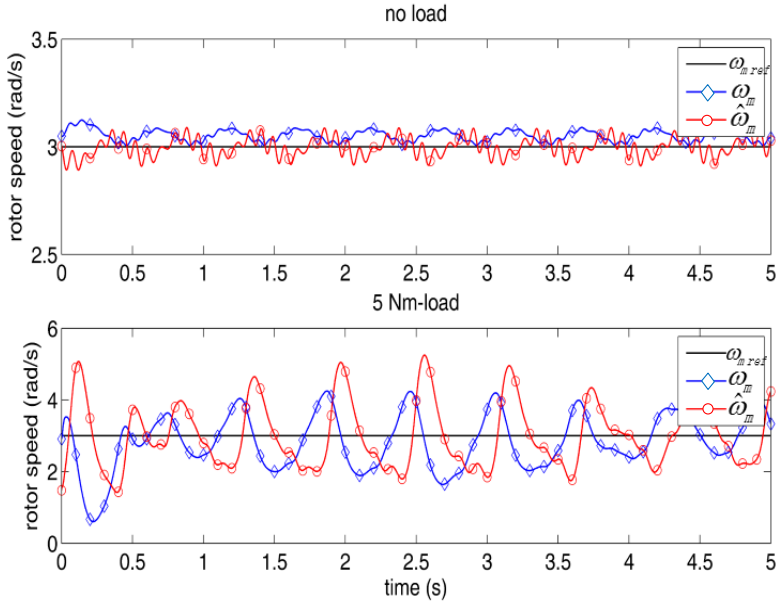

Fig 4-20 Reference, measured and estimated speed during constant speed operation at 3 rad/s

4.3.3 Experiment Results

The proposed scalar sensorless induction motor drive has been verified experimentally on the test set-up presented in section 4.3.1. For the experimental implementation of the PLL based speed estimator, the scalar control as well as the PLL have been implemented in the discrete z domanin adopting a sampling frequency of f_c=10 kHz. The PLL estimator has been tested in a very wide speed range, from rated speed (150 rad/s) down to 3 rad/s (2 % of the rated speed), showing the capability of the PLL technique to track the rotor slotting saliency in this very wide speed range. Moreover, the PLL estimator has been tested in both no-load and full-load working conditions. In the following, all the tests have been performed using the estimated speed as feedback signal, while the measured speed has been used only for comparison.

The first test refers to a speed reversal at the rated speed of the machine.

Fig. 4-21 a shows the reference, measured and estimated speed during a speed reversal from 150 to –150 rad/s (rated speed) at no load. It shows a very good behaviour of the drive, with the estimated speed properly tracking the measured one during the whole transient. Fig. 4-21 b presents the corresponding waveforms of the stator voltage amplitude terms, that is the U_{s1} term, the compensating term U_{scomp} and the compensated voltage U_{stot} as sum of the two. These terms are multiplied for the sign of the speed, including the sign of the voltage to be applied to counterbalance the back emf. It can be seen that the amplitude of the voltage varies during the speed transient, and the compensation term is maximum during the speed transient when the slip speed is maximum (maximum torque operation).

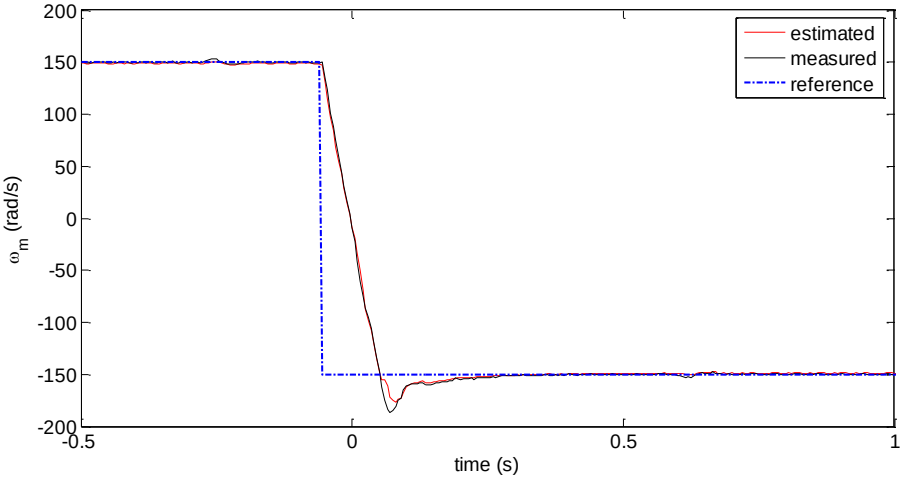

a) reference, measured and estimated mechanical speed

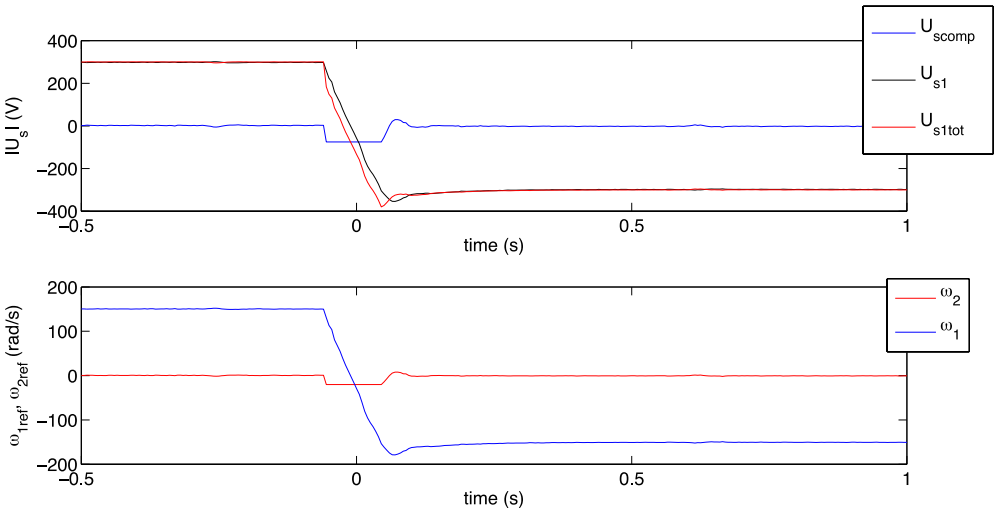

b) Stator voltage terms, supply and slip pulsations (mechanical)

Fig 4-21 The speed reversal test at no-load at high speed from 150 to -150 rad/s

The second test refers to the very challenging situation of a speed reversal at very low speed.

Fig.s 4-22 a and b show the same waveforms obtained during a speed reversal at low speed, from –5 rad/s to 5 rad/s (3.3 % of the rated speed), with a light load torque of 2 Nm (corresponding to about 15 % of the rated torque). It can be seen that the drive is able to accomplish the speed reversal at very low speed in almost 0.3 s, with an almost null speed estimation error at steady-state and with a short time lag between the estimated and measured speed, due to the reduced bandwidth of the speed estimator at low speed, as expected. It should be further noticed that such a speed reversal at low speed is particularly hard to be accomplished, since, besides the voltage compensation term, the flux amplitude of the machine at low speed reduces significantly and so does the torque capability of the machine correspondingly. Furthermore, when the machine is at zero or close to zero speed, during the transient, there is a time interval in which the flux amplitude is null. This explains the reduction of the bandwidth of the speed estimator at low speed. It is then clearly observable how the voltage compensation term is very useful in such a test at low speed, considering that the main voltage term and the compensation one present a comparable amplitude.

Fig.s 4-23 a and b show the same waveforms obtained during another speed reversal at low speed, from –10 rad/s to 3 rad/s (2 % of the rated speed), with a light load torque of 2 Nm (corresponding to about 15 % of the rated torque). Even these figures show the goodness of the proposed estimator, thanks to which the speed reversal at very low speed is

performed in about 0.6 s, with an almost null speed estimation error at steady-state even at 0.3 rad/s. The same kinds of consideration of the previous test hold for this one.

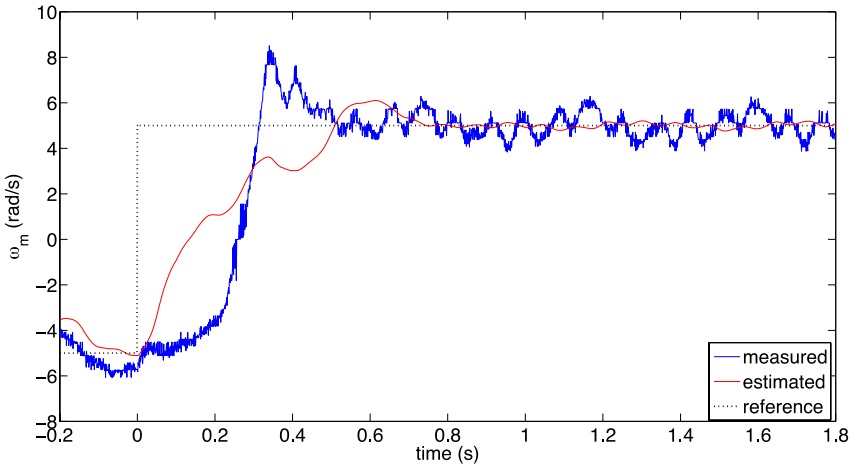

a). reference, measured and estimated mechanical speed

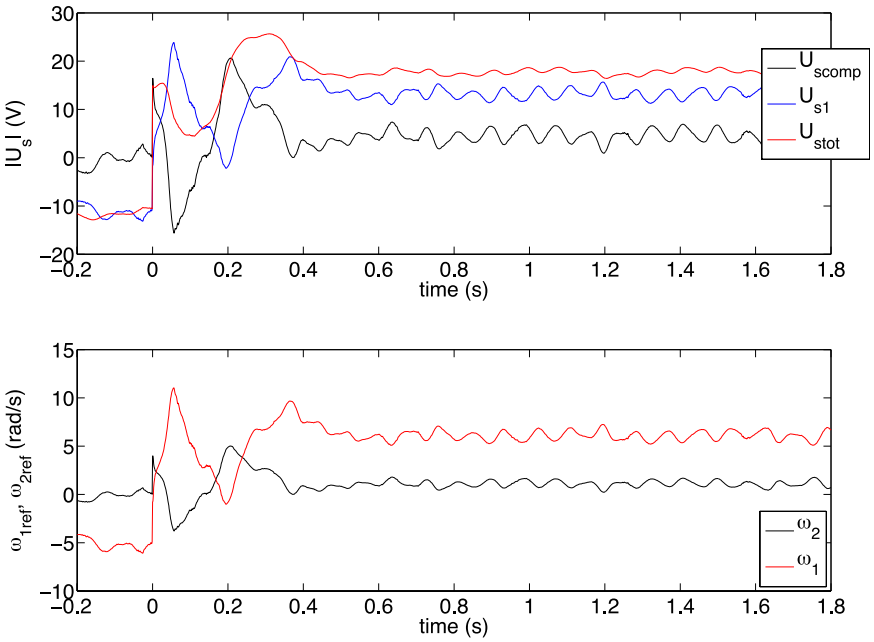

b) Stator voltage terms, supply and slip pulsations (mechanical)

Fig 4-22 The speed reversal test with 2Nm at low speed from -5 to 5rad/s

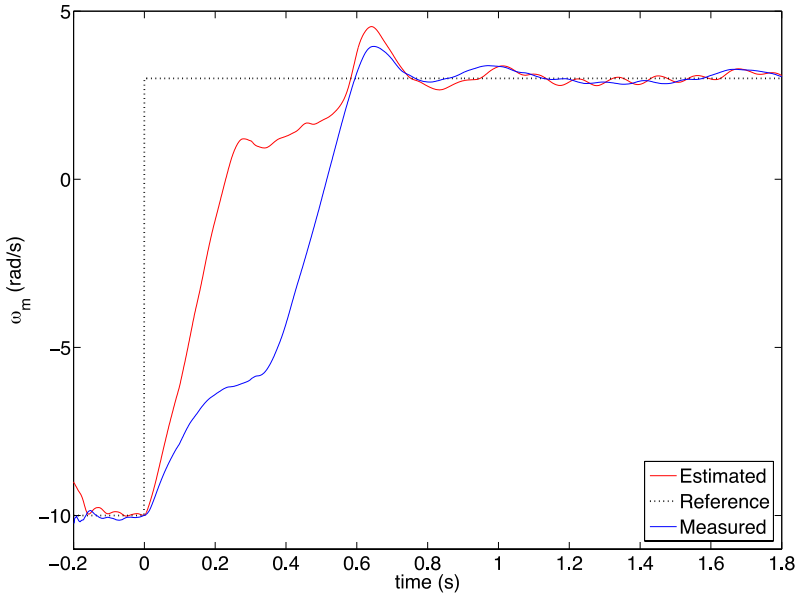

a). reference, measured and estimated mechanical speed during the speed reversal with 2Nm from -10 to 3 rad/s

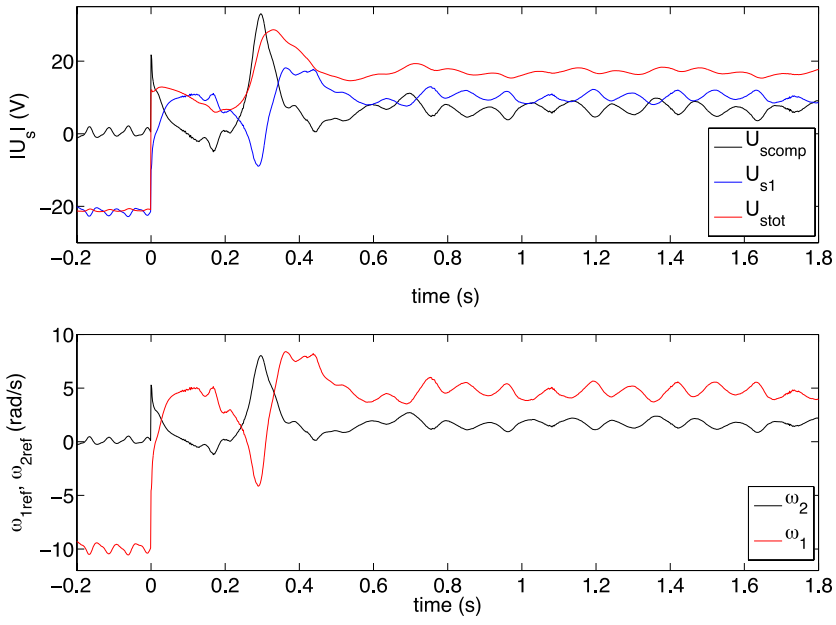

b) Stator voltage terms, supply and slip pulsations (mechanical)

Fig 4-23 The speed reversal test with 2Nm at low speed from -10 to 3 rad/s

The third test refers to the application of a square waveform of load torques at low speed. The drive has been given a constant low reference speed of 10 rad/s (6.6% of the rated speed), and then two subsequent very fast load torque square waveforms of time interval equal to 0.5 s and amplitude equal to 6 Nm and 10 Nm (rated torque). Fig.s 4-24a, b, c

show respectively the speed, the torque and the voltage waveforms. The speed waveform shows that the drive is able to properly counterbalance all the load torque step variations, with the estimated speed tracking the measured one and the reference one, even after a long speed transient with the speed of the machine assuming negative values during the transient. The torque waveforms show that the electromagnetic torque of the machine is able to track the load torque, with a very good dynamic performance, especially considering that the induction motor drive is controlled with a very simple scalar controller. Finally, the voltage waveforms show an increase of the voltage term U_{s1} because of the increase of the supply frequency and also a higher increase of the additional voltage term due to the very high increase of the slip speed.

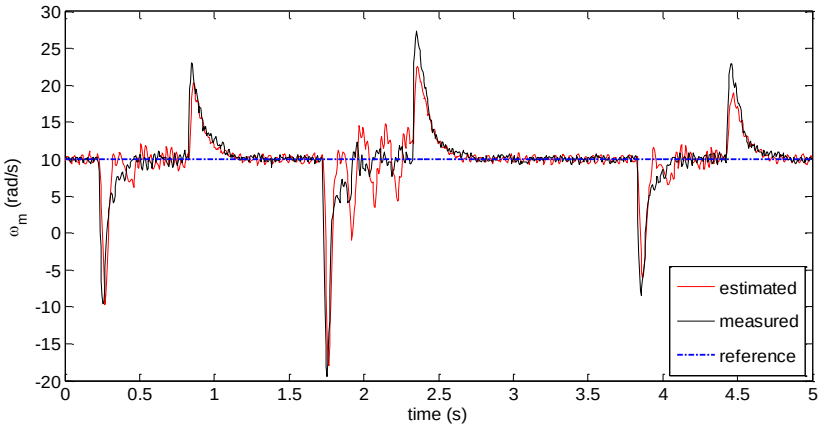

Fig. 4-24a. Reference, measured and estimated mechanical speed during the subsequent load torque steps at constant speed of 10 rad/s

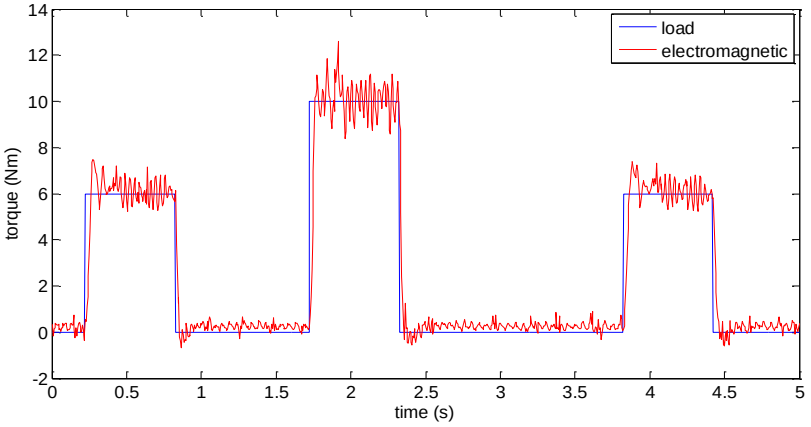

Fig. 4-24b. Electromagnetic and load torques during the subsequent load torque steps at constant speed of 10 rad/s

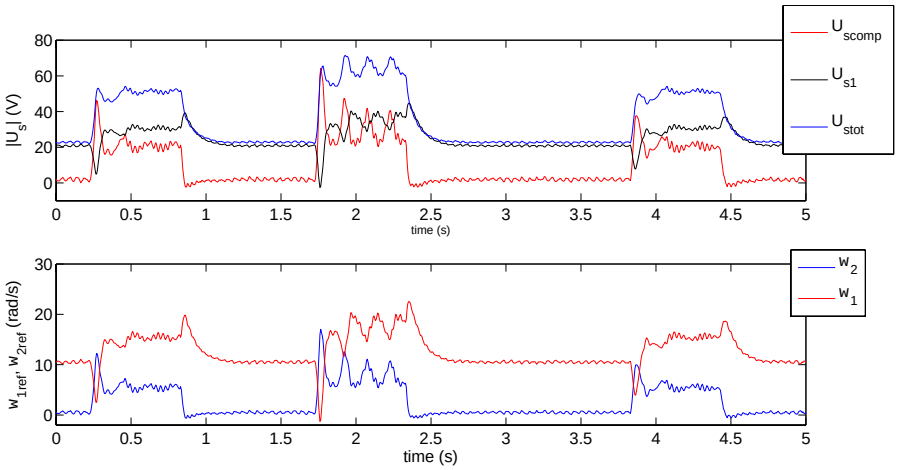

Fig 4-24 c. Stator voltage terms, supply and slip pulsations during the subsequent load torque steps at constant speed of 10 rad/s

The fourth test refers to the minimum possible operating speed of the drive. Fig. 4-25 shows the reference, the measured and the estimated speed during a constant speed reference equal to 3 rad/s (2 % of the rated speed), at no-load and at 5 Nm load torque. These figures show clearly a very good behavior of the drive at 2 % of the rated speed, at both no-load and half of the rated load. These figures show also an increasing ripple of the estimated and measured speed, especially at load, due to the presence of other spectral lines than the PSH: these enter the bandwidth of the PLL and so limit the PLL operation close to zero speed.

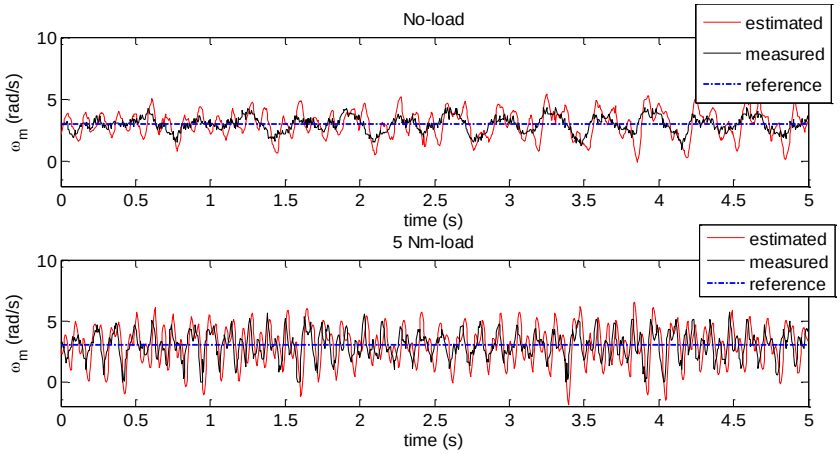

Fig 4-25 reference, measured and estimated speed during the constant speed operation at 3 rad/s at no-load (up) and at 5 Nm load (down)

4.4 Summary

The simulation and experimental results show the PLL is able to properly track the machine speed in a very wide speed range; the results also show a proper behaviour of the

scalar sensorless drive in a very wide speed range from rated speed down to 2% of the rated speed, at no load and with load conditions. Moreover experimental results are in high accordance with the simulation ones and with the theoretical analysis.

The speed estimation has been performed on the basis of a PLL algorithm, whose centre bandwidth is tuned on-line on the basis of the reference values of the supply and slip frequencies provided to the PWM. The speed estimation performed on the basis of a PLL algorithm is of a particular interest in terms of a potential industrial applications: if applied to a simple scalar control it requires both a very limited numbers of tuning parameters (PI of the speed control and the gain and cut-off frequency of the filter PLL), and the knowledge of very few machine parameters (stator and rotor resistances, and the number of rotor slots per phase and per pole). This makes the methodology easily exportable to several other types of drives.

.

CHAPTER 5. SPEED ESTIMATION BY ADALINES AND MCA EXIN NEURAL NETWORKS

To retrieve the PSH, chapter 4 describes the PLL (phase-locked loop), whose centre frequency adapts according to the working condition of the machine, and whose linearized transfer function is,

$$W_1(s)=\frac{\hat{\theta}_h(s)}{\theta_h(s)}=\frac{F(s)K(a_h/2)\tilde{\omega}_h}{s+F(s)K(a_h/2)\tilde{\omega}_h} \tag{5.1}$$

(see chapter 4 for the symbols)

The corresponding tracking error to a step of the PSH frequency, $\frac{\Delta\omega_h}{s}=\frac{s\Delta\varphi_h}{s}$, is given by:

$$\lim_{t\to\infty} e(t)=\lim_{s\to 0} s\cdot\frac{\Delta\varphi_h s}{s}\cdot W_{1e}(s)=0 \tag{5.2}$$

$W_{1e}(s)$=1-$W_1(s)$ is the error transfer function for (5.1).

From (5.2), it is obvious that the PLL has zero tracking error with input frequency steps. However, under the framework of PLL, the frequency output become correct after the phase is locked, this usually results in a longer settling time, or in worst case, ex. step of phase angle, causes the spurious transient frequency, and it takes typically many circles for the PLL to relock the phase.

To improve the speed estimation performance, in this chapter, the slot frequency is estimated by ADALINEs and MCA EXIN Neural Networks. First, two cascaded ADALINEs are used to extract the rotor slot harmonic from the input stator phase current, acting as adaptive filters and whose output consists only of the slot harmonic. Then, the MCA EXIN neurons are used to extract the eigenvector corresponding to the minimum eigenvalue of the autocorrelation matrix formed by the ADALINEs' output sequence: as a matter of fact the slot frequency can then be estimated by finding all the roots of the polynomial equation formed from this eigenvector by using Pisarenko's theory. Moreover not only can the proposed neural network work recursively sample by sample, but the computational

complexity and mean square frequency estimation errors are largely reduced. Finally, like the PLL observer, the rotor speed can then be computed by (2.5).

5.1 Retrieval of Rotor Slot Harmonics

5.1.1 ADALINE

A linear adaptive neuron (ADALINE) is a single layer artificial neural network which can be used as a notch filter or a band filter [2][89-91]. This means that the neuron is either able to cancel a determined signal at a certain frequency (notch filter), or it is able to let a determined signal pass at a predefined frequency (band filter, where band stands for a band of signals in a very narrow range around a predefined frequency).

Fig.5-1 shows the notch/band ADALINE with two adaptive weights.

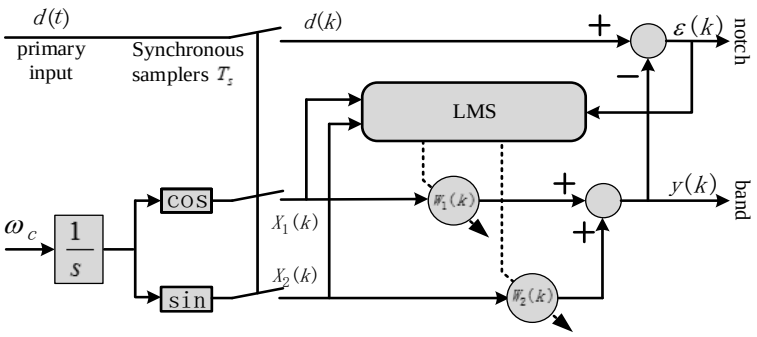

Fig 5-1 Schematic representation of the ADALINE

The network presents two inputs and two outputs: the primary input is the signal to be processed, which is assumed to be of any kind of signal; the reference input is a pure cosine wave ω_c and its π/2vdelay, at the frequency of the primary input signal *d(k)* that should be eliminated or let pass; the two outputs give the notch and the band behaviour respectively.

The sampled reference inputs are,

$$\begin{cases} x_1(k) = C\cos(k\omega_c + \varphi) \\ x_2(k) = C\sin(k\omega_c + \varphi) \end{cases} \tag{5.3}$$

where C is the amplitude of the sinusoidal sequence with reference frequency ω_c.

The procedure for updating the weights is a Least-Squares Algorithm (LS), such as the LMS or the TLS algorithm [92][93]. The LMS is adopted here because of its low complexity, low computational demand, and high-speed of convergence, its learning laws are beneath:

$$\begin{cases} w_1(k+1) = w_1(k) + 2\mu\varepsilon(k)x_1(k) \\ w_2(k+1) = w_2(k) + 2\mu\varepsilon(k)x_2(k) \end{cases} \tag{5.4}$$

where

w_i(k) the weight of the i^{th} neuron at the k^{th} time sample;

μ the learning rate;

$\varepsilon(k)$ the difference between the primary input signal $d(k)$ and the band filter output y(k); ε(k) is also the notch filter output.

It can be proved (see [89](p. 318), for the complete proof) that the notch transfer functions $H(z) = \varepsilon(z)/d\ (z)$ and band $K(z) = y(z)/d\ (z)$ are,

$$K(z) = \frac{2\mu C^2(z\cos(\omega_c) - 1)}{z^2 - 2(1-\mu C^2)z\cos(\omega_c) + 1 - 2\mu C^2} \tag{5.5a}$$

$$H(z) = \frac{z^2 - 2z\cos(\omega_c) + 1}{z^2 - 2(1-\mu C^2)z\cos(\omega_c) + 1 - 2\mu C^2} \tag{5.5b}$$

where $\varepsilon(z)$and $d(z)$ are the z-transform of the sequences ε_k and d_k; the transfer functions are therefore linear functions, and they represents typical second order adaptive filters, like the SOGI-FLL in [94][95]. The notch output and the band output are one complementary to the other.

Moreover it can be further derived by a simple analysis on the poles and zeros of the function, that the quality factor of the filter is explicitly related to the parameters as follows [89]

$$Q = \frac{\text{centerfrequency}}{\text{bandwidth}} = \frac{\omega_c}{2\mu C^2} \tag{5.6}$$

The bandwidth and centre frequency of the filter can be adjusted respectively by the learning rate μ and ω_c, and they completely define the dynamic and the filtering characteristics of the ADALINE filter.

5.1.2 The Retrieval of the RSH by ADALINEs

To retrieve the harmonic current i_h due to the PSH, the following structure is proposed:

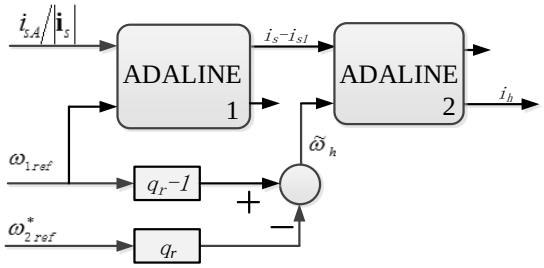

Fig 5-2 ADALINE structure to track the RSH

Fig. 5-2 depicts the overall PSH retrieval system based on two cascaded ADALINEs: one (ADALINE1) works in notch mode, the other (ADALINE2) works in band mode.

ADALINE1 receives as input the normalized stator phase current $i_{sA}(k)/|\mathbf{i}_s|$ given by

$$i_{sA}(k)/|\mathbf{i}_s| = \left[\sum_{\substack{n=1 \\ n\neq h}}^{\infty} I_n \cos(\omega_n k + \varphi_k)\right] + I_h \cos(\omega_h k + \varphi_h) \tag{5.7}$$

Where ω_{1ref} is the supply fundamental angular frequency, I_h, ω_h ,φ_h are respectively the amplitude, angular frequency and initial phase of the RSH, and I_n, ω_n ,φ_n are respectively, the amplitude, angular frequency and initial phase of the harmonics not including the RSH. $\mathbf{i}_s$ is the stator's current space phasors.

The output of ADALINE1 is the current i_s-i_{s1}, that is the normalized stator phase current without the fundamental frequency.

The second ADALINE (ADALINE2) has this last signal as input as well as the estimated slot frequency $\tilde{\omega}_h$. which is computed by using ω_{1ref} and the slip pulsation ω_{2ref} as follows by using (2.2),

$$\tilde{\omega}_h = (q_r - 1)\omega_{1ref} - q_r \omega_{2ref} \tag{5.8}$$

ADALINE2 works in band mode and extracts the slot current i_h

$$i_h(k) = I_h \cos(\omega_h k + \varphi_h) \tag{5.9}$$

where I_h and φ_h are the extracted PSH amplitude and phase.

ω_{1ref} is generally the supply fundamental frequency of the inverter, and its value is given in the framework of both scalar and vector controls.

The structure shown in fig. 5-2 works properly if the RSH is the largest signal once the fundamental frequency has been cancelled. However, $\widetilde{\omega}_h$must be provided quickly and in this thesis the idea is to estimate it on the basis of a simple rotor flux estimator, defined by (2.6).

5.1.3 Design Criteria

The learning rate μ has to be set to obtain a good trade-off between the bandwidth and the convergence speed; which is critical for the network performance, and the overall stability of the system. As a matter of fact, a slow convergence, corresponding to a lower value of μ and a resulting narrower band, introduces a delay that, in a feedback action, could be unacceptable. In addition, filter stability considerations impose the upper limit of μ on the basis of the maximum eigenvalue λ_{max} of the autocorrelation matrix of the input signal, that is: $1/\lambda_{max} > \mu > 0$.

In particular, for the ADALINE in notch mode, the fundamental harmonic is expected to be eliminated. It is assumed that the supply pulsation reference ω_{1ref} is close enough to the true fundamental frequency. Normally a greater μ is preferred, due to the resulting faster convergence and perfect elimination of the fundamental harmonic. This is not true however for low speed values and with heavy load: in these conditions, the PSH frequency is very close to the fundamental, and therefore a smaller μ can guarantee that the PSH be unaffected when the fundamental is cancelled. Fig.5-3 shows the frequency response of the ADALINE notch with respect to μ.

For the ADALINE in band mode, the centre frequency is tuned according to the estimated $\widetilde{\omega}_h$, therefore the bandwidth has to be wide enough to compensate for the error between $\widetilde{\omega}_h$ and the true one, permitting the system to track the PSH properly even in the presence of variations of the value given by (5.8). Moreover they have better phase characteristics around the band frequency. On the other hand, it is important that the harmonic and inter-harmonics outside the PSH be outside the bandwidth of the filter, and this requires a low value of μ. Since in real drive systems the PSH varies quickly according to the working conditions, and since the motor current signature is full of different time-variable harmonics, the constraints for the ADALINE in band mode are of utmost importance. Fig 5-4 shows the frequency response of the ADALINE in band mode with respect to μ.

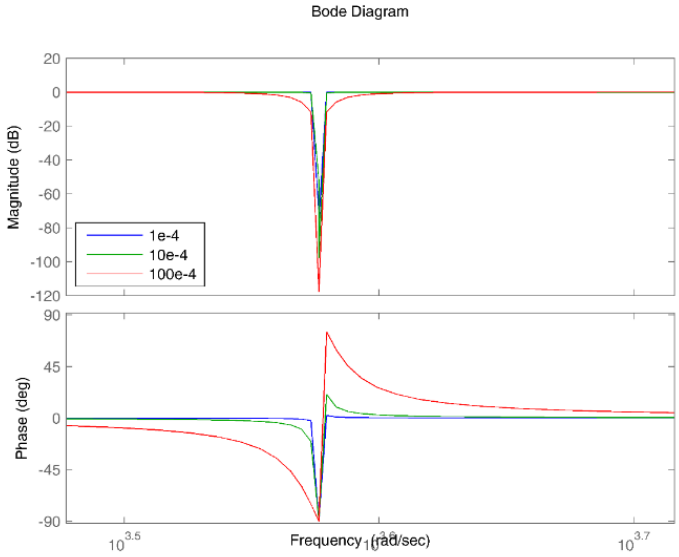

Fig 5-3 Frequency response of the ADALINE notch with respect to μ, centered at 2π*600rad/s.(f_1=50Hz, s=7.14% the experimental motor)

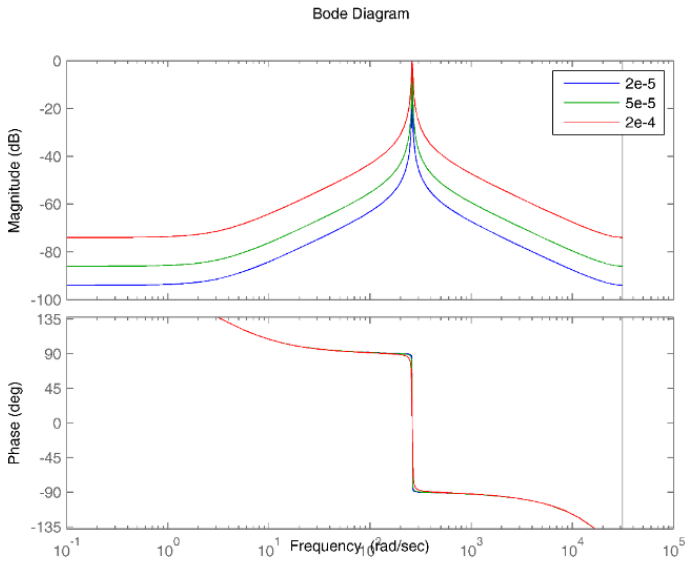

Fig 5-4 Frequency response of the ADALINE band with respect to μ, centered at 2π*600rad/s.(f_1=50Hz, s=7.14% the experimental motor)

The performance of ADALINEs in the PSH retrieve system with respect to different choice of μ has been tested in the experimental platform, with the motor running at 10 rad/s with no-load (ω_h≈260 rad/s). Figs 5-5 show respectively the frequency spectra at the input of ADALINEs (i_{sA}) and output of ADALINEs (i_h), with different μ. They clearly show that

a better filtering effect results with a smaller μ. When μ=2e-4, other harmonics are clearly observed at the ADALINE output, meaning that the filter fails to work correctly for an inappropriate learning rate.

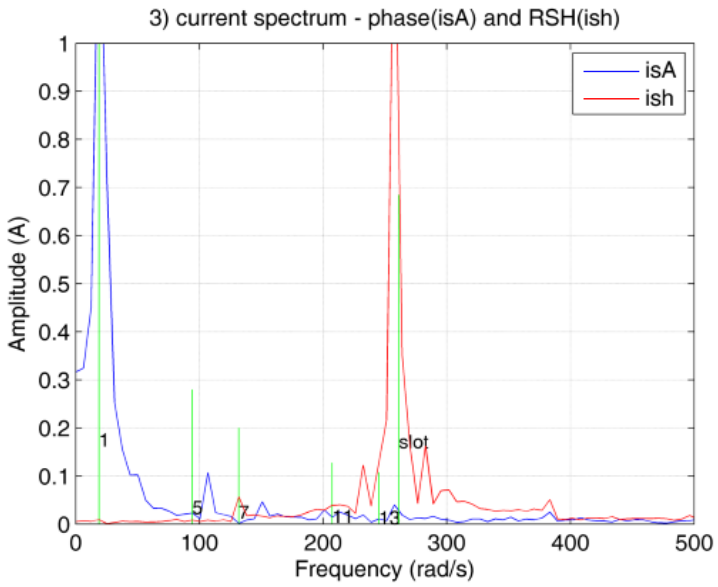

a) μ =2e-5

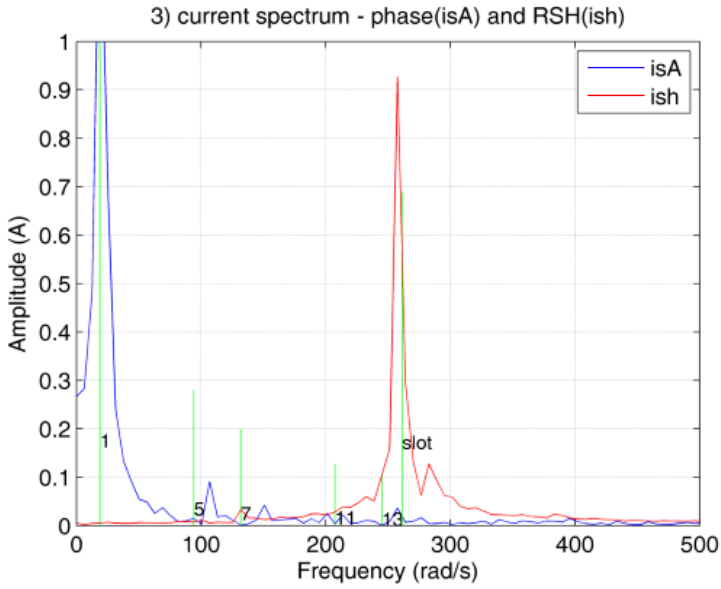

b) μ =5e-5

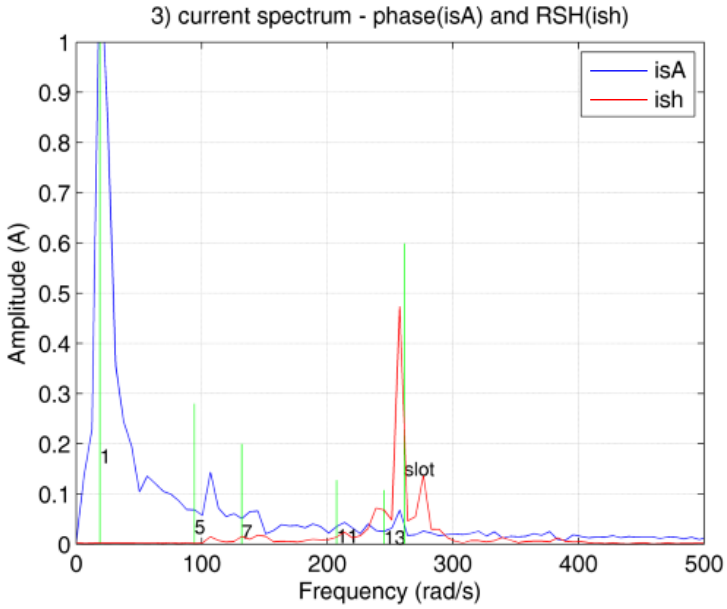

c) μ =2e-4

Fig 5-5 The FFT results of current at the input of ADALINEs (i_{sA}) and output of ADALINEs(i_h)

5.2 Frequency Estimation Based on MCA EXIN Pisarenko Method

5.2.1 The Pisarenko's Theory

The noisy discrete-time measurements of the filtered slot harmonic can be represented as

$$x(k) = i_h(k) + q(k) = I_h \cos\left(\omega_h k + \varphi_h\right) + q(k) \tag{5.10}$$

where ω_h is the slot harmonics pulsation, and φ is a random variable uniformly distributed in [0, 2π). The noise q(k) is assumed to be a zero-mean white process with unknown variance σ^2.The task is to find ω_h from K samples of $x(k)$ [96-101].

One way to estimate frequency is using subspace methods, such as Pisarenko and MUSIC, which assume that the signal is a sum of harmonics and explore the orthogonality between the noise subspace and the signal subspace [102-107]. The frequency can be then computed simply by making an eigenvalue decomposition of the autocorrelation matrix of the input signal.

Among them, Pisarenko is probably the most simple and computational efficient. In the Pisarenko method [102], it is assumed that the data sequence is a sum of p complex exponentials in white noise,

$$x(k) = \sum_{i=1}^{p} \mathbf{A}_i e^{j\omega_i n} + \upsilon(n) \tag{5.11}$$

Where v(n) is a zero mean white noise with variance σ^2, and $\mathbf{A}_i$, ω_i are respectively the amplitude and the angular frequencies of the i^{th} exponential. The amplitudes $\mathbf{A}_i$ are complex numbers as follows:

$$\mathbf{A}_i = |A_i| e^{j\varphi_i} \tag{5.12}$$

and the phases φ_i are considered uncorrelated random variables uniformly distributed over the interval [0, 2π).

In the Pisarenko's theory, the data sequence is considered to be a final length sequence of p+1 elements, therefore a (p+1)×(p+1)autocorrelation matrix can be constructed as follows (see Appendix B for details):

$$\mathbf{R}_{xx} = E(\mathbf{x}\mathbf{x}^T) = \begin{bmatrix} r_{xx}(0) & r_{xx}(1) & \cdots & r_{xx}(p) \\ r_{xx}(1) & r_{xx}(0) & \cdots & r_{xx}(p-1) \\ \vdots & \vdots & \ddots & \vdots \\ r_{xx}(p) & r_{xx}(p-1) & \cdots & r_{xx}(0) \end{bmatrix} \tag{5.13}$$

where $r_{xx}(k)$ is the k^{th} input autocorrelation sequence $\mathbf{R}_{xx}$ can be decomposed into

$$\mathbf{R}_{xx} = \mathbf{R}_{ss} + \sigma^2 \mathbf{I} \tag{5.14}$$

where $\mathbf{R}_{ss}$ is the autocorrelation matrix without noise.

The autocorrelation matrix $\mathbf{R}_{ss}$ is of rank p[102], but $\mathbf{R}_{xx}$ is of rank p+1 due to the presence of white noise, with eigenvalues $\sigma^2 \leq \lambda_p \leq \ldots \leq \lambda_1$ and corresponding orthonormal eigenvectors $\mathbf{z}_{p+1}$, $\mathbf{z}_p, \ldots, \mathbf{z}_1$. In this choice, the dimension of noise subspace is equal to one, and it is spanned by the eigenvector corresponding to the minimum eigenvalue, $\lambda_{min} = \sigma^2$. Denoting this noise eigenvector by $\mathbf{v}_{min}$, it follows from (5.14) that

$$\mathbf{R}_{ss}\mathbf{v}_{\min} = 0 \tag{5.15}$$

And $\mathbf{v}_{min}$ is therefore orthogonal to each of the signal vectors, $\mathbf{e}_i = \begin{bmatrix} 1 & e^{j\omega_i} & e^{j2\omega_i} & \cdots & e^{jp\omega_i} \end{bmatrix}^T$ [102]. Thus, the frequency can be estimated by finding all the roots of the following polynomial equation formed by the minimum eigenvector,

$$V_{\min}(e^{j\omega}) = \sum_{k=0}^{p} \mathbf{v}_{\min}(k) e^{-jk\omega} = 0 \tag{5.16}$$

Consequently, the z-transform of the noise eigenvector, $\mathbf{v}_{\min}$, has p zeros on the unit circle,

$$V_{\min}(z) = \sum_{k=0}^{p} \mathbf{v}_{\min}(k) z^{-k} = \prod_{k=0}^{p} (1 - e^{j\omega_k} z^{-1}) \tag{5.17}$$

corresponding to the p harmonics of the signal: the frequencies of the complex exponentials can be therefore extracted from the roots of $V_{min}(z)$.

When the original Pisarenko's method is used to estimate the frequency, it is limited by: 1) The estimation of the autocorrelation sequence: in real-time applications, the amount of data samples that one has to work with is never unlimited, actually most are computed on a limited number of samples, and this will lead up to an erroneous estimation. 2) The general difficulties involved in determining the eigenvalues and eigenvectors of autocorrelation matrix: the algorithm of SVD require $\boldsymbol{O}(N^3)$ multiplications, for high-order problems, resulting in a lot of computation effort.

To adaptively compute the generated eigenvector associated with the smallest eigenvalue of an autocorrelation matrix. A number of algorithms have been proposed in the framework of Pisarenko theory. These algorithms can mainly be divided into two categories: The first category involves stochastic-type adaptive algorithms. Thompson [108] first proposed an adaptive algorithm that is used to extract a single minor component and can be applied to find the Pisarenko solutions. Other similar algorithms have also been reported in [109],[110], they usually require $O(N)$ computational complexity. The second category algorithms are called the recursive total least squares (RTLS) algorithms. They are developed on the basis of recursive least square (RLS) method, in the RTLS algorithm however, the observation vector is also assumed to be corrupted by noise. In general, the RTLS algorithms have $O(N^2)$ computational complexity per iteration, whereas the fluctuations in the estimation parameter are reduced. Examples can be found in [126][127], they can quickly track the eigenvector associated with the smallest eigenvalue of the augmented correlation matrix.

Obviously the algorithms in the first category are more appropriate to implement on-line due to the reduced computation. However, the inherent limitation of the learning process necessitates a compromise between the requirement of fast convergence rate and small mean square frequency estimation error (MSFE) (the MSFE are of order $O(\alpha)$, being α the learning rate [118](p.251)). One interesting approach for the stochastic-type adaptive algorithms is, to adaptively select the values of the learning rate in accordance with some criterion, which can provide an approximate measure of the adaptation process state. Such an algorithm is, even imperative when one tries to apply it in the real-time case. Many heuristic methods has been directed to vary the step size for the gradient based algorithm such as LMS, RLS, and back propagation [111],[112], they can all work effectively in their own field, but are not directly applicable to the MCA neurons.

In the following the recursive frequency estimation algorithms using the original MCA EXIN and two improved MCA EXIN method under the framework of Pisarenko will be discussed. The MCA EXIN neuron, which deals with the recovery of eigenvectors of the data sequence's autocorrelation matrix, as proposed in [92][113][114], can be adopted for finding the minimum eigenvalue and eigenvector to be used in Pisarenko method. Thus, the estimation algorithm can become iterative and deal with each data sample instead of the whole data block, meanwhile, the overall solution is of TLS meaning (see appendix D).

5.2.2 The MCA EXIN Pisarenko method

A recursive total least squares neural network (MCA EXIN) can be used to compute the TLS solution of the minimum eigenvector required by Pisarenko's method; the algorithm requires only $\boldsymbol{O}(N)$ multiplication at each iteration. Fig. 5-6 shows the scheme of the neural networks.

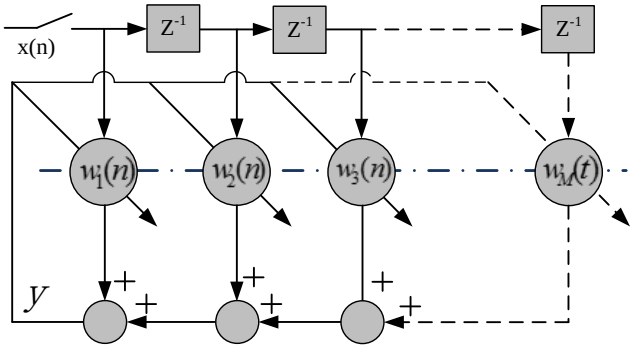

Fig 5-6 The recursive linear total least square neural network

In the following a brief summary of the MCA EXIN neuron is given as in [113].

Let a linear neuron be considered with a real input vector $\mathbf{x}(t) = [x_1(t), \ldots, x_M(t)]^T$ and real output y(t) (see appendix C for details):

$$y(t) = \mathbf{w}^T(t)\mathbf{x}(t) = \sum_{i=1}^{M} w_i(t)x_i(t) \tag{5.18}$$

where $\mathbf{w}(t) = [w_1(t), \ldots, w_M(t)]^T$ is the weight vector.

In order that the neural weights converge to the minimum eigenvector, the updates of weights should follow the minimization of the Rayleigh quotient (RQ),

$$E[J] = r[\mathbf{w}, \mathbf{R}_{xx}] = \frac{\mathbf{w}^T\mathbf{R}_{xx}\mathbf{w}}{\mathbf{w}^T\mathbf{w}} \tag{5.19}$$

By employing a gradient descent method for minimizing this function, the gradient flow of E[J] is given by

$$\frac{d\mathbf{w}(t)}{dt} = -\frac{1}{\|\mathbf{w}(t)\|_2^2}\left[\mathbf{R}_{xx} - \frac{\mathbf{w}^T(t)\mathbf{R}_{xx}\mathbf{w}(t)}{\mathbf{w}^T(t)\mathbf{w}(t)}\right]\mathbf{w}(t) \tag{5.20}$$

with $\|\bullet\|_2$ the Euclidean norm of a vector. This equation is the average version of the continuous time differential equation,

$$\frac{d\mathbf{w}(t)}{dt} = -\frac{1}{\|\mathbf{w}(t)\|_2^2}\left[\mathbf{x}(t)\mathbf{x}^T(t) - \frac{\mathbf{w}^T(t)\mathbf{x}(t)\mathbf{x}^T(t)\mathbf{w}(t)}{\mathbf{w}^T(t)\mathbf{w}(t)}\right]\mathbf{w}(t) \tag{5.21}$$

The EXIN neuron, one of the best learning laws in terms of stability and converging time, whose averaging gradient flow (ODE) is directly derived from the discretization of the sequential version of the exact gradient flow of *RQ*, is given by

$$\mathbf{w}(t+1) = \mathbf{w}(t) - \frac{\alpha(t)y(t)}{\|\mathbf{w}(t)\|_2^2}\left[\mathbf{x}(t) - \frac{y(t)\mathbf{w}(t)}{\mathbf{w}^T(t)\mathbf{w}(t)}\right] \tag{5.22}$$

where $\alpha(t)$ is the learning rate.

Let $\mathbf{R}_{xx}$ be the n×n autocorrelation matrix of input data. If $\mathbf{w}(0)$ satisfies $\mathbf{w}^T(0)\mathbf{z}_M \neq 0$ (being $\mathbf{z}_M$ the orthonormal eigenvector corresponds to the smallest eigenvalue), it holds

$$\mathbf{w}(t) \to \pm\|\mathbf{w}(0)\|_2 \mathbf{z}_M \tag{5.23}$$

Then this weight vector, which converges to the eigenvector corresponds to the smallest eigenvalue (MC), can be used in (5.17) for computing the frequencies.

It should be noted that in (5.11) the signal is assumed to have *p* complex-valued exponential: the required dimension of autocorrelation matrix and number of MCA neurons are *M*=*p*+1. It is obvious that for *p* real-valued sinusoidal ($\cos(\omega t) = (e^{j\omega t} + e^{-j\omega t})/2$); thus the required dimensions is *M=2p+1* correspondingly. For the real-valued data stream from the ADALINEs (5.10) *M*=2*p*+1=3 neurons are required, so it is considered that the output of the ADALINE is only one harmonic, i.e. the PSH.

5.2.3 The rMCA EXIN Pisarenko method

If the signal to be processed is real-valued, the symmetry property can be used to accelerate the convergence. Consider a stream of signals $x \in \mathbb{R}^{2p+1}$ where 2*p* is the number of harmonics in the signal (*p* complex frequencies*)*. Define $\mathbf{R}_{xx} = E(xx^T)$ as the associated covariance matrix.

Define:

$$Q_1 = \begin{pmatrix} I_p/\sqrt{2} & 0 \\ 0 & 1 \\ J_p/\sqrt{2} & 0 \end{pmatrix} \tag{5.24}$$

which is $(2p+1) \times (p+1)$, where I_p is the $p \times p$ identity matrix and J_p is the $p \times p$ anti-diagonal matrix:

$$I_p = \begin{pmatrix} 1 & \cdots & 0 \\ \vdots & \ddots & \vdots \\ 0 & \cdots & 1 \end{pmatrix}, \; J_p = \begin{pmatrix} 0 & \cdots & 1 \\ \vdots & \iddots & \vdots \\ 1 & \cdots & 0 \end{pmatrix} \tag{5.25}$$

Consider the "projected stream" of vectors $\boldsymbol{y} = Q_1^T \boldsymbol{x}$, which results as :

$$\left(\frac{x_1 + x_{2p+1}}{\sqrt{2}}, \frac{x_2 + x_{2p}}{\sqrt{2}}, \cdots, x_{p+1} \right)^T \tag{5.26}$$

with $p+1$ components (reduced space).

Find the eigenvector γ_1 associated to the smallest eigenvalue for the projected stream y.

The true eigenvector is given by

$$\mathbf{c} = Q_1 \boldsymbol{\gamma}_1 \tag{5.27}$$

Then the eigenvector for the Pisarenko's method is given by the corresponding unit vector. This MCA EXIN with reduced space is named rMCA EXIN. With regard to MCA EXIN, the convergence is accelerated and the computational complexity is reduced by *p*.

For the signal given in (5.10), it is considered that only one slot harmonic is present; hence, *M=p+1=2* neurons are required.

5.2.4 The Adaptive MCA EXIN Pisarenko method

The learning rate of the MCA EXIN is normally assumed to be constant or exponentially decreasing to zero [115-118]. However, a data-driven adaptive learning rate can be used in the conventional gradient MCA algorithm. This new algorithm, gives faster tracking and smaller mean square error.

Recall the learning process,

$$\mathbf{w}(t+1) = \mathbf{w}(t) - \alpha(t)\nabla\big(\mathbf{w}(t)\big) \tag{5.28}$$

where $\nabla\big(\mathbf{w}(t)\big)$ is the gradient flow and has been given in (5.20). Consider the averaged continuous equation and expand it around the critical directions, $\{\mathbf{z}_1, \mathbf{z}_2, \ldots, \mathbf{z}_M\}$. The averaged gradient flow vanishes at these critical directions, i.e. at $\boldsymbol{w}_i^*$ such that $\overline{\nabla}(\boldsymbol{w}_i^*) = 0$. It follows

$$\frac{d\mathbf{w}(t)}{dt} = -\alpha(t)\overline{\nabla}\big(\mathbf{w}(t)\big) \cong -\alpha(t)\boldsymbol{H}_i^*[\mathbf{w}(t) - \boldsymbol{w}_i^*] \tag{5.29}$$

where $\boldsymbol{w}_i^*$, $\boldsymbol{H}_i^*$ (*i=1,…M*) are, respectively, the weight vector and the Hessian matrix at the critical direction *i*, i.e., *i=M*, which corresponds to the optimal solution (MC)**.**

Suppose an eigenvector $\boldsymbol{v}$ of the matrix$\boldsymbol{H}_i^*$, satisfying

$$\boldsymbol{v}^T\boldsymbol{H}_i^* = \lambda\boldsymbol{v}^T \tag{5.30}$$

and define [119][120]

$$\xi(\mathrm{t}) = \boldsymbol{v}^T\overline{\nabla}\big(\mathbf{w}(t)\big) \cong \boldsymbol{v}^T\boldsymbol{H}_i^*[\mathbf{w}(t) - \mathbf{w}_i^*] \tag{5.31}$$

where the average gradient flow $\overline{\nabla}$ is projected into a unique direction $\boldsymbol{v}$. The idea is to choose a good direction $\boldsymbol{v}$ such that it is sufficient to observe the whole dynamics of the flow only along this projection, whereas any computation of the Hessian matrix itself can be avoided.

Hence the dynamics of $\xi(\mathrm{t})$ can be approximately represented as

$$\frac{d}{dt}\,\xi(\mathrm{t}) = -\lambda\alpha(t)\xi(\mathrm{t}) \tag{5.32}$$

By using $\xi(\mathrm{t})$, the discrete and continuous modification of the rule for $\alpha(t)$ is given by [119]

$$\alpha(t) = \alpha(t) + l\alpha(t)[m|\,\xi(\mathrm{t})| - \alpha(t)] \tag{5.33}$$

$$\frac{d}{dt}\,\alpha(t) = l\alpha(t)[m|\,\xi(\mathrm{t})| - \alpha(t)] \tag{5.34}$$

where l, m are constants. The asymptotic solutions of equation (5.32) and (5.34) are given by

$$\xi(\mathrm{t}) = \frac{1}{m}\left(\frac{1}{\lambda} - \frac{1}{l}\right)\frac{1}{t}, \alpha(t) = \frac{1}{\lambda}\frac{1}{t} \tag{5.35}$$

This 1/t-convergence rate is the optimal order of any estimator $\mathbf{w}(t)$ converging to $\mathbf{w}^*$.

An important problem concerns the choice of a good direction $\boldsymbol{v}$ of projection. It should be noted that any direction can be valid except the one which is orthogonal to the gradient flow. Here it is assumed that all the critical directions are sufficiently different from each other. It exists a learning rate such that, at the critical direction, the learning becomes

$$\mathbf{w}_i^* - \mathbf{w}(t) = -\alpha(t)\overline{\nabla}\big(\mathbf{w}(t)\big) \tag{5.36}$$

Together with (5.31), it follows

$$\frac{1}{\alpha(t)}\overline{\nabla}\big(\mathbf{w}(t)\big) = \boldsymbol{H}_i^*\overline{\nabla}\big(\mathbf{w}(t)\big) \tag{5.37}$$

From (5.37), it follows that by properly choosing the learning rate, the average instantaneous gradient flow can be forced to be one of the eigenvector of $\boldsymbol{H}_i^*$, with the corresponding eigenvalue inversely proportional to the learning rate. Hence the projection direction can be approximated by

$$\boldsymbol{v} = \frac{\bar{\nabla}(\mathbf{w}(t))}{\|\bar{\nabla}(\mathbf{w}(t))\|} \tag{5.38}$$

and it can be adopted :

$$\xi(\mathrm{t}) = \boldsymbol{v}^{\boldsymbol{T}}\bar{\nabla}\big(\mathbf{w}(t)\big) = \big\|\bar{\nabla}\big(\mathbf{w}(t)\big)\big\| \tag{5.39}$$

(5.38) and (5.39) represent the most possible efficient projection direction. Eq. (5.33) can be computed by only using the knowledge of instantaneous flow. The learning process converges to the critical direction with 1/*t* optimal rate. The critical direction is unstable toward the directions associated to smaller eigenvalues [113], because the considered equilibrium direction is a local maximum (in RQ) for the directions with smaller eigenvalues: the fact that the algorithm is a gradient descent implies that the equilibrium has to be unstable in this direction. Hence, the weights converge to the critical direction corresponding to the minimum eigenvalue.

From [113], the eigenvalues of the Hessian matrix are given by

$$\boldsymbol{H}_i^* \boldsymbol{z}_j = \begin{cases} 0 & i = j \\ (\lambda_j - \lambda_i)\boldsymbol{z}_j & i \neq j \end{cases} \tag{5.40}$$

Hence, it has the same eigenvectors as $\mathbf{R_{xx}}$, but with different eigenvalues. Compared to the Hessian matrix at the minimum, the Hessian matrix at the other critical directions has smaller spectra, and the one corresponding to the largest eigenvalues has the smallest spectrum. As λ in the asymptotic solution (5.35) is one of the eigenvalues of $\boldsymbol{H}_i^*$, the term $\frac{1}{\lambda}$ in (5.35) decreases as the neural networks converge towards the eigenvector corresponding to the minimum eigenvalue of $\mathbf{R_{xx}}$. When the weight vector is in the same direction of the eigenvector corresponding to the minimum eigenvalue (MC), $\frac{1}{\lambda}$ will be the smallest possible one, and the learning rate $\alpha(t)$ decreases continuously along the $\frac{1}{\lambda}\frac{1}{t}$ curve as shown in (5.35)**.**

Moreover, the critical directions corresponding to different eigenvalues represent different learning stages of the neural networks, i.e. the weight vector is still far from the MC if it is in the directions corresponding to the largest eigenvalues, and it is the final solution if it is in the same direction of MC, which corresponds to the smallest eigenvalue. They should be treated differently by the adaptive mechanism. The averaged instantaneous cost function

$$\bar{J} =< \frac{\mathbf{w}^T(t)\mathbf{x}(t)\mathbf{x}^T(t)\mathbf{w}(t)}{\mathbf{w}^T(t)\mathbf{w}(t)} > \tag{5.41}$$

can be adopted, since from the property of RQ, at the critical direction it holds that the eigenvalues of input correlation matrix$\lambda_i \approx \bar{J}$. When $\bar{J}$ is large, it means the neurons are still far from the final solution, and are possibly approaching towards the critical direction associated to a larger eigenvalue. Therefore, the new adapting rule is given by considering the RQ as,

$$\alpha(t+1) = \alpha(t) + n\bar{J}\alpha(t)[m|\,\xi(\mathrm{t})| - \alpha(t)] \tag{5.42}$$

where *l* in (5.33) is replaced by $n\bar{J}$, being *n* a constant which scales the product to a reasonable range.

If the term $n\bar{J}$ varies much slower than the learning rate itself, i.e. (5.41) is averaged over a large number of iterations, then it still holds the solution in (5.35), and *l* in the solution is replaced by $n\bar{J}$. Thus, the term $\left(\frac{1}{\lambda} - \frac{1}{n\bar{J}}\right)$ in (5.35) is larger at the beginning, and it decreases as $\bar{J}$ converges. The global convergence becomes faster.

An upper bound of learning rate can be used to enhance the convergence of the adaptive MCA EXIN algorithm under all conditions, the derivation of this bound in detail has been included in appendix E for the simplicity's sake.

5.2.5 Numerical Simulation of the MCA EXIN and rMCA EXIN

5.2.5.1 Methods to be compared

A. PLL

The phase locked loop (PLL) is chosen as one of the methods to be compared [121]. The structure of the main PLL topology can be found in chapter 4 (see fig.4-2 inside the dashed box).

B. Cross correlation based method

The cross correlation matrix based method (COR) proposed in [122] is chosen as another method to be compared. In [122], the cross-correlation matrix is used to replace the auto-correlation matrix used in the Pisarenko type method, where the estimation of autocorrela-

tion sequence is usually biased for short data samples. The recursive version of COR algorithm (recCOR), which avoids matrix inversion, is also described in the paper, and it can be used to track time-variant frequencies.

The only parameter to be adjusted in the recCOR is a forgetting coefficient ρ. For there is not much discussion about the choice of ρ in the original paper, in this simulation, ρ =0.9 is used by which a best simulation performance, in terms of rapidity and variance, can be achieved.

5.2.5.2 Some Definitions

A. SNR

The signal to noise ratio is given by [123],

$$SNR = 20\log\left(\frac{A}{\sqrt{2}\sigma}\right) \tag{5.43}$$

where A is the amplitude of the signal, σ is the standard deviation of the noise.

B. The mean-square frequency estimation error

The mean-square frequency estimation error (MSFE), which is used to evaluate the frequency estimation error, is given as below [124],

$$MSFE = 10\log\frac{\sum_{i=1}^{N}(\omega_e - \omega_e^*)^2}{N} \tag{5.44}$$

Where ω_e is the estimated frequency, ω_e^* is the value of the true frequency, N is the number of iterations over which the algorithm has been evaluated.

C. CRLB

The CRLB, which is the lowest MSFE that can be achieved by any unbiased estimator is given in [103][125]

$$CRB = \frac{6\sigma^2}{A^2(N-2)[(N-2)^2-1]} \tag{5.45}$$

5.2.5.3 Simulation Results

The performances of the MCA EXIN Pisarenko's method have been evaluated using Matlab/Simulink, the objective of the simulation study is to investigate the realization of the MCA EXIN Pisarenko method and highlight the characteristics of the MCA EXIN Pisarenko method. It has been applied to estimate the frequency in various conditions: as the proposed method is aimed to estimate the frequency of the rotor slot harmonics (RSH) in an induction machine, which varies in a very wide range (from a few hertz to hundreds of hertz), and rapidly (it is dependent of the target system, normally within a few milliseconds). The simulation conditions are designed based on the characteristics of RSH, The sampling frequency is 2 kHz, the typical value for the learning rate is in the range 0.001~0.05. The initial weight modulus are 0.5~0.8.

Comparisons are made among the proposed MCA EXIN and rMCA EXIN algorithms with learning rate α=1e-3, the PLL, the correlation method (COR), the recursive type correlation method (recCOR) (ρ =0.9), and the original Pisarenko's harmonic decomposition method (PSH). The estimator is aimed to have a good performance for the extraction of RSH, whose frequency possibly lies in a wide range, so the MSFE has to be tested in full range. Meanwhile the RSH frequency could be quite low compared to the sampling frequency, it is necessary to specify the performance at low frequency.

A. Comparason of MCA EXIN and rMCA EXIN

In this part, the converging speed of MCA EXIN and rMCA EXIN are compared: the MCA EXIN and rMCA EXIN start from the same initial condition, and end when the same stop criterion is met, the stop criterion is that the error of instantaneous RQ $|\lambda(t+1)- \lambda(t)|$<threshold for 30 consecutive iterations. The MCA EXIN and rMCA EXIN have been applied to single, two real-valued, and three real-valued frequencies cases respectively, under noise level SNR=10dB, 20dB, 30dB and 40dB.

The results are summarized in Tabs. 5-1 to 5-3, they illustrate respectively the results for single, two real-valued, and three real-valued frequencies estimation results. Among them, the number of iterations, elapsed time, and stop $rho^{(2)}$ show the dynamic of neuron,

while the mean value, variance, and MSFE, which are computed over 100 iterations, suggest the steady-state performance of the neuron.

From Tab 5-1 to Tab 5-3, they show that the rMCA EXIN converges faster than MCA EXIN in all the cases, with less time and computation burden. Although the MSFE of MCA EXIN is a littler larger than rMCA EXIN, it is acceptable for the significant improvement in the speed of convergence.

Tab 5-1 Single sinusoid, A^2= 2.963, ω=0.159π

SNR (dB)	10		20		30		40	
	MCA EXIN	rMCA EXIN	MCA EXIN	rMCA EXIN	MCA EXIN	rMCA EXIN	MCA EXIN	rMCA EXIN
Elapsed(1) time(μs)	X[2]	X	645	388	513	360	509	303
Stop rho(3) (dB)	X	X	-56,08	60,08	51,40	62,51	50,63	51,26
Number iterations	X	X	195	119	155	111	154	93
Mean frequency	0,4986	0,4983	0,4995	0,4994	0,4995	0,4995	0,4995	0,4995
MSFE (dB),	36,28	34,26	47,40	44,08	57,52	53,95	67,50	63,91

Tab 5-2 Two sinusoids A_1^2=2, A_2^2=3, ω_1 =0.5 π, ω_2=0.8 π

SNR (dB)	10		20		30		40	
	MCA EXIN	rMCA EXIN	MCA EXIN	rMCA EXIN	MCA EXIN	rMCA EXIN	MCA EXIN	rMCA EXIN
Elapsed(1) time(μs)	X	X	1393	828	1159	619	1074	551
Stop rho (dB)	X	X	-47,03	-62,76	-43,19	-40,34	-39,32	-35,31
Number iterations	X	X	416	252	348	188	314	168
Mean value	1,57	1,57	1,57	1,57	1,57	1,57	1,57	1,57
	2,5135	2,5134	2,5133	2,5133	2,5133	2,5133	2,5133	2,5133
MSFE(dB)	-44,32	-40,92	-54,33	-49,80	-64,26	-59,49	-74,18	-69,41
	-44,58	-41,16	-53,21	-48,56	-63,00	-58,15	-72,90	-68,13

Tab 5-3 Three sinusoids A_1^2=2, A_2^2=3, A_3^2=4, ω_1 =0.5 π, ω_2 =0.8 π, ω_3 =0.7 π

SNR (dB)	10		20		30		40	
	MCA EXIN	rMCA EXIN	MCA EXIN	rMCA EXIN	MCA EXIN	rMCA EXIN	MCA EXIN	rMCA EXIN
Elapsed[1] time(μs)	X	X	1738	1454	1603	852	1261	750
Stop rho(dB)	X	X	-31,21	-41,46	-29,63	-26,32	-23,51	-23,47
Number iterations	X	X	518	443	478	258	373	225
Mean frequency	1,57	1,57	1,57	1,57	1,57	1,57	1,57	1,57
	2,20	2,21	2,20	2,20	2,20	2,20	2,20	2,20
	2,5214	2,5093	2,5157	2,5084	2,5134	2,5127	2,5131	2,5133
MSFE(dB)	-36,77	-32,70	-45,60	-40,22	-54,96	-49,34	-64,40	-59,09
	-24,88	-20,16	-30,71	-24,73	-39,52	-33,66	-49,25	-43,91
	-27,38	-23,24	-33,43	-27,26	-42,25	-36,25	-52,05	-46,68

1. The test platform for elapsed time is: intel core i5-3320M, 2.6Ghz, matlab 7.9.0
2. X means the stop criterion is not met even in steady-state
3. $rho = 10\log\frac{\sum_{i=1}^{M}(w_i - w_i^*)}{N}$ is used as an indicator for estimation accuracy. M is the dimension of neurons, w_i are the components of the neuron weight vector and w_i^* are the components of the true value, the neuron weights are normalized according to the minimum eigenvector for comparison.

B. MSFE versus estimated frequency(normalized)

Fig. 5-7a shows the MSFE results versus frequency at SNR=20dB, which is computed by (5.44) over 100 iterations.

As shown in the figure, the MSFE of MCA and rMCA EXIN have the smallest MSFE in the whole range, and their performance are comparable to CRLB. It should be noted that their performance is acceptable even at very low frequency, i.e. ω approaches 0 and π, this verifies that they are suitable for frequency estimation over a wide range. The original COR

outperforms the original Pisarenko's method (PSH) in the medium frequency range, however, it degrades dramatically as the frequency approaching 0 and π. The same phenomenon can be observed in its recursive version, but with a much higher MSFE, especially at low frequency. Compared to the other algorithms, the results of PLL is more flat, making its performance at low frequency notable.

The mean frequency estimation error is illustrated in fig.5-7 b. It is found that the biases of all the algorithm are small except when frequency is close to 0 or π. Among them, the COR and recCOR have the largest bias, MCA and rMCA EXIN have the smallest bias for most of the frequencies, the exceptions happen if ω is close to 0 or π, where the PLL has the lowest error.

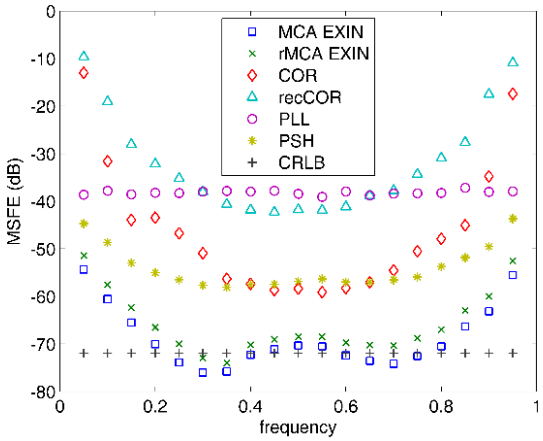

a) MSFE

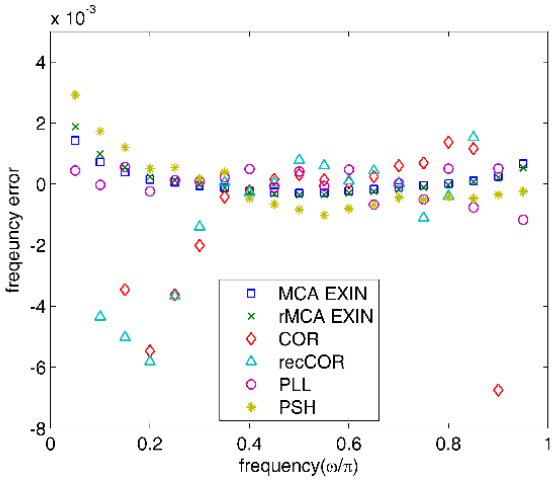

b) Mean frequency estimation error

Fig 5-7 Frequency estimation performance of the algorithms under consideration at different frequencies, with A= $\sqrt{2}$, SNR=20dB and N=100

C. MSFE versus SNR

Fig.5-8a illustrates the MSFE results versus SNR level, the signal frequency ω=0.1 π, fig.5-8 b) shows the corresponding mean frequency estimation error.

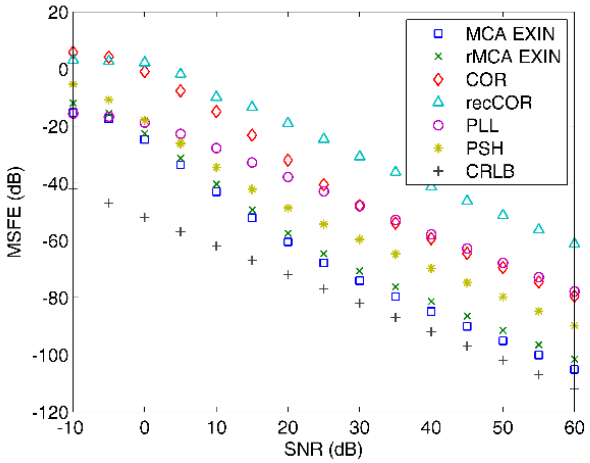

a) MSFE

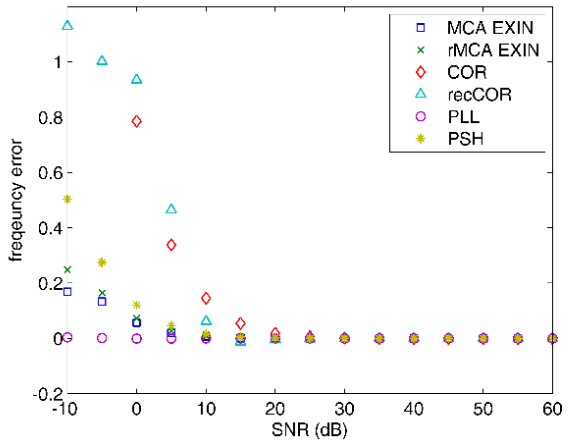

b) Mean frequency estimation error

Fig 5-8 Frequency estimation performance of the algorithms under consideration versus SNR, A=$\sqrt{2}$, ω=0.1 π and N=100

As shown in the figure, the best MSFE can be obtained by using the MCA and rMCA EXIN: if SNR is not so small, their results are comparable to CRLB. The performance of COR diverges according to the noise levels, and it has an acceptable result only at high SNR. This can be explained by the fact that, compared to the autocorrelation, the cross-relation matrix framework has larger forgetting factor, thus it has a low bias but larger variance. Meanwhile, the recCOR has even larger MSFE in most of the cases. What is more,

like in fig. 5-7, although PLL is outperformed by other methods at high SNR, it has a good performance at very low SNR, the closed-loop framework makes the PLL has a more flat MSFE in respect to noise level and frequencies.

D. Tracking of Step Change.

The tracking features of the MCA EXIN method, rMCA EXIN method, PLL and recCOR with respect to step change is investigated in this part in the conditions 1) the frequency steps down from 50Hz to 49.5Hz at 0.1s, then steps up to 50Hz at 0.35s. SNR=60dB. 2) The frequency steps down from 200 Hz to 100Hz and steps up, SNR=40dB

Fig.5-9 shows the result for condition 1). At steady-state, the estimated frequencies for all methods are accurate. The MCA EXIN tracks the new frequency within 0.01s, no oscillation is observed as it approaches the actual frequency, and the rMCA EXIN converges even faster, although the oscillations is larger than MCA EXIN. The PLL response rapidly, but it has an overshoot and bias which die out slowly. That results from the linear nature of PLL, whereby it will either have a fast response with large ripples at steady-state, or a slow response with small ripples; it is difficult to find a proper bandwidth which satisfies both requirements. MCA EXIN and rMCA EXIN algorithm however follow the direction of gradient descent, once they arrives at the minimum component, a large 'inertia' will prevent it from overshoot. The recCOR has a good steady-state performance, but the transient is not good enough, although the dynamic could be accelerated by using a smaller forgetting factor, the oscillation increases in the same way.

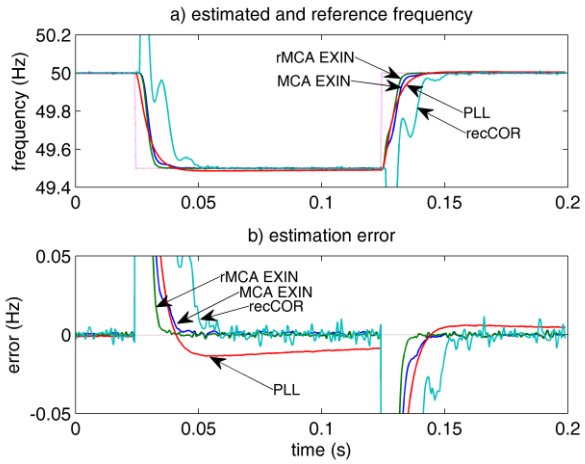

Fig 5-9 Tracking capability of the MCA EXIN method with respect to step change in frequency of the input signal (small step).

The results of step change in condition 2) are shown in fig.5-10. They have the similar response pattern as fig.5-9, but the oscillation and estimation errors increase for all the methods, this is as a consequence of the change in SNR. However, the rMCA EXIN and MCA EXIN still have the fastest response and smallest oscillation.

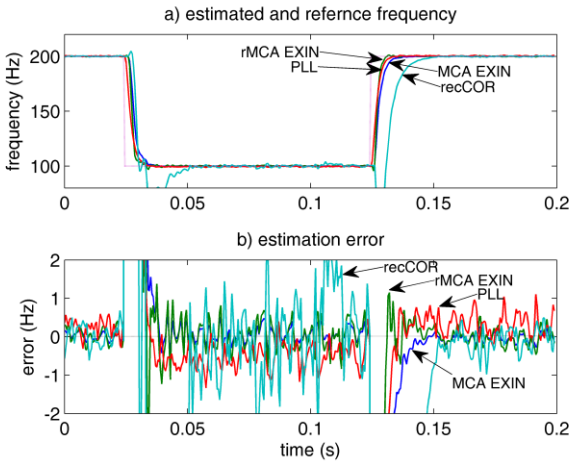

Fig 5-10 Tracking capability of the MCA EXIN method with respect to step change in frequency of the input signal (big step)

E. The estimation of two sinusoidal simultaneously

The capability to track two real valued sinusoidal signals at the same time is investigated in this part. The harmonics signal is given by $x(t) = \sin(2\pi \times 50t) + 0.5\sin(2\pi \times 250t)$. A 5% step in frequency occurs at t=0.1s to one harmonic. Since the PLL cannot estimate two frequencies at the same time, the simulation is done only with the MCA EXIN, rMCA EXIN and recCOR method.

Fig. 5-11 shows that the MCA EXIN and rMCA EXIN method track the change properly within 0.02s, but the whole recovery process takes 0.1s for MCA EXIN and 0.05s for rMCA EXIN. The recCOR tracks the reference in about 0.16s, and the transient of the recCOR method is not as smooth as the EXIN method. For this case, the MCA EXIN has a dimension of 5 ($2p$+1) instead of 3 in the single frequency case, and the rMCA EXIN has a dimension of 3(p+1). The improvement on the speed of converging of rMCA EXIN relative to the MCA EXIN is bigger than in the single frequency case.

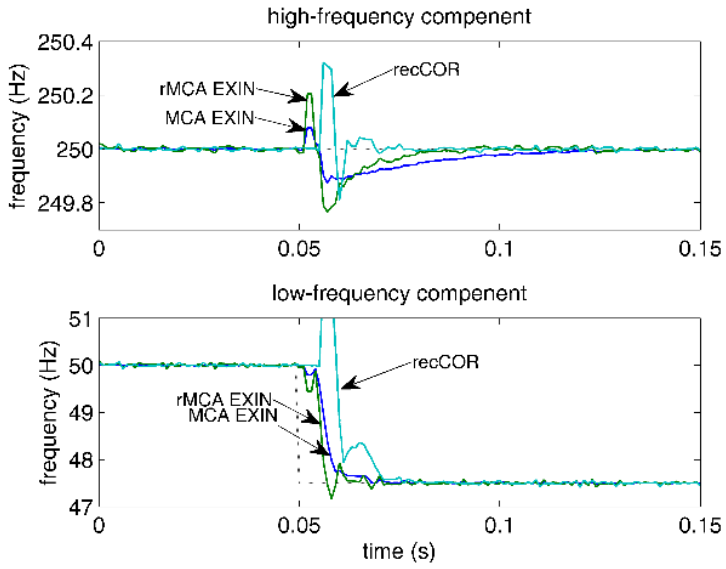

Fig 5-11 Tracking capability of the MCA EXIN method with two sinusoids

5.2.6 Numerical Simulation of the Adaptive MCA EXIN

The performance of the proposed adaptive MCA EXIN method have been evaluated using Matlab/Simulink environment. It was compared with the variable forgetting factor RTLS algorithm in [126] and RLS in [127]. Both of them require $\boldsymbol{O}(N^2)$ computational complexity, but the proposed algorithm has only $\boldsymbol{O}(N)$. They are not originally built to estimate the frequency, but have been integrated into the Pisarenko's theory, thus the three can be compared using the frequency estimation results with same conditions.

Tab.5-4 shows the parameters in the simulation unless they are indicated elsewhere. The name of the parameters are compact with their original paper. It should be noted that for the proposed algorithm, m generally controls the MSFE at steady-state, while the term $n\bar{J}$ mainly control the adapting speed. It is already known that $\bar{J}$ converges to the minimum eigenvalue, thus it will stabilizes at different values which are dependent of SNR, a single value n is not always the best choice unless $\bar{J}$ is normalized according to SNR, this can be done by adding another subspace tracking process, here however, only the constant n is used.

Tab 5-4 Parameters used in the simulation of adaptive MCA EXIN

Algorithm	Parameters
Proposed Algorithm	$\alpha(0)$=0.01,n=10,m=0.04, $\bar{J} = mean(r(k)), k = t, \dots, t-9,$
RLS	α=0.3, β=0.99, μ=0.04,$\omega(0)$=0.98
RTLS	μ=0.95, $\lambda(0)$=0,$\boldsymbol{\pi}(0)$=0,$\mathbf{g}_M$=0,$\bar{\boldsymbol{g}}_M$=0,

A. The MCA EXIN with constant learning rate

Fig.5-12 shows the MSFE results versus learning rate. The MCA EXIN algorithm has been implemented with different learning rate, but always been initiated by the same initial weights. As expected, a smaller α enables the proposed algorithm to track the system frequency more accurately (lower MSFE) but at the expense of slower convergence, and vice versa. This is due to the fact that the MCA EXIN employs a stochastic gradient approach to recursively minimize the RQ of input autocorrelation matrix, and the learning rate controls the trade-off between the convergence speed and steady state estimation accuracy. This trade-off, however, is a common problem faced by all the gradient based algorithms.

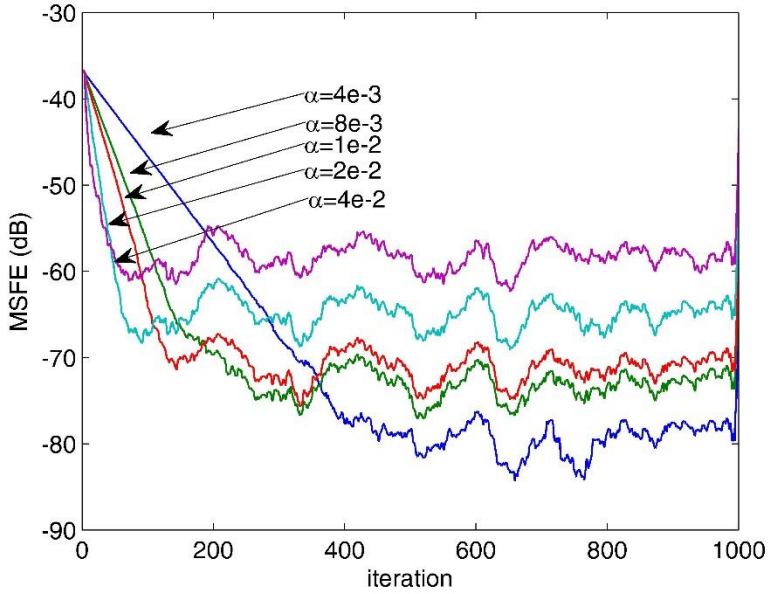

Fig 5-12 Frequency estimation performance of the MCA EXIN algorithm for variant learning rate, with SNR=40dB and, $\omega = 0.1\pi$ initiated by the same conditions

B. The overall performance verification

In this evaluation, the overall performance of the proposed algorithm are compared with the RLS and RTLS algorithms. The input frequency switches between $\omega_{ref} = 0.3\pi$ and 0.5π every 250 iterations. The input of the signal is perturbed by zero mean Gaussian white noise, SNR=20dB. Due to the trade-off between converging speed and steady-state MSFE, any separate investigation of either tracking speed or MSFE will be meaningless. The following figures will show this two aspect of results in the same time, using the same parameter setting.

The tracking performance of the algorithms are shown in fig. 5-13a, where the corresponding tracking errors are shown in fig.5-13b. These results show that all of them can track the target properly. However, it can be observed from fig.5-13b the RLS method, although its transient are fast and with less fluctuations, is biased at steady-state. This is due to fact that the noise also present in the observation vector, which is unfortunately not taken into consideration by the RLS algorithm. The proposed algorithm, on the other hand, tracks the frequency variation faster than the RTLS. Because they consider the errors both in the data matrix and observation vector, their bias is very low.

The square frequency estimation errors are shown in fig.5-13c, they are of the same order of magnitudes. It should be noted however, the RLS and RTLS achieve the results with a much higher computation burden.

Fig.5-13d shows the adaption of learning rate for the proposed method, the global converging of learning rate is in accordance with the theoretical analysis.

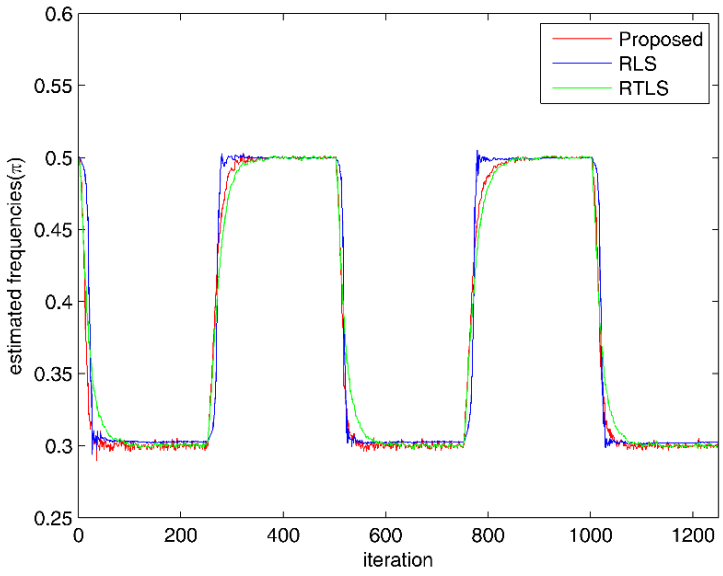

a) The estimated frequencies for the three method

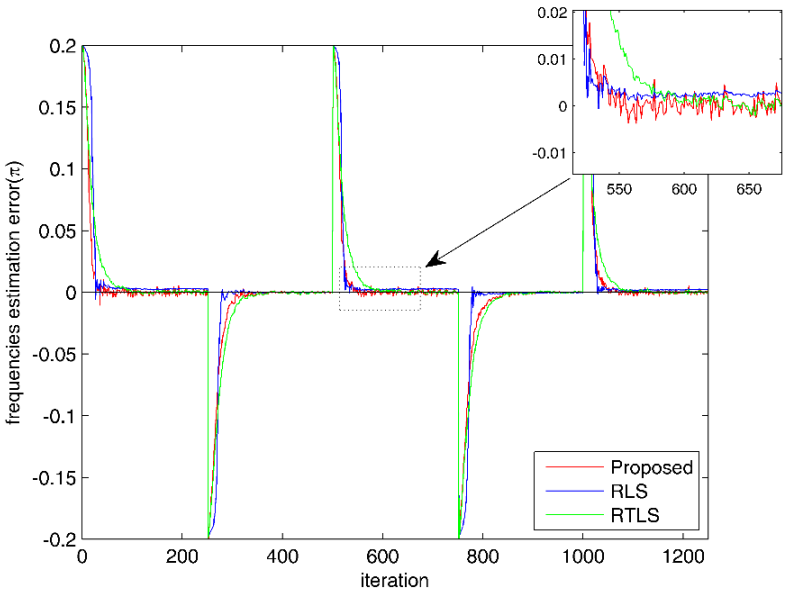

b) The frequency estimation error

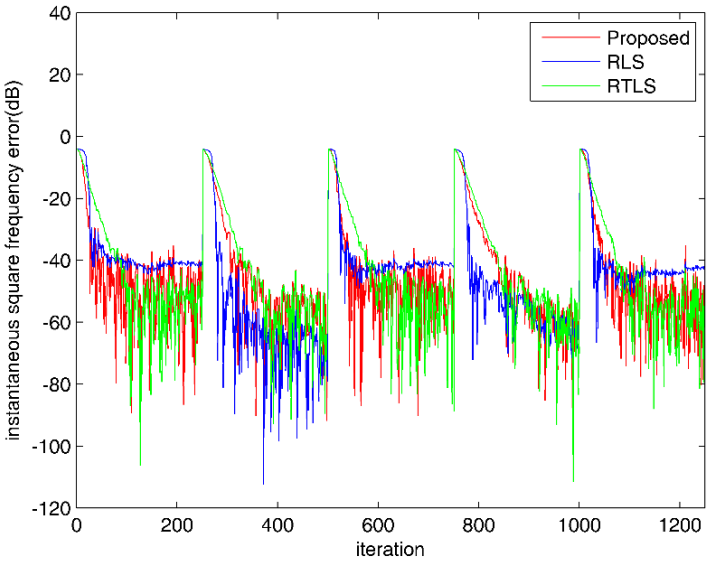

c) The square frequency estimation error

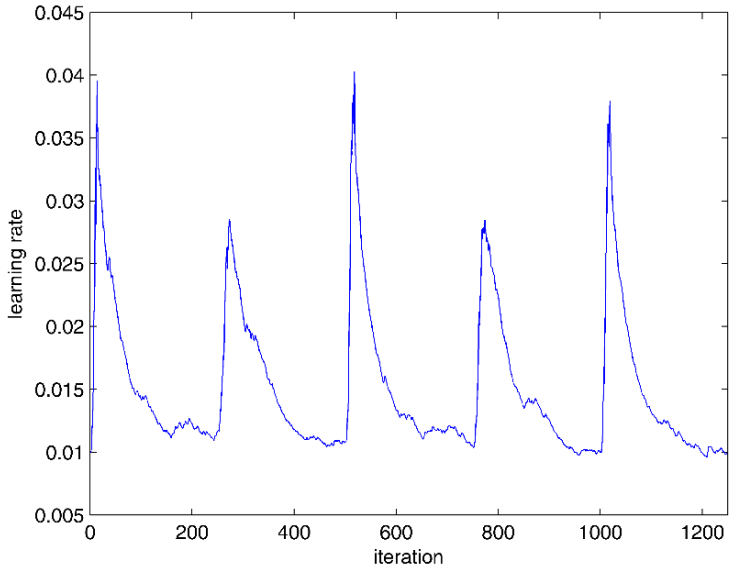

d) The adaption of learning rate

Fig 5-13 Results of adaptive MCA EXIN, tracking of the frequency switching, $\omega_{ref} = \{0.3\pi, 0.5\pi\}$ and SNR=20dB

5.3 Simulation Results of the Proposed Speed Estimator

The proposed speed estimator (with ADALINES + MCA EXIN Pisarenko structure) has been studied in Matlab/Simulink® environment. The space-vector dynamic model of the IM including rotor slotting effects, which was proposed in [41] is used for the simulation part, with the parameters shown in tab.5-5.

The speed estimation performance is verified in the framework of the measured speed based vector control system: a VSI direct rotor-flux oriented vector control [field oriented control (FOC)] in which current control is performed at the field reference frame level [1][2], the proposed speed estimator is connected on-line along with the main vector control loop (as shown in fig. 5-14), the variables $\omega_{1\text{ref}}$ and $\omega_{2\text{ref}}$, which are used for the reference of ADALINEs, are respectively taken from the PWM supply frequency and estimated by (5.11). The output of the estimator is shown together with the measured speed for comparison.

Tab 5-5 Parameters of the induction machine

Rated power P_{rated} [kW]	2.2
Rated voltage U_{rated} [V]	220
Rated frequency f_{rated} [Hz]	50
Pole-pairs	2
Stator resistance R_s [Ω]	2.9
Stator inductance L_s [mH]	223
Rotor resistance R_r [Ω]	1.52
Rotor inductance L_r [mH]	229
3-phase magnetizing inductance L_m [mH]	217
Moment of inertia J [kg·m^2]	0.0048

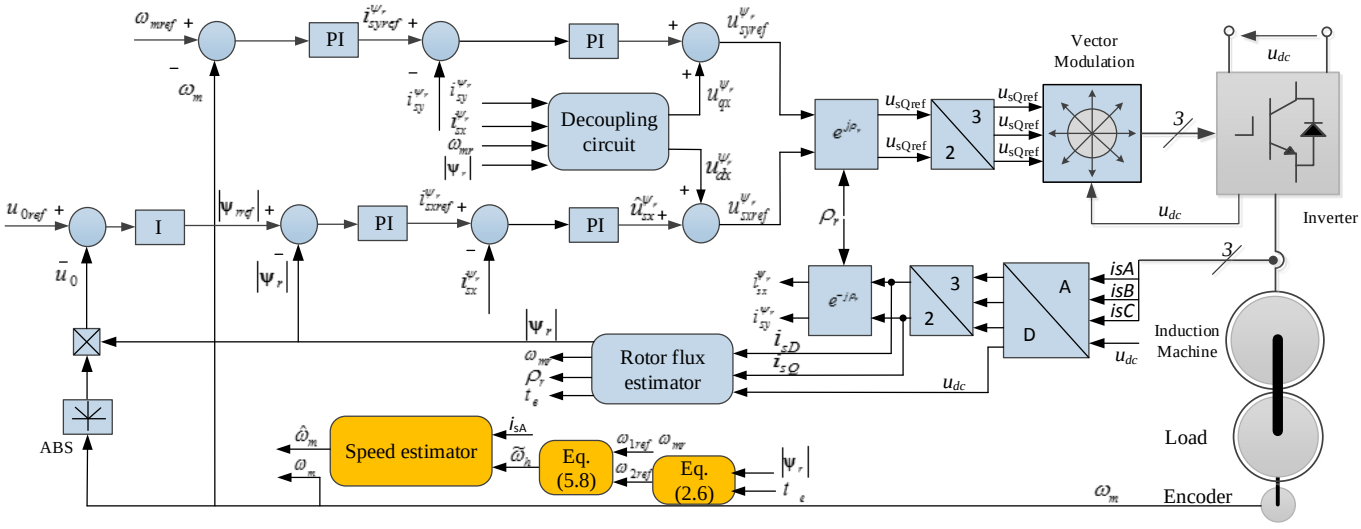

Fig 5-14 Implement field oriented scheme and speed estimation scheme

The following figures show the results of the proposed ADALINEs plus MCA EXIN pisarenko speed estimator.

Figs. 5-15~18 show the speed tracking performance at low speed range, at different loads. In fig. 5-15 and fig.5-16, the reference speed steps up from 5 rad/s to 10 rad/s, with a load of 5 Nm, while in fig.5-17 and fig.5-18 the reference speed steps down from 10 rad/s to 5 rad/s at no load.

Fig.5-15a shows that the estimated speed tracks the measured speed properly: even during the transient, the estimated speed converges to the true one, and the speed of response is fast. Fig.5-15 b shows the corresponding estimated slot frequencies.

Fig. 5-16 shows the current at the input and output of the ADALINEs. The slot current is well extracted from the stator current. In the simulation, the inductance caused by slotting effect is constant, thus the amplitude of the slot current after normalization remains almost constant.in the simulation. Although the machine current consists only of the slot harmonic and the fundamental one, nevertheless, the absence of other machine harmonics makes the choice of parameters easily coherent with the theoretical analysis, and it can provide a good guidance for the experimental part.

Fig. 5-17 shows respectively the estimated speed, measured speed and RSH frequency when the reference speed steps down at no load. Fig.5-18 shows the corresponding currents. The overall behavior is similar to the one in the step down test, which shows that the proposed speed estimator is able to work at these conditions.

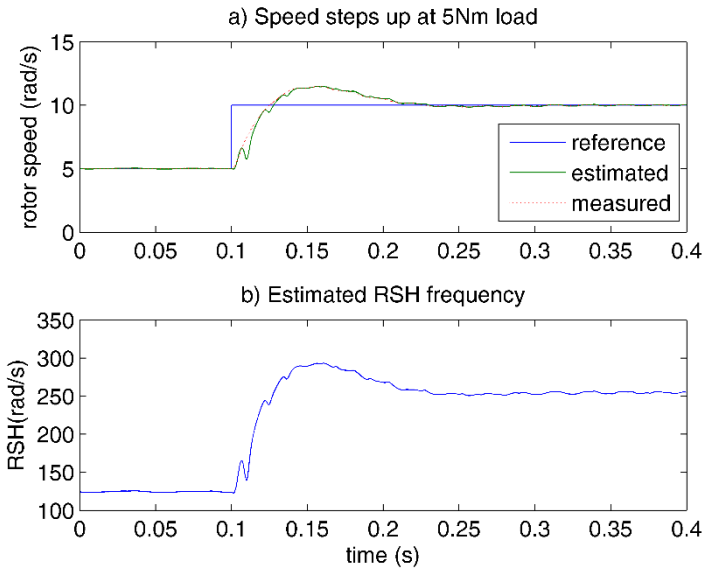

Fig 5-15 speed tracking result when speed steps up from 5 rad/s to 10 rad/s at 5Nm

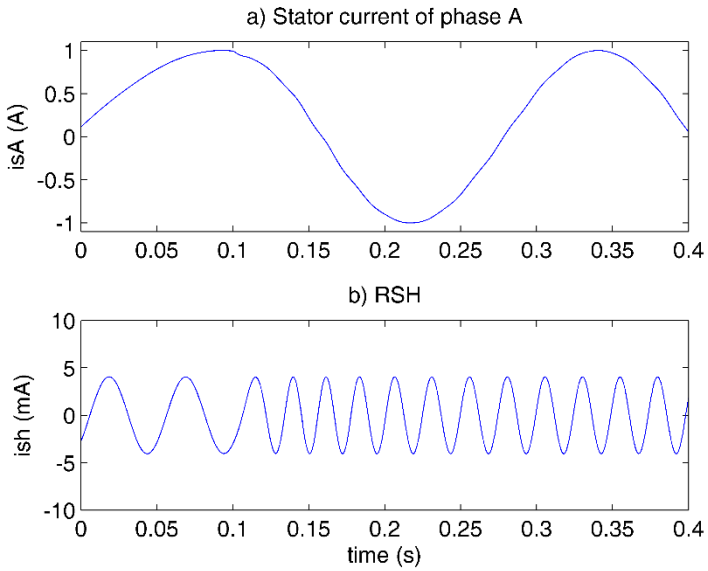

Fig 5-16 Normalized stator phase current i_{sA} and the output of ADALINE2 i_h when speed step up at 5Nm-load condition

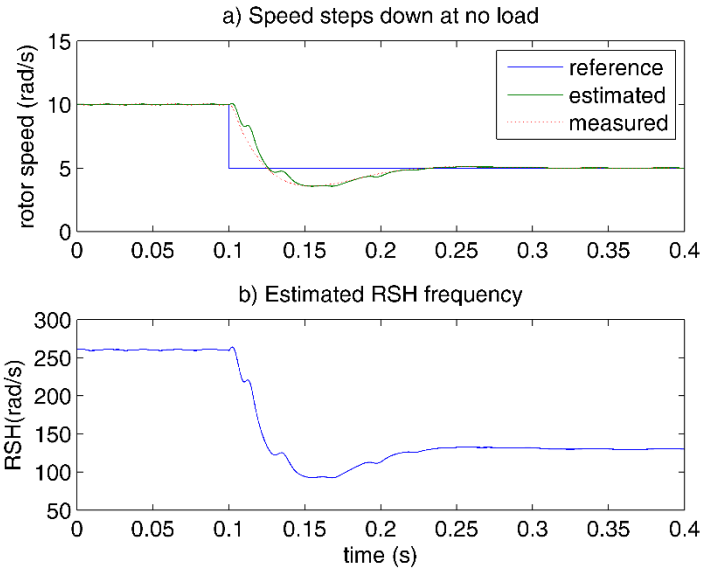

Fig 5-17 speed tracking result when speed steps down from 10 rad/s to 5 rad/s at no load

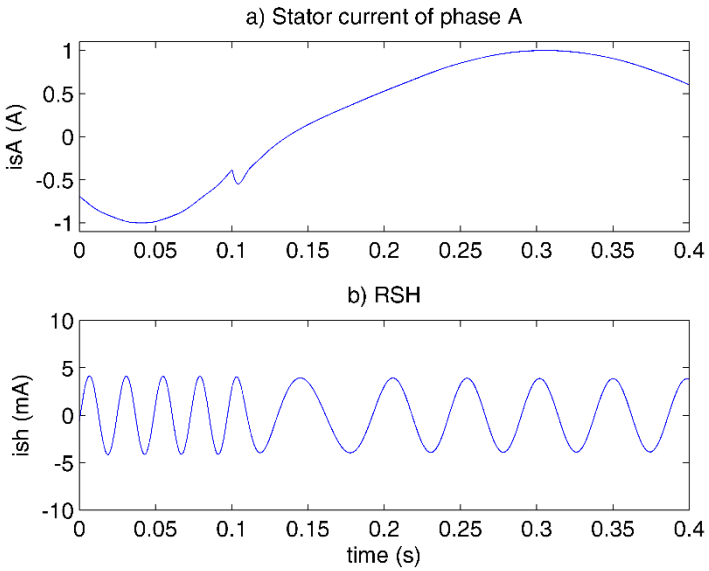

Fig 5-18 Normalized stator phase i_{sA} and the output of ADALINE2 i_h when speed step down at no load condition, from 10 to 5 rad/s

Figs. 5-19 and 5-20 show the speed tracking performance in the high speed range, with load of 10Nm. It can be observed in fig. 5-19a that the estimated speed follows the measured one closely, the speed tracking results at high speed is very accurate. Fig. 5-20 also shows that the slot harmonic is well-extracted by the ADALINEs, the frequency of it lies at higher range.

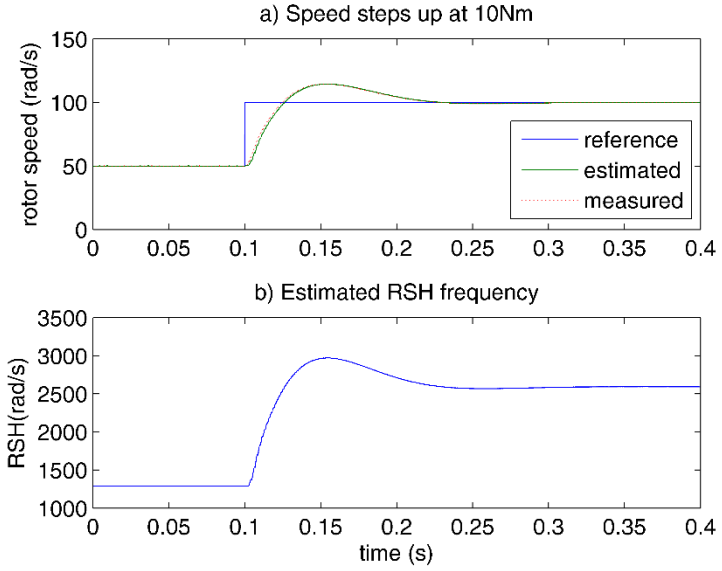

Fig 5-19 speed tracking result when speed steps up from 50 to 100 rad/s at 10Nm load

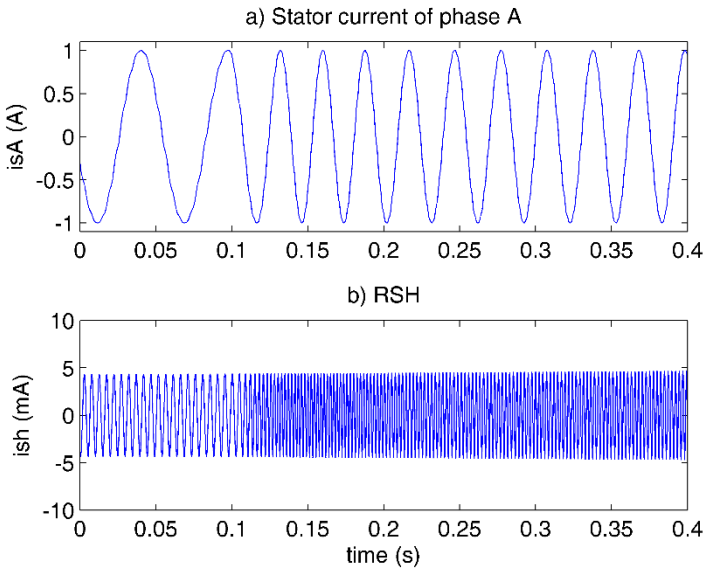

Fig 5-20 Normalized stator phase i_{sA} and the output of ADALINE2 i_h when speed step up at 10Nm condition from 50-100rad/s

Fig. 5-21 shows the results at steady-state at very low speed range: the drive is with load of 10Nm, the speed is 2, 4, 6, 8, 10 rad/s. It is apparent that the estimation speeds are in accordance with the measured ones.

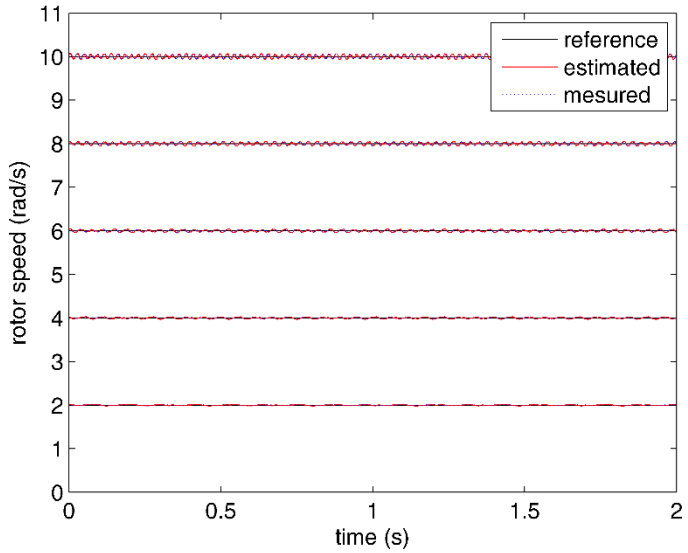

Fig 5-21 Speed estimation results at steady-state, 5Nm load

5.4 Experiment Results

The employed test set-up consists of:

- A three-phase induction machine with parameters shown in Tab.4-1, with 36 stator and 28 rotor slots.
- An 8 kVA, three-phase VSI for the control of the machine side inverter.
- A torque controlled brushless Interior Mounted Permanent Magnet (IMPM) machine drive for the load of 1.5kW.
- A dSPACE card (DS1103) with a PowerPC 604e at 400 MHz and a floating-point DSP TMS320F240 for the control of the machine side inverter.

Like in the simulations, to verify the proposed speed estimation algorithm, the measured speed (from the encoder) is used as feedback in the framework vector control, while the proposed speed estimation scheme is connected on-line along with the main vector control loop. The test is made for different loads and speed conditions. The RSH frequency varies from hundreds of hertz to only a few hertz, when the speed reference changes from 150 rad/s (rated) to 1 rad/s (1% rated), the sampling frequency for the MCA EXIN Pisarenko method is kept at 2.5k Hz. The following part only shows the results of the most challenging tests at low speed.

The tracking capability results when the speed steps up with 5Nm-load are shown in fig. 5-22 and fig.5-23.

Fig.5-22 a shows the corresponding estimated speed and the measured speed, respectively. Both the steady-state and transient performance are satisfactory. Remark that the estimated speed tracks the measured speed within 0.01s. Fig. 5-22 b shows the estimated RSH frequency from which the speed is computed. Compared to the simulation results, the oscillation of the estimated speed in experiment are larger, this is because of the presence of the machine harmonics, but the estimated speed always converge to the measured one.

Fig.5-23 presents the normalized phase current of the motor in the test. It can be observed from fig.5-23a that the stator phase current is full of harmonics, but it contains only the slot harmonics in the output of ADALINEs, with the waveform i_h stable and smooth.

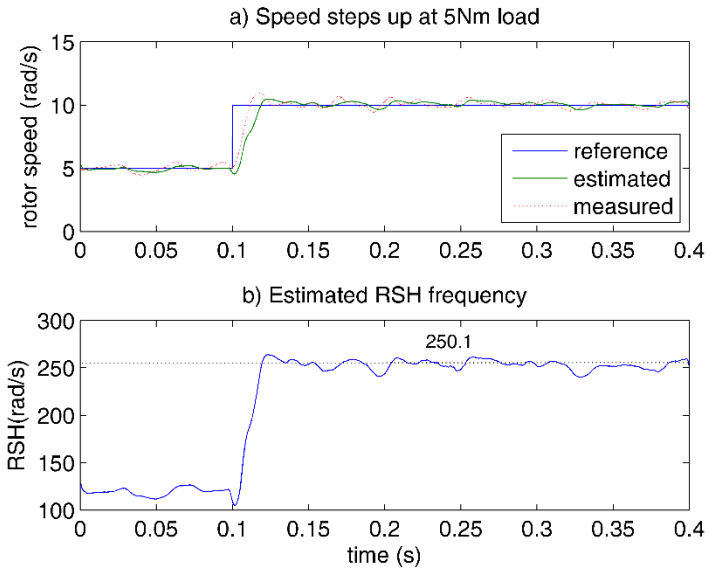

Fig 5-22 Tracking capacity when speed step up at 5Nm load condition

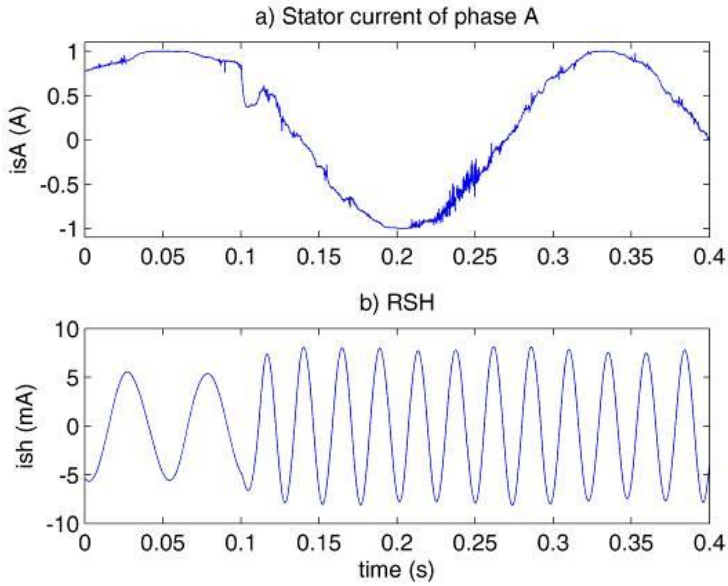

Fig 5-23 Normalized phase current i_{sA} and the output of filter i_h when speed step up at 5Nm-load condition

The tracking capability results when speed steps down are presented from fig. 5-24 and fig. 5-25, from 10 rad/s to 5 rad/s, at no load.

Fig.5-24a and b show the corresponding estimated speed and the estimated RSH frequency, respectively. The results show that the proposed algorithm can track the measured one properly, and the behavior is similar to the step up test.

The corresponding current waveform can be found in fig. 5-25.

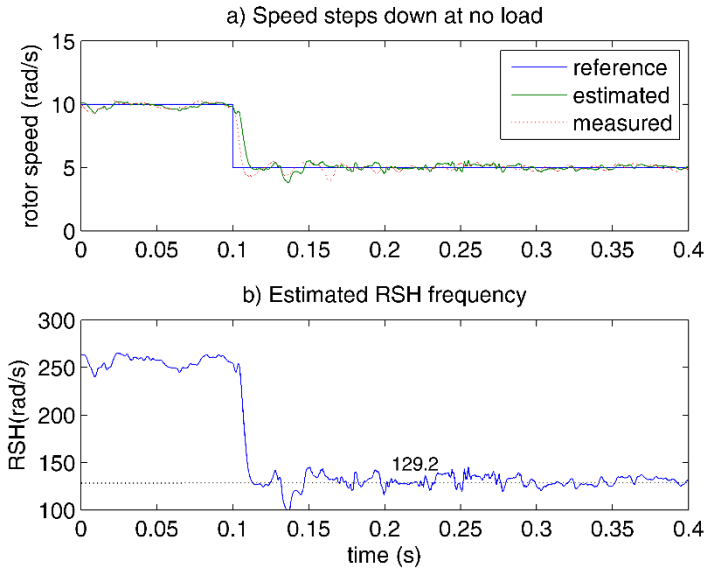

Fig 5-24 Tracking capacity when speed step down at no-load

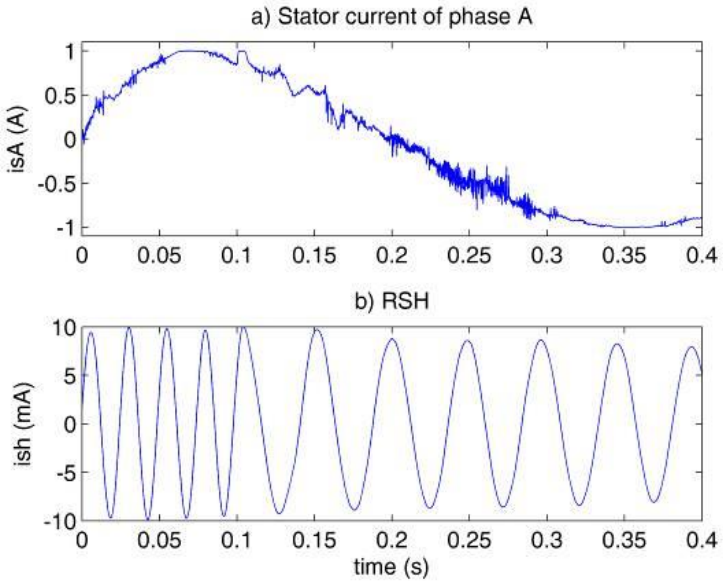

Fig 5-25 Normalized phase current i_{sA} and the output of filter i_h when speed steps down at no-load

The steady-state performance of the MCA EXIN Pisarenko method is shown in fig.5-26 and fig.5-27.

In fig. 5-26, the machine operates at no-load, the reference speed is around the values 2, 4, 6, 8, 10 rad/s. The measured speeds and the estimated speeds are shown comparatively: the estimated speeds track the measured ones accurately, for the very low speeds; even if

the measured speeds behave worse in terms of oscillation, nevertheless, the estimated speeds follows the change of the measured ones.

In fig. 5-27, the machine is 5Nm-loaded, the reference speed varies from 10 rad/s to 2 rad/s. The results are similar to the no-load case. However, it has to be stressed that the bias is larger at 2 rad/s, since when the machine is loaded, the actual RSH frequency has lower values, and the other harmonics are very close to the RSH, which is in the output of the ADALINEs can appear. Moreover, at 2 rad/s, the RSH frequency is just a few hertz, and like most of the frequency estimation methods, the mean square estimation error will increase. This can be improved by adopting a smaller sampling frequency, and a slower response is to be expected.

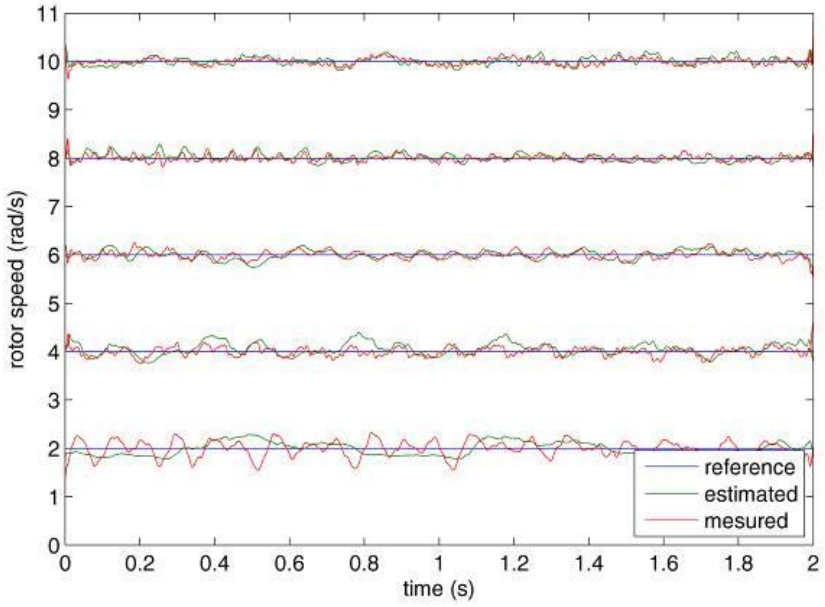

Fig 5-26 Speed estimation results at steady-state no load

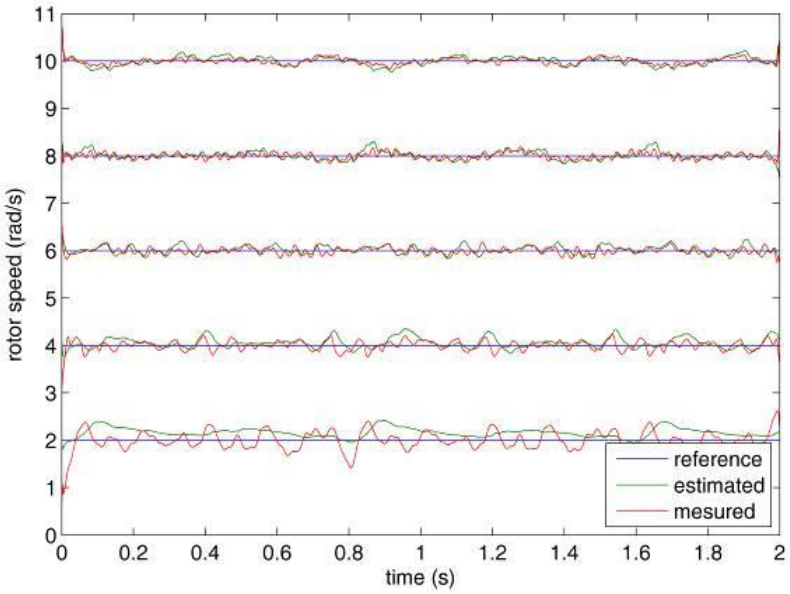

Fig 5-27 Speed estimation results at steady-state 5Nm load

5.5 Summary

In this chapter, the speed related rotor slot harmonic is extracted from the stator phase current by two ADALINEs: one works in notch mode in order to eliminate the fundamental current, the other works in band mode thus its output consists only of the slot harmonic. The frequency of this harmonic is then estimated by using MCA EXIN neural networks based on Pisarenko theory: The neural weights converge to the eigenvector corresponding to the minimum eigenvalue of the input autocorrelation matrix, which is the output of ADALINEs in this case, thus the frequency can be estimated by finding all the roots of the polynomial equation formed by this eigenvector in Pisarenko theory. However, compared to the original Pisarenko's method, the computational complexity and mean square frequency estimation error are largely reduced, and the proposed frequency estimator can work recursively sample by sample. The overall speed estimation algorithm is fast and accurate, its performance has been verified both in the simulation and in the experiment.

CHAPTER 6. CONCLUSIONS AND FUTURE WORK

This thesis proposed the techniques using a higher harmonic model of the induction motor which takes into account the rotor slot effects and its use for the computation of the rotor speed of induction motors (IMs). It is characterized by a very low sensitivity to the parameters variations. The proposed algorithms fulfill the requirements of steady-state accuracy and transient behavior.

Conclusions in specific areas are summarized in the following sections.

6.1 Speed Detection by Tracking Rotor Slot Harmonics

It was already known from the previous literatures that the rotor slot harmonics are detectable, and are related to the instantaneous rotor speed. Several investigative studies have been taken in this thesis, and this thesis proposed to divide the RSH tracking approaches into two main categories:

1). *Frequency domain methods*, which are mainly based on FFT (Fast Fourier Transform)-like approaches;

2). *Time domain methods*, which are mainly based on PLL (Phase-Locked Loop)-like approaches.

The former generally provides good accuracy and linearity over a very wide speed range and load conditions, but a compromise has to be made between the required frequency resolution, to allow speed detection, and the response time versus changes of speed. The latter can provides a better real time performance than the frequency domain method, although the accuracy of the result will be affected by the noise level. It generally behaves like such a band-pass filter: the gain is very large at the RSH frequency and very small away the RSH frequency, thus it usually needs a better prior knowledge of the location of expected RSH frequency.

Considering all the pros and cons, this thesis focused on the time domain method, making it better suited for real-time applications. On the basis of that, two main approaches have been proposed

1) A phase-locked loop (PLL) structure. The centre bandwidth of PLL was tuned on-line on the basis of the reference values of the supply and slip frequencies provided to the PWM converter, tracking the machine rotor slotting harmonic without the need of any high frequency signal injection, neither rotating nor pulsating, this results in tracking the machine speed in a very wide speed range (from rated speed down to as much as 2% of it). Meanwhile, the frequency of the slot harmonic is available directly in the framework of PLL.

2) The ADALINEs plus MCA EXIN Neural Networks structure. First, two cascaded ADALINEs were used to extract the rotor slot harmonic from the input stator phase current, acting as adaptive filters and whose output consists only of the slot harmonic. Then, the MCA EXIN neurons were used to extract the eigenvector corresponding to the minimum eigenvalue of the autocorrelation matrix formed by the ADALINEs' output sequence: as a matter of fact, the slot frequency can then be estimated by finding all the roots of the polynomial equation formed from this eigenvector by using Pisarenko's theory. Moreover not only can the proposed neural networks work recursively sample by sample, but the computational complexity and mean square frequency estimation errors are largely reduced.

6.2 Sensorless Scalar Drive by PLL Speed Detector

The proposed PLL speed estimator has been applied to a scalar controlled drive. The speed estimation performed on the basis of a PLL algorithm is of a particular interest in terms of a potential industrial applications: with the aim of developing a low cost, computationally light sensorless drive, where the number of parameters to be tuned, both in the controller and in the estimator, is very limited in comparison with more performing sensorless drives. In particular, as for the control algorithm, only the PI control is to be tuned and only the stator and rotor resistances are to be known (only if voltage drop compensation is to be performed). As far as the PLL speed estimator is concerned, the only tuning parameters are the PLL gain and the cut-off frequency of its low pass filter while the only machine parameter to be known is the number of rotor slots per phase and per pole. This makes the methodology easily exportable to several other types of drives.

6.3 Improved Frequency Estimation Algorithms

According to the Pisarenko's theory, it has been verified that the minor component which lies in the noise subspace is orthogonal to the signal subspace, thus, the signal frequencies contained in the input can be computed from a polynomial formed by the MC. When the original Pisarenko's method is used to estimate the frequency, it is limited by: 1) the estimation of the autocorrelation sequence, 2) the general difficulties involved in determining the eigenvalues and eigenvectors of autocorrelation matrix.

This thesis has improved the Pisarenko's method by using the MCA EXIN neurons, which deals with the recovery of eigenvectors of the data sequence's autocorrelation matrix. Thus, the estimation algorithm can retrieve the MC recursively with less computation and improved error performance (the solution is of total least square meaning).

Moreover, two improvements have been made to the original MCA EXIN methods.

1) The rMCA EXIN. Consider a stream of signals $x \in \mathbb{R}^{2p+1}$ where $2p$ is the number of harmonics in the signal (p complex frequencies), then the input signal has been projected to a reduced space $y \in \mathbb{R}^{p+1}$, thus, the convergence rate is accelerated and the computational complexity is reduced by p.

2) The adaptive MCA EIXN. The learning rate of the MCA EXIN is normally assumed to be constant or exponentially decreasing to zero, however, on the basis of convergence study on the conventional gradient MCA algorithm, this thesis proposed a data-driven adaptive learning rate. This new algorithm, gives faster tracking and smaller mean square error.

6.4 Directions for Future Work

Future work could proceed efficiently in several directions:

1) The speed estimation algorithm which combines the signal injection algorithm with the proposed slot harmonics based algorithm: either the two algorithms work in parallel, or the slot harmonics tracking algorithm works in the high speed range, while the signal injection works in the low speed range. Thus, the sensorless algorithm can works efficiently in a wider range (from rated speed down to zero speed theoretically).

2) Experiment verification of the proposed speed detection algorithms both in scalar controlled and vector controlled drives.

3) The gradient based frequency estimation with improved converging speed and reduced frequency estimation error. To achieve this, a better learning rate adaptive mechanism has to be adopted. Meanwhile, the non-linear type MCA algorithms can be developed to increase the noise rejection ability.

4) Instead of estimating the frequency in the presence of noise under the framework of Pisarenko's theory, the minor space analysis (MSA) neural networks can be used to estimate the frequency under the framework of MUSIC theory, thus the mean square estimation error can be reduced.

5) Algorithms that are able to determine the model order of the Pisarenko's method and MUSIC's method automatically by using some criterion, such as Akaike information criterion (AIC), yet the computational complexity remains as low as possible.

APPENDIX A SPACE VECTOR MODEL OF IM INCLUDING THE ROTOR SLOTTING EFFECTS

The full-state space-vector model of the induction machine, including rotor slotting effects was given in [41] as,

$$\frac{d}{dt}\begin{bmatrix}\mathbf{i}_s\\ \boldsymbol{\psi}_r'\end{bmatrix}=\begin{bmatrix}\mathbf{A}_{11} & \mathbf{A}_{12}\\ \mathbf{A}_{21} & \mathbf{A}_{22}\end{bmatrix}\begin{bmatrix}\mathbf{i}_s\\ \boldsymbol{\psi}_r'\end{bmatrix}+\begin{bmatrix}\mathbf{B}_1\\ 0\end{bmatrix}\mathbf{u}_s=\mathbf{A}\mathbf{x}+\mathbf{B}\mathbf{u}_s \tag{A.1}$$

$$\mathbf{i}_s=\mathbf{C}x \tag{A.2}$$

Where

$$\mathbf{A}_{11}=\frac{1}{L_s+L_he^{\mp jq_r\theta_r}-\frac{L_m^2}{L_r+L_he^{\pm jq_r\theta_r}}}\left\{-R_s-\frac{R_rL_m^2}{\left(L_r+L_he^{\pm jq_r\theta_r}\right)^2}\pm j\omega_r\left[q_rL_he^{\mp jq_r\theta_r}-\frac{q_rR_rL_mL_h}{\left(L_r+L_he^{\pm jq_r\theta_r}\right)^2}e^{\pm jq_r\theta_r}\right]\right\}$$

$$\mathbf{A}_{12}=\frac{1}{L_s+L_he^{\mp jq_r\theta_r}-\frac{L_m^2}{L_r+L_he^{\pm jq_r\theta_r}}}\left\{\frac{R_rL_m}{\left(L_r+L_he^{\pm jq_r\theta_r}\right)^2}+j\omega_r\left[\pm\frac{q_rL_mL_h}{\left(L_r+L_he^{\pm jq_r\theta_r}\right)^2}e^{\pm jq_r\theta_r}-\frac{L_m}{L_r+L_he^{\pm jq_r\theta_r}}\right]\right\}$$

$$\mathbf{A}_{21}=\frac{R_rL_m}{L_r+L_he^{\pm jq_r\theta_r}},\ \mathbf{B}_1=\frac{1}{L_s+L_he^{\mp jq_r\theta_r}-\frac{L_m^2}{L_r+L_he^{\pm jq_r\theta_r}}},\mathbf{C}=\begin{bmatrix}\mathbf{I} & \mathbf{0}\end{bmatrix};$$

Where

L_s, L_r, L_m, L_h are respectively the stator and rotor inductance without slotting, magnetizing inductance, and the slot inductance;

q_s , q_r are the number of stator and rotor slots per pole pair;

θ_r angular position of rotor a-phase with respect to stator a-phase (positive if counterclockwise);

$\mathbf{i}_s$,, $\mathbf{u}_s$ and $\boldsymbol{\psi}_r'$ are respectively the stator current space vectors, stator voltage space vector and the rotor flux linkage space vectors in the stator reference frame.

The upper sign refers to the case q_r=3n−1, q_s=3m−1and the lower one to the case q_r = 3n + 1. q_s = 3m + 1, with n, $m \in N$

In the Matlab/Simulink environment, an IM model including rotor slot effect has been built, the validity of the space-vector dynamic model of IM has been verified, at different supply voltage, and load conditions.

The IM model including slot effect has been tested at different supply voltage with constant V/f. At each supply voltage, different values of load torque have been applied to the machine. The corresponding stator current harmonics have been examined according to (eq.

2.2) at each condition, to verify the validity of the model. Some of those results are shown below:

Figs. A-1 and A-2 show the waveforms of stator current and its spectrum when the supply voltage is 50Hz (rated), respectively under no-load and full-load; the corresponding rotor speed is also shown. Figs. A-3 and A-4 show respectively the waveform of the rotor speed, the stator current and its current spectrum and for 15Hz supply voltage at no-load and full load. Some key information obtained from figs. A-1 to A-4 are listed on table A-1 for comparison.

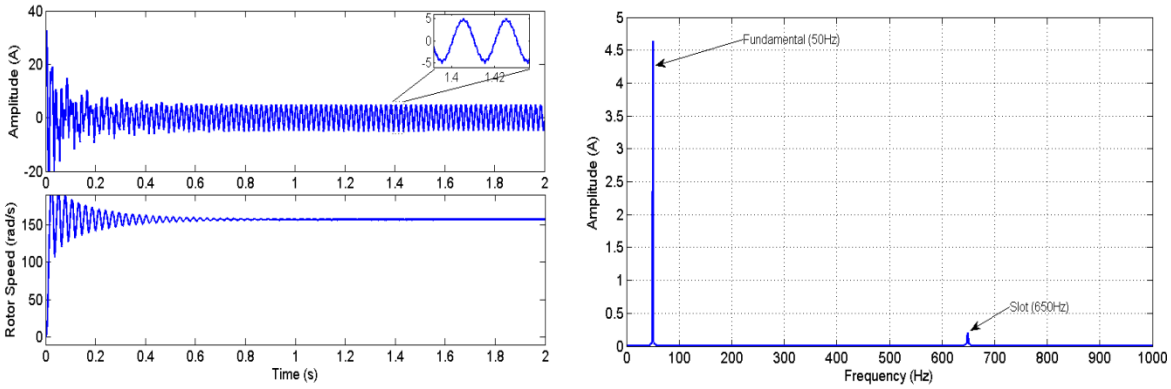

Fig A-1 Current Signature at 50 Hz supply frequency and no load

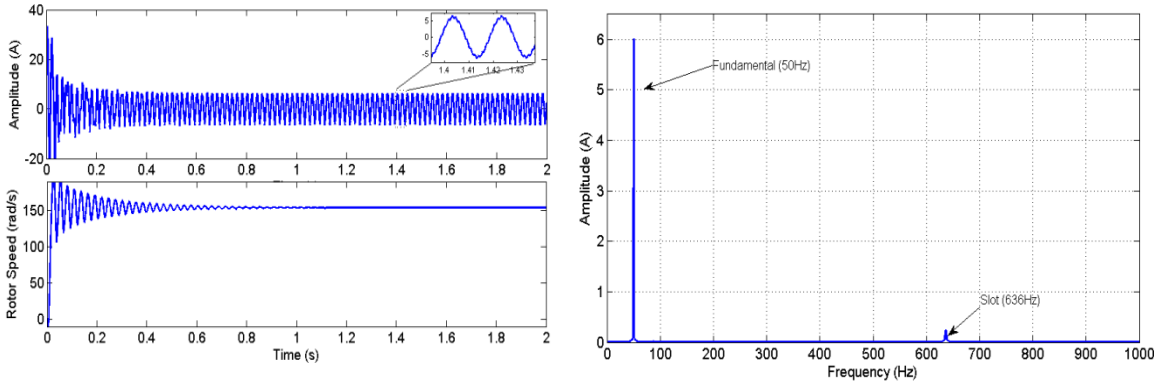

Fig A-2 Current signature at 50 Hz supply frequency and full load

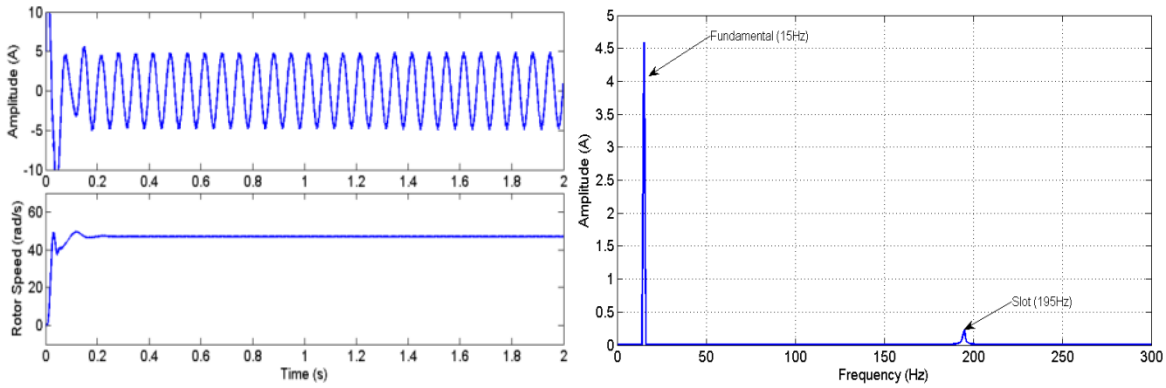

Fig A-3 Current signature at 15 Hz supply frequency and no load

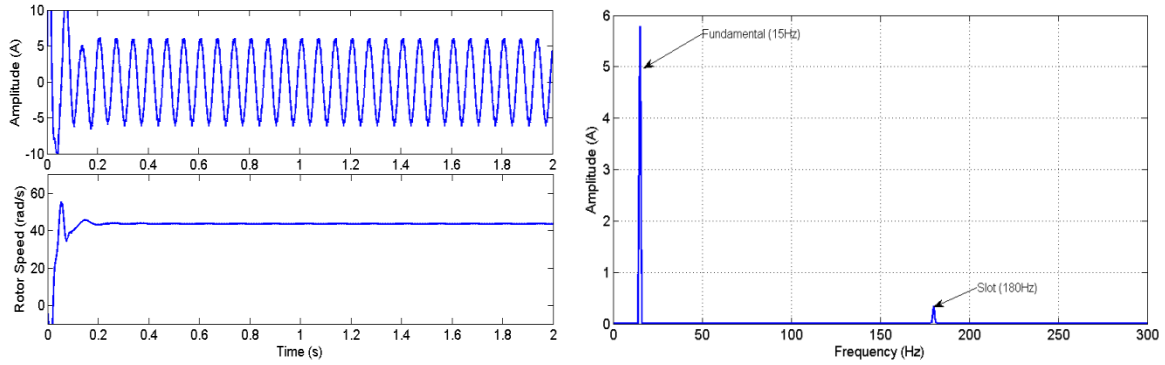

Fig A-4 Current signature at 15 Hz supply frequency and full load

Table A-1 Results of the Stator Current Signature Test

	f_1		f_{RSH}		ω_m
Conditions	Frequency (Hz)	Amplitude (A)	Frequency (Hz)	Amplitude (A)	(Rad/s)
50Hz No-Load	50	4.6	650	0.2	156.7
50Hz 10Nm-Load	50	6	636	0.24	154
15 Hz No-Load	15	4.6	195	0.23	47.1
15Hz 10Nm-Load	15	5.78	180	0.35	43.8

It can be found that all the slot harmonics appear at frequencies in accordance with the theoretical values calculated from (2.2), which verifies the validity of the simulation IM model. It should be noted that in the simulation model, the IM presents no other harmonics except the RSH, which is apparently not the case in practice.

Remark that, at full load, decreasing the supply voltage and frequency, the amplitudes of the first and slot harmonic increase. The variations in harmonic magnitude do not affect the algorithm as long as the slot harmonics are above the noise level.

APPENDIX B PROF OF PISARENKO'S THEORY

(**Eigen-Decomposition of the Autocorrelation Matrix**)

It is assumed that the data sample is a sum of *p* (usually considered known) complex exponentials in white noise,

$$x(n) = \sum_{i=1}^{p} A_i e^{j\omega_i n} + \upsilon(n) \tag{B.1}$$

Where v(n) is zero mean white noise with variance σ^2; A_i, ω_i are respectively the complex amplitude, and the principal argument of the angular frequency of the i^{th} exponential. The complex amplitudes $\boldsymbol{A}_i$ are given by,

$$\mathbf{A}_i = |A_i| e^{j\varphi_i} \tag{B.2}$$

Where $|A_i|$ is the amplitude, while the phases φ_i are considered uncorrelated random variables uniformly distributed over the interval [0, 2π).

Given the process (B.1), the auto correlation function is easily shown to be

$$r_{xx}(k) = \sum_{i=1}^{p} A_i^2 \exp(jk\omega_i) + \sigma^2 \delta(k) \tag{B.3}$$

Let $P_i=A_i^2$ denote the power of the i^{th} sinusoid, then the $M\times M$ autocorrelation matrix for $M>p$ is given by

$$\underbrace{\mathbf{R}_{xx}}_{M\times M} = \underbrace{\mathbf{R}_{ss}}_{M\times M} + \underbrace{\mathbf{R}_{vv}}_{M\times M} = \sum_{i=1}^{p} P_i \mathbf{e}_i \mathbf{e}_i^H + \sigma^2 \mathbf{I} \tag{B.4}$$

Where $\mathbf{e}_i = \begin{bmatrix} 1 & e^{j\omega_i} & e^{j2\omega_i} & \cdots & e^{j(M-1)\omega_i} \end{bmatrix}^T$ is the signal vector. The set of { $\mathbf{e}_i$ } *i=1,2…,p* form a linearly independent vector spanning $\mathbb{R}^M$. $\mathbf{R}_{xx}$ is the autocorrelation matrix of the signal, $\mathbf{R}_{ss}$ is the autocorrelation matrix of the signal without noise. (B.4) can also be written in matrix form as follows:

$$\mathbf{R}_{xx} = \mathbf{E}\mathbf{P}\mathbf{E}^H + \sigma^2 \mathbf{I} = \mathbf{R}_{ss} + \sigma^2 \mathbf{I} \tag{B.5}$$

Where $\mathbf{E}=[\mathbf{e}_1,\ldots,\mathbf{e}_p]$ is an $M \times p$ matrix containing the p signal vectors $\mathbf{e}_i$, and $\mathbf{P}=\text{diag}[P_1,\ldots,P_p]$ is the diagonal matrix containing the signal powers.

From (**B**.5), $\mathbf{R}_{xx}$ is the sum of the signal autocorrelation matrix $\mathbf{R}_{ss}$ and the noise autocorrelation matrix $\mathbf{R}_{vv}=\sigma^2\mathbf{I}$. $\mathbf{R}_{xx}$ is of rank p because it is the sum of p diagonal products. The total autocorrelation matrix $\mathbf{R}_{xx}$ is, however, full rank due to the inclusion of the $\sigma^2\mathbf{I}$ term. It can be easily proved [102], [128] that the eigenvalues of $\mathbf{R}_{xx}$ are $\{\lambda_1+\sigma^2, \ldots, \lambda_p+\sigma^2, \sigma^2,\ldots, \sigma^2\}$ where $\{\lambda_1,\ldots, \lambda_p\}$are the eigenvalues of $\mathbf{R}_{ss}$ and $\lambda_1\geq\lambda_1\geq\ldots\geq\lambda_p\geq 0$. Since the autocorrelation matrix $\mathbf{R}_{ss}$ is semi-definite positive. Then the first p eigenvalues of $\mathbf{R}_{xx}$ are greater than σ^2 and the last M-p eigenvalues are equal to σ^2. The eigenvalues and eigenvectors of $\mathbf{R}_{xx}$ may therefore be divided into two groups: the signal eigenvectors $\mathbf{v}_1,\ldots,\mathbf{v}_p$ that have eigenvalues greater than σ^2,which span the p dimensional signal subspace, and the noise eigenvectors $\mathbf{v}_{p+1},\ldots,\mathbf{v}_M$ that have eigenvalues equal to $\sigma^2$and span the noise subspace.

Thus, for p complex frequencies, a related eigen decomposition based on the eigenvectors $\mathbf{v}_i$ and eigenvalues λ_i of $\mathbf{R}_{xx}$ produces,

$$\mathbf{R}_{xx}=\sum_{i=1}^{p}\left(\lambda_i+\sigma^2\right)\mathbf{v}_i\mathbf{v}_i^H+\sum_{i=p+1}^{M}\left(\sigma^2\right)\mathbf{v}_i\mathbf{v}_i^H \tag{B.6}$$

Where the signal autocorrelation matrix has been replaced by $\sum_{i=1}^{p}\lambda_i\mathbf{v}_i\mathbf{v}_i^H$ and the decomposition of **I** has been used. Now if the eigenvectors $\mathbf{v}_{p+1},\ldots,\mathbf{v}_M$ of $\mathbf{R}_{xx}$ are considered, which span the noise subspace, then the following equation holds,

$$\mathbf{R}_{xx}\mathbf{v}_{p+j}=\sigma^2\mathbf{v}_{p+j} \qquad j=1,\ldots,M\text{-}p, \tag{B.7}$$

This together with (B.5),

$$\mathbf{R}_{ss}\mathbf{v}_{p+j}=0 \qquad j=1,\ldots,M\text{-}p, \tag{B.8}$$

Or,

$$\mathbf{EPE}^H\mathbf{v}_{p+j}=0 \qquad j=1,\ldots,M\text{-}p, \tag{B.9}$$

Premultiplying by $\mathbf{v}_{p+j}^H$ yields,

$$v_{p+j}^H\mathbf{EPE}^H\mathbf{v}_{p+j}=(\mathbf{E}^H\mathbf{v}_{p+j})^H\mathbf{P}(\mathbf{E}^H\mathbf{v}_{p+j})=0 \tag{B.10}$$

Since **P** is positive definite it follows that

$$\mathbf{e}_i^H\mathbf{v}_{p+j}=0 \qquad i=1,2,\ldots p,\ j=1,\ldots,M\text{-}p, \tag{B.11}$$

Hence the signal vectors are orthogonal to all vectors in noise subspace as linked at above. This property forms the basis for the frequency estimation algorithm among which the Pisarenko method. In this method, M is chosen to be p+1 so the noise subspace has dimension of 1. (B.11) can be therefore rewritten in the more familiar form

$$V_{\min}(e^{j\omega}) = \sum_{k=0}^{p} \mathbf{v}_{p+1}(k)\ e^{-j\omega_i k} = 0 \quad i=1,2,\ldots,p \tag{B.12}$$

Consequently, the z-transform of the noise eigenvector, $\mathbf{v}_{\min}$, has p zeros on the unit circle,

$$V_{\min}(z) = \sum_{k=0}^{p} \mathbf{v}_{\min}(k) z^{-k} = \prod_{k=0}^{p} (1 - e^{j\omega_k} z^{-1}) \tag{B.13}$$

corresponding to the p harmonics of the signal, the frequencies of the complex exponentials can be extracted from the roots of $V_{\min}(z)$.

APPENDIX C MCA ALGORITHMS AND THE ASSESSMENT SOFTWARE

1. The MCA Linear Neurons

The minor component analysis (MCA) deals with the recovery of the eigenvector associated to the smallest eigenvalue of the autocorrelation matrix of the input data and is a very important tool for signal processing and data analysis. It is almost exclusively solved by linear neurons. Fig. C-1 shows the structure of the MCA linear neurons.

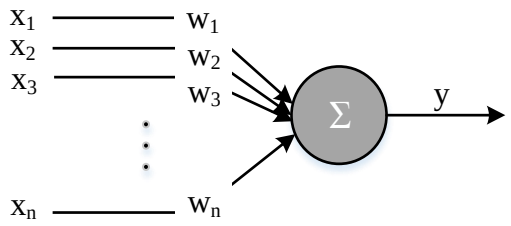

Fig C-1 The structure of the MCA linear neurons.

The linear neuron has a real number input vector $\mathbf{x}(t) = [x_1(t), \ldots, x_N(t)]^T$ and output y(t):

$$y(t) = \mathbf{w}^T(t)\mathbf{x}(t) = \sum_{i=1}^{N} w_i(t)x_i(t) \tag{C.1}$$

where $\mathbf{w}(t) = [w_1(t), \ldots, w_N(t)]^T$ is the weight vector.

The update of the weights, following different gradient flows, are listed as below:

A. The OJA's Learning Laws

$$\mathbf{w}(t+1) = \mathbf{w}(t) - \alpha(t)y(t)\left[\mathbf{x}(t) - y(t)\mathbf{w}(t)\right] \tag{C.2}$$

B. The explicitly normalized version of Oja's learning law (OJAn)

$$\mathbf{w}(t+1) = \mathbf{w}(t) - \alpha(t)y(t)\left[\mathbf{x}(t) - \frac{y(t)\mathbf{w}(t)}{\mathbf{w}^T(t)\mathbf{w}(t)}\right] \tag{C.3}$$

C. The Luo-Unbehauen-Cichocki's learning law (LUO)

$$\mathbf{w}(t+1) = \mathbf{w}(t) - \alpha(t)\left[\mathbf{w}^T(t)\mathbf{w}(t)y(t)\mathbf{x}(t) - y^2(t)\mathbf{w}(t)\right] \tag{C.4}$$

D.The Feng-Bao-Jiao's Learning Law

$$\mathbf{w}(t+1) = \mathbf{w}(t) - \alpha(t)\left[\mathbf{w}^T(t)\mathbf{w}(t)y(t)\mathbf{x}(t) - \mathbf{w}(t)\right] \tag{C.5}$$

E. The EXIN learning law

$$\mathbf{w}(n+1) = \mathbf{w}(n) - \frac{\alpha(n)y(n)}{\mathbf{w}^T(n)\mathbf{w}(n)}\left[\mathbf{x}(n) - \frac{y(n)\mathbf{w}(n)}{\mathbf{w}^T(n)\mathbf{w}(n)}\right] \tag{C.6}$$

An evaluation software has been built in MATLAB/GUIDE, whose desktop is shown in fig. C-2. The MCA learning law with respect to different configuration can be studied in the software, i.e. the initial value, the learning rate, and the noise level of the training set. Meanwhile the performance of the results (weights, lambda, and rho) will be show graphically in the plot.

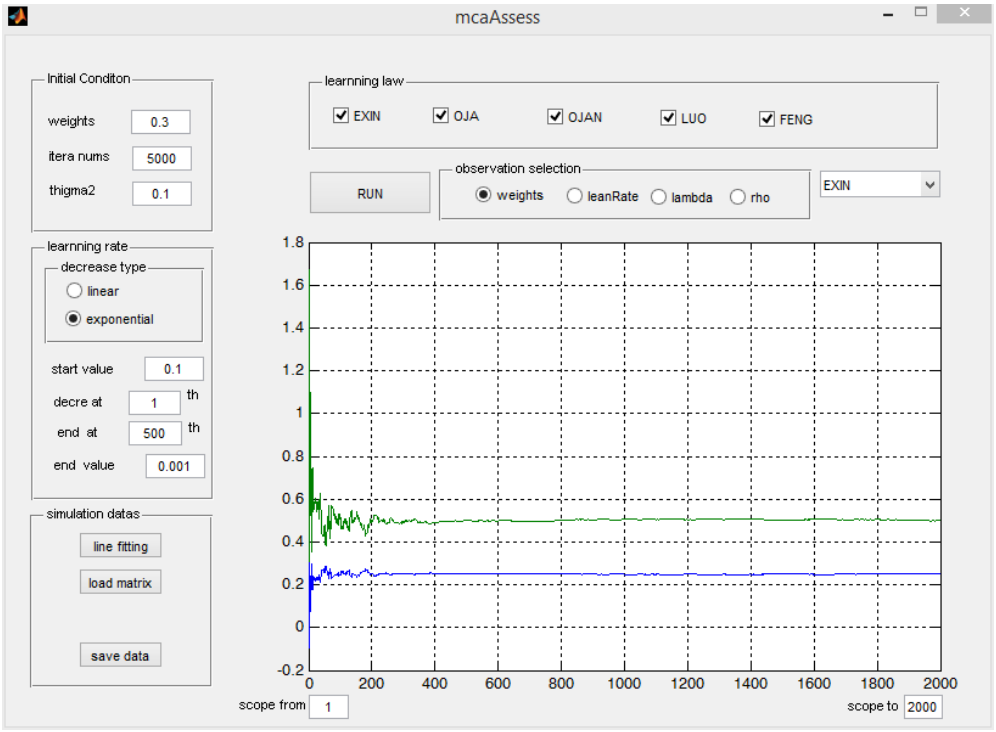

Fig C-2 Desktop of the MCA assessment software

Some examples of the results taken from the evaluation software are shown below from fig. C-3 to fig. C-6. It can be seen from those figures that both the advantage and drawbacks of different leaning law is clearly shown in the desktop.

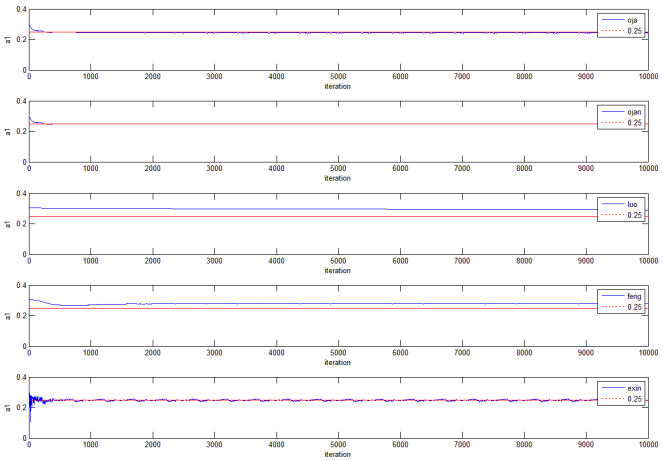

Fig C-3 One of the weights for different learning laws in the presence of white noise

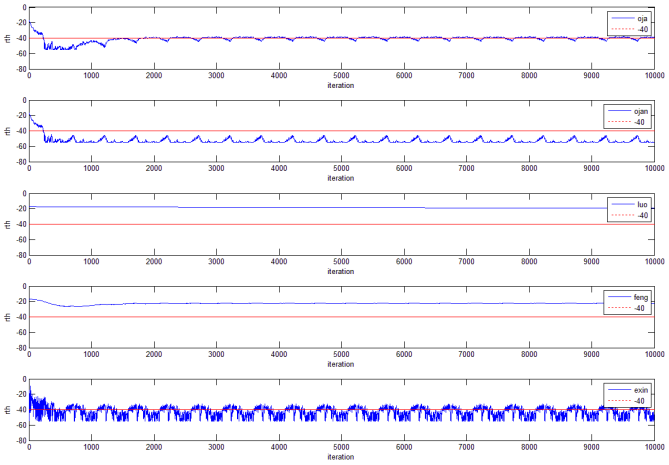

Fig C-4 *Rho* for different learning laws in the presence of white noise

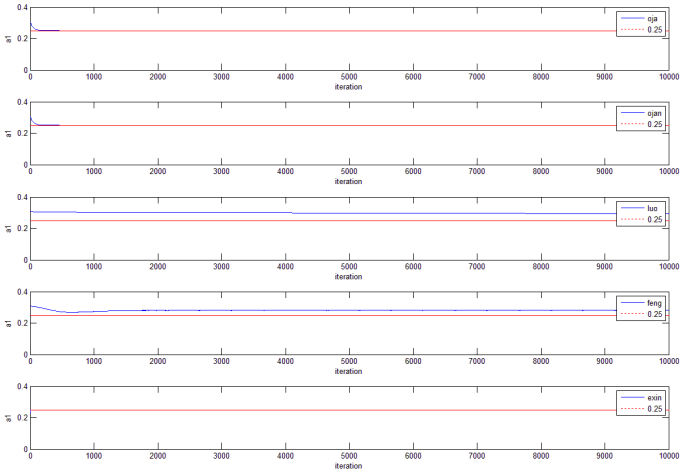

Fig C-5 One of the weight for different learning laws without noise

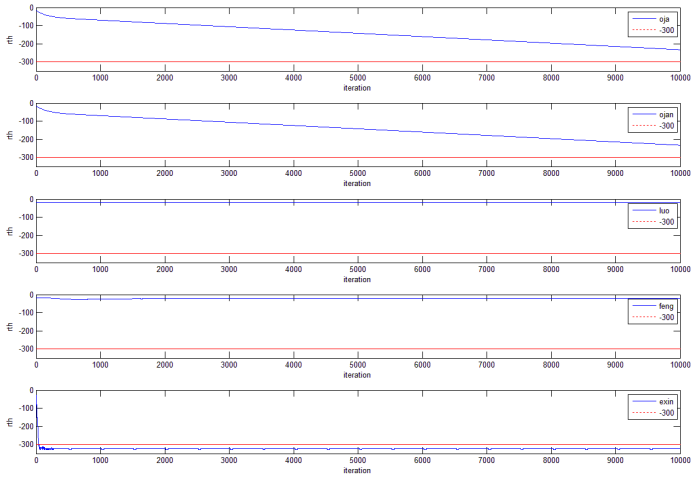

Fig C-6 Rho for different learning laws without noise

In the following sections, a brief summary of the convergence of MCA EXIN neuron is given as in [113]

2. Convergence and time constant of MCA EXIN

Assume that $\mathbf{R}_{xx}$ is well behaved: the observation follows from the well-known second-order ergodicity properties.

The weight $\mathbf{w}(t)$ can be expressed as a function of the orthogonal vectors

$$\mathbf{w}(t) = \sum_{i=1}^{n} f_i(t)\mathbf{z}_i \tag{C.7}$$

Replace it into (C.6), and recalling the orthogonality of the eigenvectors, yields

$$\frac{df_i(t)}{dt} = \|\mathbf{w}(t)\|_2^{-4}\left[\mathbf{w}^T(t)\mathbf{R}_{xx}\mathbf{w}(t)\, f_i(t) + -\mathbf{w}^T(t)\mathbf{w}(t)\lambda_i f_i(t)\right] \forall i = 1,2,...,n. \tag{C.8}$$

Define, $\forall i = 1,2,...,n-1.$

$$\varphi_i = \frac{f_i(t)}{f_n(t)} \tag{C.9}$$

Which gives

$$\frac{d\varphi_i(t)}{dt} = \frac{f_n(t)\dfrac{df_i(t)}{dt} - f_i(t)\dfrac{df_n(t)}{dt}}{\left(f_n(t)\right)^2} \overset{(c.7)}{=} \left\|\mathbf{w}(t)\right\|_2^{-2}\left(\lambda_n - \lambda_i\right)\varphi_i(t) \qquad (C.10)$$

Whose solution on $[0,\infty)$ is

$$\varphi_i(t) = \exp\left((\lambda_n - \lambda_i)\int_0^t \frac{d\nu}{\left\|\mathbf{w}(\nu)\right\|_2^2}\right) \quad \forall i = 1,2,...,n-1 \qquad (C.11)$$

If λ_n is single, then $\varphi_i(t) \overset{t\to\infty}{\to} 0$, then,

$$\lim_{t\to\infty} f_i(t) = 0, \qquad \forall i = 1,2,...,n-1 \qquad (C.12)$$

Which yields

$$\lim_{t\to\infty}\mathbf{w}(t) = \mathbf{w}(t_{ss}) = \lim_{t\to\infty} f_n(t)\mathbf{z}_n \qquad (C.13)$$

(C.13) shows $\mathbf{w}(t_{ss})$ is the eigenvector of $\mathbf{R}_{xx}$ which corresponding to minimum eigenvalue λ_n.

Multiplying (5.23) by $\mathbf{w}^T(t)$ on the left yields

$$\frac{d\left\|\mathbf{w}(t)\right\|_2^2}{dt} = \frac{2}{\left\|\mathbf{w}(t)\right\|_2^4}\left[-\left\|\mathbf{w}(t)\right\|_2^2\mathbf{w}^T(t)R\mathbf{w}(t) + \left(\mathbf{w}^T(t)R\mathbf{w}(t)\right)\left\|\mathbf{w}(t)\right\|_2^2\right] = 0 \qquad (C.14)$$

Then

$$\left\|\mathbf{w}(t)\right\|_2^2 = \left\|\mathbf{w}(0)\right\|_2^2, \quad t > 0 \qquad (C.15)$$

The symbol '=' in (C.15) is different from (5.23) is a consequence of the fact that the learning law represents only as a first-order approximation. The constancy of the weight modulus holds from (C.14), it then follows:

$$\lim_{t\to\infty} f_n(t) = \pm\left\|\mathbf{w}(0)\right\|_2 \qquad (C.16)$$

$$\lim_{t\to\infty}\mathbf{w}(t) = \mathbf{w}(t_{ss}) = \begin{cases} +\left\|\mathbf{w}(0)\right\|_2\mathbf{z}_n \ \forall\mathbf{w} / \mathbf{w}^T\mathbf{z}_n > 0 \\ -\left\|\mathbf{w}(0)\right\|_2\mathbf{z}_n \ \forall\mathbf{w} / \mathbf{w}^T\mathbf{z}_n < 0 \end{cases} \qquad (C.17)$$

(C.16) and (C.17) represent the convergence of the MC neurons.

From (C.11), in the approximation of modulus constancy (C.15),

$$\varphi_i(t) = \exp\left((\lambda_n - \lambda_i) \frac{t}{\|\mathbf{w}(0)\|_2^2} \right) \qquad \forall i = 1,2,..., n-1 \quad \text{(C.18)}$$

The time constant of the neuron is given by

$$\tau = \frac{\|\mathbf{w}(0)\|_2^2}{\lambda_n - \lambda_i} \quad \text{(C.19)}$$

(C.19) represents the approximate converging time for the the proposed estimator: it depends on the signal to noise ratio (SNR) and the modular of initial weights. As no assumptions on the SNR should be made, the time constant of the system can only be modified by the initial weights modulus.

(C.19) also shows the extra $\|\mathbf{w}(0)\|_2^2$ term make the MCA EXIN Pisarenko method possibly outperform some conventional gradient based method. The method has quicker convergence in the beginning with small modulus, as we will discuss later, this implies a higher variance in the first temporal part of the weight time evolution, but the fluctuation will decrease as the evolution continues.

3. Rayleigh Quotient and MCA EXIN learning law

The Rayleigh quotient (RQ) is the function which assigns to any nonzero complex vector **u** the scalar quantity

$$\mathrm{RQ}(\mathbf{u}) \equiv \mathrm{RQ}(\mathbf{u}, \mathbf{C}) \equiv \frac{\mathbf{u} * \mathbf{C}\mathbf{u}}{\mathbf{u} * \mathbf{u}} = \frac{\sum_j \sum_k c_{jk} u_j u_k}{\sum_i |u_i|^2} \quad \text{(C.20)}$$

Where $\mathbf{C} = \lfloor c_{jk} \rfloor$

The most relevant properties of the RQ are the following (for proofs see[129-132])

- Homogeneity:

$$\mathrm{RQ}(\alpha\mathbf{u}, \beta\mathbf{C}) = \beta \mathrm{RQ}(\mathbf{u}, \mathbf{C}) \quad \text{(C.21)}$$

- Translation invariance:

$$\mathrm{RQ}(\mathbf{u}, \mathbf{C} - \alpha\mathbf{I}) = \mathrm{RQ}(\mathbf{u}, \mathbf{C}) - \alpha \tag{C.22}$$

Boundedness: as **u** ranges over all nonzero vectors, RQ(**u**) fills a region in the complex plane which is called the field of values (also numerical range) of **C**. This region is closed, bounded and convex. If **C**=**C***(self adjoint matrix), the field of values is the real interval bounded by the extreme eigenvalues $[\lambda_{\min}, \lambda_{\max}]$.

- Orthogonality:

$$\mathbf{u} \perp (\mathbf{C} - \mathrm{RQ}(\mathbf{u})\mathbf{I})\mathbf{u} \tag{C.23}$$

- Minimal residual: scalar $\forall\, \mathbf{u} \neq 0 \wedge \forall$ scalar μ ,

$$\left\|(\mathbf{C} - \mathrm{RQ}(\mathbf{u})\mathbf{I})\right\| \leq \left\|(\mathbf{C} - \mu\mathbf{I})\mathbf{u}\right\| \tag{C.24}$$

- Let **C** be a real symmetric n-dimensional matrix with eigenvalues $\lambda_n \leq \lambda_{n-1} \leq \cdots \leq \lambda_1$ and corresponding unit eigenvectors $\mathbf{z}_1, \mathbf{z}_2, ..., \mathbf{z}_n$, Then

$$\lambda_1 = \max\ \mathrm{RQ}(\mathbf{u}, \mathbf{C}) \tag{C.25a}$$

$$\lambda_n = \min\ \mathrm{RQ}(\mathbf{u}, \mathbf{C}) \tag{C.25b}$$

More generally, the critical points and critical values of are the eigenvectors and eigenvalues for **C**.

The *Hessian* matrix of the RQ is given by

$$\mathbf{H}_r = \frac{2}{\|\mathbf{u}\|_2^2}\left(\mathbf{C} - \mathrm{grad}(\mathrm{RQ})\mathbf{u}^T - \mathbf{u}\,\mathrm{grad}(\mathrm{RQ})^T - \mathrm{RQ}\mathbf{I}\right) \tag{C.26}$$

Where **u** is real and

$$\mathrm{grad}(\mathrm{RQ}) = \frac{2}{\|\mathbf{u}\|_2^2}(\mathbf{C} - \mathrm{RQ}\mathbf{I})\mathbf{u} \tag{C.27}$$

It can be observed that, $\forall i = 1, 2, 3, ..., n$

$$H_{\mathrm{RQ}}(z_i) = \mathbf{C} - \lambda_i\mathbf{I} \tag{C.28}$$

Hence

$$\det[\mathbf{H}_r(\mathbf{z}_i)] = \det[\mathbf{C} - \lambda_i\mathbf{I}] = 0 \tag{C.29}$$

Which implies that $\mathbf{H}_{\mathrm{RQ}}(z_i)$ is singular $\forall z_i$. Furthermore

$$\mathbf{H}_{\mathrm{RQ}}(z_i)z_j = \begin{cases} 0 & i = j \\ (\lambda_j - \lambda_i)z_j & i \neq j \end{cases} \tag{C.30}$$

So $\mathbf{H}_r$, computed at the RQ critical points, has the same eigenvectors as **C**, but with different eigenvalues. $\mathbf{H}_r(\mathbf{u})$ is positive semidefinite only when $\mathbf{u}=\mathbf{z}_{\min}$.

Degeneracy proposition: The RQ critical points are degenerate because in these points the Hessian matrix is not invertible. Then the RQ is not a Morse function in every open subspace of the domain containing a critical point.

4. The Rayleigh Quotient Gradient Flow

Let $\phi: M \to \Re$ be a smooth function defined on a manifold M;

Let $D(\phi): M \to T*M$ denote the differential, i.e., the section of the cotangent bundle $T*M$ defined by

$$D(\phi(\mathbf{w})): T_{\mathbf{w}}M \to \Re, \quad \xi \to D(\phi(\mathbf{w}))\cdot\xi \equiv D(\phi)\big|_{\mathbf{w}}(\xi) \tag{C.31}$$

Where $D(\phi(\mathbf{w}))$ is the Fréchet derivative of ϕ at ***w***. To be able to define the gradient vector field of ϕ, a Riemannian metric $<,>_w$ on M must be specified. Then the consequent gradient $\operatorname{grad}\phi: M \to T*M$ is uniquely determined by the following two properties:

1) Tangency condition

$$\operatorname{grad}\phi(w) \in T_wM \quad \forall w \in M; \tag{C.32}$$

2) compatibility condition

$$D(\phi(w))\cdot\xi = \langle grad\,\phi(w), \xi\rangle \quad \forall \xi \in T_wM. \tag{C.33}$$

If $M = \Re^n$ is endowed with its standard Riemannian metric defined by $\langle\xi,\eta\rangle = \xi^T\eta \forall \xi,\eta \in \Re^n$, then the associated gradient vector is just

$$\nabla\phi(w) = \left(\frac{\partial\phi}{\partial w_1}(w), \frac{\partial\phi}{\partial w_2}(w), ..., \frac{\partial\phi}{\partial w_n}(w)\right)^T \tag{C.34}$$

If $Q(w): \Re^n \to \Re^{n\times n}$ is a symmetric matrix denoting a smooth map which represents the Riemannian metric, then

$$\operatorname{grad}\phi(w) = Q^{-1}(w)\nabla\phi(w) \tag{C.35}$$

Which shows the dependence of $\operatorname{grad}\phi(w)$ on the metric $Q(w)$.

Let $S^{n-1}=\{\mathbf{w}\in\Re^n \mid \|\mathbf{w}\|=1\}$ denote the unit sphere in $\Re^n$. Denote $\mathrm{RQ}(\mathbf{w},\mathbf{R}_{xx}):S^{n-1}\to\Re$ the restriction of the RQ of the autocorrelation matrix on the unit sphere.

The unite vector $\mathbf{w}\in S^{n-1}$, the Fréchet derivative of $\mathrm{RQ}(\mathbf{w},\mathbf{R}_{xx})$ is the linear functional $D(\mathrm{RQ}(\mathbf{w},\mathbf{R}_{xx}))|_{\mathbf{w}}:T_{\mathbf{w}}S^{n-1}\to\Re$ defined by

$$D(\mathrm{RQ}(\mathbf{w},\mathbf{R}_{xx}))|_{\mathbf{w}}(\xi)=2\langle\mathbf{R}_{xx}\mathbf{w},\xi\rangle=2\mathbf{w}^T\mathbf{R}_{xx}\xi \tag{C.36}$$

In order to define the gradient on the sphere, the standard Euclidean inner product on $T_{\mathbf{w}}S^{n-1}$ is chosen as Riemannian metric on S^{n-1}, i.e., up to a constant,

$$\langle\zeta,\eta\rangle\equiv 2\zeta^T\eta \quad \forall\xi,\eta\in T_{\mathbf{w}}S^{n-1} \tag{C.37}$$

The gradient $\nabla\mathrm{RQ}(\mathbf{w},\mathbf{R}_{xx})$ is then uniquely determined if it satisfies the tangency condition and the compatibility condition

$$D(RQ(\mathbf{w},\mathbf{R}_{xx}))|_{\mathbf{w}}(\xi)=\langle\nabla RQ(\mathbf{w},\mathbf{R}_{xx}),\xi\rangle=2\nabla RQ^T(\mathbf{w},\mathbf{R}_{xx})\xi \quad \forall\xi\in T_{\mathbf{w}}S^{n-1} \tag{C.38}$$

Which together with (C.35), implies

$$[\nabla RQ(\mathbf{w},\mathbf{R}_{xx})-\mathbf{R}_{xx}\mathbf{w}]^T=0 \tag{C.39}$$

From the definition of tangent space, it follows $\nabla RQ(\mathbf{w},\mathbf{R}_{xx})=\mathbf{R}_{xx}\mathbf{w}+\lambda\mathbf{w}$ with $\lambda=-\mathbf{w}^T\mathbf{R}\mathbf{w}$, so that $\mathbf{w}^T\nabla RQ(\mathbf{w},\mathbf{R}_{xx})=0$ to satisfy the tangency condition. Thus the gradient flow for the RQ on the unit sphere S^{n-1} is

$$\frac{d\mathbf{w}(\mathbf{t})}{dt}=-[\mathbf{R}_{xx}-RQ(\mathbf{w},\mathbf{R}_{xx})\mathbf{I}]\mathbf{w}(t) \tag{C.40}$$

The RQ gradient flow restricted to the unit sphere extends to a flow on $\Re^n-\{0\}$: Deriving the expression of the RQ with regard to $\mathbf{w}$ to gives the Fréchet derivative of $\mathrm{RQ}(\mathbf{w},\mathbf{R}_{xx}):\Re^n-\{0\}\to\Re$, which is

$$D(RQ(\mathbf{w},\mathbf{R}_{xx}))|_{\mathbf{w}}(\xi)=\frac{2}{\|\mathbf{w}\|_2^2}(\mathbf{R}_{xx}\mathbf{w}-RQ(\mathbf{w},\mathbf{R}_{xx})\mathbf{w})^T\xi \tag{C.41}$$

Define a Riemannian metric on each tangent space $T_{\mathbf{w}}(\Re^n-\{0\})$: as $\forall\xi,\eta\in T_{\mathbf{w}}(\Re^n-\{0\})$,

$$<< \xi, \eta >> \equiv 2\|\mathbf{w}\|_2^2 \xi^T \eta \Rightarrow \frac{d\mathbf{w}(t)}{dt} = -\frac{1}{\|\mathbf{w}\|_2^2} \nabla \phi(\mathbf{w}) \qquad \text{(C.42)}$$

Which is the ODE of the MCA EXIN neurons. Convergence and stability properties of gradient flows may depend on the choice of the Riemannian metric. In case of a nondegenerate critical point of ϕ, the local stability properties of the gradient flow around that point do not change with the Riemannian metric. However, in case of a degenerate critical point, the qualitative picture of the local phase portrait of the gradient around that point may well change with the Riemannian metric [130], [133].

As seen in the Degeneracy proposition [113], the RQ critical points are degenerate. As a consequence, the phase portrait of the gradient flow has only degenerate straight lines in the direction of the RQ eigenvectors, i.e., the critical points are not isolated. This fundamental observation, together with the above analysis, justifies the creation of MCA neurons.

APPENDIX D GENERALIZATION OF THE LINEAR REGRESSION PROBLEMS

If the vector $\mathbf{b} = [b_1 \ldots b_j \ldots b_m]^T \in \mathbb{R}^m$ is considered as well as the matrix $A \in \mathbb{R}^{mxn}$ composed of *m* row vectors $\mathbf{a}_j^T$, then finding the weight vector **x** (the problem of linear parameter estimation) is generally equivalent to solving the following overdetermined set of linear equations, on the basis of the training set made up of the expanded matrix [A;b]:

$$\mathbf{Ax} \oplus \mathbf{b} \tag{D.1}$$

Generally, $\mathbf{A} \in \mathbb{R}^{mxn}$ is called data matrix, and $\mathbf{b} \in \mathbb{R}^m$ is called observation vector. Several different problems require finding the solution, according to the error consideration, there are generally three types of approaches to solve this equation [2,92]:

1. Ordinary Least Squares (OLS)

According to the classical ordinary least squares (OLS) approach, errors are implicitly assumed to be confined to the observation vector. The least-square solution is the one minimizing

$$\min_{\mathbf{b}' \in \Re^m} \left\| \mathbf{b} - \mathbf{b}' \right\|_2 \text{ with the constraint } \mathbf{b}' \in R(\mathbf{A}) \tag{D.2}$$

Where $R(\mathbf{A})$ is the column space of **A**. When a minimum of $\mathbf{b}'$ is found, every vector satisfying

$$\mathbf{Ax}' = \mathbf{b}' \tag{D.3}$$

is then called the OLS solution. It corresponds to the point minimizing the following cost function:

$$\mathrm{E}_{OLS}(x) = (\mathbf{Ax} - \mathbf{b})^T (\mathbf{Ax} - \mathbf{b}) \tag{D.4}$$

2. Data Least Squares (DLS)

The opposite case is the data least squares (DLS) problem, because the error is assumed to lie only in the data matrix **A**. The data least-square solution is the one minimizing $\min_{\mathbf{A}' \in \Re^{m*n}} \left\| \mathbf{A} - \mathbf{A}'' \right\|_F$ with constraint $\mathbf{b} \in R(\mathbf{A}'')$

where $\|\ldots\|_F$ is the Frobenius norm. Once a minimum $\mathbf{A}''$ is found, every $\mathbf{x}''$satisfying

$$\mathbf{A}^{''}\mathbf{x}^{''} = \mathbf{b} \tag{D.5}$$

is called the DLS solution. It is proved that it corresponds to the minimization of the cost function

$$\mathrm{E}_{DLS}(x) = \frac{(A\mathbf{x}-\mathbf{b})^T(A\mathbf{x}-\mathbf{b})}{\mathbf{x}^T\mathbf{x}} \tag{D.6}$$

3. Total Least Squares (TLS)

The total least squares (TLS) method is a technique devised to make up for the errors in both the data matrix and observation vector. The least-square solution is the one minimizing

$$\min_{[\hat{A};\hat{\mathbf{b}}]\in\Re^{m*(n+1)}} \left\| [\mathbf{A};\mathbf{b}] - \left[\hat{\mathbf{A}};\hat{\mathbf{b}}\right] \right\|_F \text{ with constraint } \hat{\mathbf{b}} \in R(\hat{\mathbf{A}}) \tag{D.7}$$

When a minimum of $\left[\hat{\mathbf{A}};\hat{\mathbf{b}}\right]$ is found, every $\hat{\mathbf{x}}$ satisfying

$$\hat{\mathbf{A}}\hat{\mathbf{x}} = \hat{\mathbf{b}} \tag{D.8}$$

is called a TLS solution. It minimizes the sum of orthogonal squared distances (weighted residues squared sum):

$$\mathrm{E}_{TLS}(x) = \frac{(\mathbf{A}\mathbf{x}-\mathbf{b})^T(\mathbf{A}\mathbf{x}-\mathbf{b})}{1+\mathbf{x}^T\mathbf{x}} = \frac{\left\|[\mathbf{A};\mathbf{b}]\left[\mathbf{x}^T;-1\right]\right\|_2^2}{\left\|\left[x^T;-1\right]\right\|_2^2} \tag{D.9}$$

APPENDIX E CONVERGENCE BOUND OF THE ADAPTIVE LEARNING RATE

Before studying the upper bound of the learning rate, consider again the learning process (5.20) in the deterministic continuous time (DCT) system [115], and rewrite the learning process of EXIN neurons in the DDT system[116,117].

$$\mathbf{w}(k+1) = \mathbf{w}(k) - \frac{\alpha(k)}{\|\mathbf{w}(k)\|_2^2}[\mathbf{R}_{xx}\mathbf{w}(k) - r(k)\mathbf{w}(k)] = G(\boldsymbol{w}(k)) \qquad \text{(E.1)}$$

Where $\mathrm{r(k)} = \frac{\mathbf{w}^T(\mathbf{k})\mathbf{R}_{xx}\mathbf{w}(\mathbf{k})}{\mathbf{w}^T(\mathbf{k})\mathbf{w}(\mathbf{k})}$ is the Rayleigh quotient at the k^{th} iteration, and it holds that $\lambda_M \leq \mathrm{r(k)} \leq \lambda_1$ from the properties of the RQ. To avoid confusion, the time index term *t* is replaced by *k* in the following DDT analysis.

It should be noted that (E.1) can also be obtained as the numerical integration of (5.20) via Euler's method with step size α, however, in (E.1) the discrete learning process is preserved appropriately.

At the equilibrium of MCA EXIN, $\{\mathbf{z}_1, \mathbf{z}_2, \ldots, \mathbf{z}_M\}$, it follows from (E.1), and without loss of generality, we simplify the term $\mathbf{w}(\mathbf{t})$ to $\mathbf{w}$,

$$\frac{\partial G}{\partial w} = \boldsymbol{I} - \alpha\boldsymbol{H} \quad = \boldsymbol{I} - \frac{\alpha}{\|\mathbf{w}\|^2}\left(r\boldsymbol{I} - 2\frac{r\mathbf{w}\mathbf{w}^{\boldsymbol{T}}}{\|\mathbf{w}\|_2^2} - \frac{\mathbf{w}^{\boldsymbol{T}}r\mathbf{w}\mathbf{I} + 2\mathbf{w}\mathbf{w}^{\boldsymbol{T}}\boldsymbol{r}}{\|\mathbf{w}\|_2^2} + 4\frac{(\mathbf{w}^{\boldsymbol{T}}r\mathbf{w})\mathbf{w}\mathbf{w}^{\boldsymbol{T}}}{\|\mathbf{w}\|_2^4}\right)$$

$$= \boldsymbol{I} - 2\alpha\frac{1}{\|\mathbf{w}\|_2^2}(\mathbf{R} - \nabla(r)\mathbf{w}^{\boldsymbol{T}} - \mathbf{w}\,\nabla(r)^T - r\boldsymbol{I}) \qquad \text{(E.2)}$$

Where $\boldsymbol{H}$ is the Hessian matrix of the RQ, and

$$\nabla(r) = \frac{2}{\|\mathbf{w}\|_2^2}(\mathbf{R}_{xx} - r\mathbf{I})\mathbf{w} \qquad \text{(E.3)}$$

is the gradient flow of RQ, being $\mathbf{R}_{xx}$ the autocorrelation matrix.

It is easy to see that (E.2) has the same eigenvectors as $\mathbf{R}_{xx}$, for the equilibrium $\mathbf{w}=\mathbf{z}_j$, and recalling the properties of RQ, it follows

$$\left.\frac{\partial G}{\partial w}\right|_{z_j} = I - 2\alpha\frac{1}{\|\mathbf{w}\|_2^2}\left(\mathbf{R}_{xx} - \lambda_j\boldsymbol{I}\right) = \boldsymbol{J}_j \qquad \text{(E.4)}$$

The term $\frac{1}{\|\mathbf{w}\|_2^2}$ acts as a scaling term to the learning rate.

Now the stability at point $\boldsymbol{z}_j(\lambda_j)$ will depend on the spectral analysis of $\boldsymbol{J}_j$, whose eigenvalues are given by the eigenvalues of $\mathbf{R}_{xx}$, λ_i, following (E.4),

$$\begin{cases} \lambda & = 1 - \frac{2\alpha}{\|\mathbf{w}\|_2^2}(\lambda_i - \lambda_j), & i \neq j \quad a) \\ \lambda & = 1, & i = j \quad b) \end{cases} \tag{E.5}$$

From the Lyapunov theory, an asymptotic stability at points $\boldsymbol{z}_j(\lambda_j)$ sufficient condition is $|\lambda| < 1, \forall \lambda \; of \; \boldsymbol{J_j}$. It should be noted from (E.5b) that we cannot draw any conclusions of the global stability because one eigenvalue lies on the unit circle for $i = j$, the equilibrium can be either stable or unstable, however (E.5a) provide the necessary information about the range where the learning rate does not diverge the original system. The verification of the global convergence of MCA EXIN neurons, can be found in appendix D.

For this purpose, the cases *j=M* and $j \neq M$ should be distinguished, where *j=M* corresponding to the eigenvector associated with the minimum eigenvalueλ_M.

Case $j \neq M$, considering the eigenvalues for $i \neq j$ in (E.5a),

$$\left|1 - \frac{2\alpha}{\|\mathbf{w}\|_2^2}(\lambda_i - \lambda_j)\right| < 1 \Leftrightarrow -1 < 1 - \frac{2\alpha}{\|\mathbf{w}\|_2^2}(\lambda_i - \lambda_j) < 1$$

$$\Leftrightarrow (\lambda_i > \lambda_j) \cap (\tfrac{\alpha}{\|\mathbf{w}\|_2^2} < \tfrac{1}{\lambda_i - \lambda_j}) \tag{E.6}$$

It is obviously from the definition that for i>j, $\lambda_i \leq \lambda_j$, which is in contradiction with (E.6). Therefore points $j \neq M$ are instable irrelevant to the choice of α, which is in accordance with the convergence analysis in appendix D.

Case *j=M*, and considering$i \neq j$, from (E.5a)

$$\left|1 - \frac{2\alpha}{\|\mathbf{w}\|_2^2}(\lambda_i - \lambda_M)\right| < 1 \Leftrightarrow -1 < 1 - \frac{2\alpha}{\|\mathbf{w}\|_2^2}(\lambda_i - \lambda_M) < 1$$

$$\Leftrightarrow (\lambda_i > \lambda_M) \cap (\tfrac{\alpha}{\|\mathbf{w}\|_2^2} < \tfrac{1}{\lambda_i - \lambda_M}) \tag{E.7}$$

Note that $\frac{1}{\lambda_i - \lambda_M} \geq \frac{1}{\lambda_1 - \lambda_M}$, so the maximal learning rate which does not diverge the original system is given as,

$$\alpha < \alpha_{max} = \frac{\|\mathbf{w}\|_2^2}{\lambda_1 - \lambda_M} \tag{E.8}$$

BIBLIOGRAPHY

[1] Vas P. Sensorless vector and direct torque control[M]. Oxford Univ. Press, 1998.

[2] Cirrincione M, Pucci M, Vitale G. Power Converters and AC Electrical Drives with Linear Neural Networks[M]. CRC Press, 2012.

[3] Asher, G.M., "Sensorless estimation for vector controlled induction motor drives," *Vector Control Revisited (Digest No. 1998/199), IEE Colloquium on* , vol., no., pp.6/1,6/5, 23 Feb 1998

[4] Holtz J. Sensorless control of induction motor drives[J]. Proceedings of the IEEE, 2002, 90(8): 1359-1394.

[5] Lascu C, Boldea I, Blaabjerg F. Direct torque control of sensorless induction motor drives: a sliding-mode approach[J]. Industry Applications, IEEE Transactions on, 2004, 40(2): 582-590.

[6] Blasco-Gimenez R, Asher G M, Sumner M, et al. Dynamic performance limitations for MRAS based sensorless induction motor drives. Part 1: Stability analysis for the closed loop drive[J]. IEE Proceedings-Electric Power Applications, 1996, 143(2): 113-122.

[7] Ghanes M, Zheng G. On sensorless induction motor drives: Sliding-mode observer and output feedback controller[J]. Industrial Electronics, IEEE Transactions on, 2009, 56(9): 3404-3413.

[8] Kim S H, Park T S, Yoo J Y, et al. Speed-sensorless vector control of an induction motor using neural network speed estimation[J]. Industrial Electronics, IEEE Transactions on, 2001, 48(3): 609-614.

[9] Tajima H, Guidi G, Umida H. Consideration about problems and solutions of speed estimation method and parameter tuning for speed-sensorless vector control of induction motor drives[J]. Industry Applications, IEEE Transactions on, 2002, 38(5): 1282-1289.

[10] Rashed M, Stronach A F. A stable back-EMF MRAS-based sensorless low-speed induction motor drive insensitive to stator resistance variation[J]. IEE Proceedings-Electric Power Applications, 2004, 151(6): 685-693.

[11] Cirrincione M, Pucci M. An MRAS-based sensorless high-performance induction motor drive with a predictive adaptive model[J]. Industrial Electronics, IEEE Transactions on, 2005, 52(2): 532-551.

[12] Toliyat H A, Levi E, Raina M. A review of RFO induction motor parameter estimation techniques[J]. Energy Conversion, IEEE Transactions on, 2003, 18(2): 271-283.

[13] Hu, J.; Wu, B., "New integration algorithms for estimating motor flux over a wide speed range," *Power Electronics Specialists Conference, 1997. PESC '97 Record., 28th Annual IEEE* , vol.2, no., pp.1075,1081 vol.2, 22-27 Jun 1997

[14] Hurst, K.D.; Habetler, T.G.; Griva, G.; Profumo, F., "Zero-speed tacholess IM torque control: simply a matter of stator voltage integration," *Industry Applications, IEEE Transactions on* , vol.34, no.4, pp.790,795, Jul/Aug 1998

[15] Holtz, J.; Juntao Quan, "Sensorless vector control of induction motors at very low speed using a nonlinear inverter model and parameter identification," *Industry Applications, IEEE Transactions on* , vol.38, no.4, pp.1087,1095, Jul/Aug 2002

[16] Holtz, J.; Juntao Quan, "Drift- and parameter-compensated flux estimator for persistent zero-stator-frequency operation of sensorless-controlled induction motors,"*Industry Applications, IEEE Transactions on* , vol.39, no.4, pp.1052,1060, July-Aug. 2003

[17] Schauder, C., "Adaptive speed identification for vector control of induction motors without rotational transducers," *Industry Applications, IEEE Transactions on* , vol.28, no.5, pp.1054,1061, Sep/Oct 1992

[18] Orlowska-Kowalska, T.; Dybkowski, M., "Stator-Current-Based MRAS Estimator for a Wide Range Speed-Sensorless Induction-Motor Drive," *Industrial Electronics, IEEE Transactions on* , vol.57, no.4, pp.1296,1308, April 2010

[19] Dybkowski, M.; Orlowska-Kowalska, T., "Self-tuning adaptive sensorless induction motor drive with the stator current-based MRAS speed estimator," *EUROCON 2009, EUROCON '09. IEEE* , vol., no., pp.804,810, 18-23 May 2009

[20] Castaldi, P.; Tilli, A, "Parameter estimation of induction motor at standstill with magnetic flux monitoring," *Control Systems Technology, IEEE Transactions on* , vol.13, no.3, pp.386,400, May 2005

[21] Comanescu, Mihai; Batzel, T., "Sliding Mode MRAS Speed Estimators for Sensorless Control of Induction Machine under Improper Rotor Time Constant," *Industrial Electronics, 2007. ISIE 2007. IEEE International Symposium on* , vol., no., pp.2226,2231, 4-7 June 2007

[22] M. Cirrincione , M. Pucci , G. Cirrincione , G. A. Capolino, "A New Adaptive Integration Methodology for Estimating Flux in Induction Machine Drives ", IEEE Transactions on Power Electronics, vol.19, n °1, January 2004, pp.25-34

[23] Cirrincione, M.; Pucci, M., "An MRAS based speed estimation method with a linear neuron for high performance induction motor drives and its experimentation," *Electric Machines and Drives Conference, 2003. IEMDC'03. IEEE International* , vol.1, no., pp.617,623 vol.1, 1-4 June 2003

[24] Kubota, K.; Matsuse, K.; Nakano, T., "DSP-based speed adaptive flux observer of induction motor," *Industry Applications, IEEE Transactions on* , vol.29, no.2, pp.344,348, Mar/Apr 1993

[25] Kyo-Beum Lee; Blaabjerg, F., "Reduced-order extended luenberger observer based sensorless vector control driven by matrix converter with nonlinearity compensation,"*Industrial Electronics, IEEE Transactions on* , vol.53, no.1, pp.66,75, Feb. 2006

[26] Benchaib, A; Rachid, A; Audrezet, E.; Tadjine, M., "Real-time sliding-mode observer and control of an induction motor," *Industrial Electronics, IEEE Transactions on* , vol.46, no.1, pp.128,138, Feb 1999

[27] Kim, Y.-R.; Seung-Ki Sul; Park, M.-H., "Speed sensorless vector control of induction motor using extended Kalman filter," *Industry Applications, IEEE Transactions on* , vol.30, no.5, pp.1225,1233, Sep/Oct 1994

[28] Pucci, M.; Serporta, C., "Finite-Element Analysis of Rotor Slotting Saliency in Induction Motors for Sensorless Control," *Magnetics, IEEE Transactions on* , vol.46, no.2, pp.650,653, Feb. 2010

[29] Teske, N.; Asher, G.M.; Sumner, M.; Bradley, K.J., "Analysis and suppression of high-frequency inverter modulation in sensorless position-controlled induction machine drives," *Industry Applications, IEEE Transactions on* , vol.39, no.1, pp.10,18, Jan/Feb 2003

[30] Holtz, J., "Sensorless position control of induction motors-an emerging technology," *Industrial Electronics, IEEE Transactions on* , vol.45, no.6, pp.840,851, Dec 1998

[31] Caruana, C.; Asher, G.M.; Sumner, M., "Performance of HF signal injection techniques for zero-low-frequency vector control of induction Machines under sensorless conditions," *Industrial Electronics, IEEE Transactions on* , vol.53, no.1, pp.225,238, Feb. 2006

[32] Jansen, P.L.; Lorenz, R.D., "Transducerless field orientation concepts employing saturation-induced saliencies in induction machines," *Industry Applications Conference, 1995. Thirtieth IAS Annual Meeting, IAS '95., Conference Record of the 1995 IEEE* , vol.1, no., pp.174,181 vol.1, 8-12 Oct 1995

[33] Teske, N.; Asher, G.M.; Sumner, M.; Bradley, K.J., "Encoderless position estimation for symmetric cage induction machines under loaded conditions," *Industry Applications, IEEE Transactions on* , vol.37, no.6, pp.1793,1800, Nov/Dec 2001

[34] Briz, F.; Degner, M.W.; Diez, A; Lorenz, R.D., "Measuring, modeling, and decoupling of saturation-induced saliencies in carrier-signal injection-based sensorless AC drives," *Industry Applications, IEEE Transactions on* , vol.37, no.5, pp.1356,1364, Sep/Oct 2001

[35] J. Holtz, "Sensorless control of induction machines—With or without signal injection?," IEEE Trans. Ind. Electron., vol. 53, no. 1, pp. 7–30, Feb. 2006.

[36] Staines, C.S.; Caruana, C.; Asher, G.M.; Sumner, M., "Sensorless control of induction Machines at zero and low frequency using zero sequence currents," *Industrial Electronics, IEEE Transactions on* , vol.53, no.1, pp.195,206, Feb. 2006

[37] Raute, R.; Caruana, C.; Staines, C.S.; Cilia, J.; Sumner, M.; Asher, G.M., "Sensorless Control of Induction Machines at Low and Zero Speed by Using PWM Harmonics for Rotor-Bar Slotting Detection," *Industry Applications, IEEE Transactions on* , vol.46, no.5, pp.1989,1998, Sept.-Oct. 2010

[38] Ishida, M.; Iwata, K., "A New Slip Frequncy Detector of an Induction Motor Utilizing Rotor Slot Harmonics," *Industry Applications, IEEE Transactions on* , vol.IA-20, no.3, pp.575,582, May 1984

[39]Williams, B.W.; Goodfellow, J.K.; Green, T.C., "`Sensorless' speed measurement of inverter driven squirrel cage induction motors," Power Electronics and Variable-Speed Drives, 1991., Fourth International Conference on , vol., no., pp.297,300, 17-19 Jul 1990

[40] Nandi, S.; Toliyat, H.A; Xiaodong Li, "Condition monitoring and fault diagnosis of electrical motors-a review," *Energy Conversion, IEEE Transactions on* , vol.20, no.4, pp.719,729, Dec. 2005

[41] M. Cirrincione , M. Pucci , G. Cirrincione , A. Miraoui, "Space-Vector State Model of Induction Machines Including Rotor Slotting Effects: Towards a New Category of Observers", IEEE Transactions on Industry Applications, Vol. 44, n.6, November/December 2008.

[42] Cameron, J.R.; Thomson, W.T.; Dow, AB., "Vibration and current monitoring for detecting airgap eccentricity in large induction motors," *Electric Power Applications, IEE Proceedings B* , vol.133, no.3, pp.155,163, May 1986

[43] Kron, Gabriel. Equivalent circuits of electric machinery. Dover Publications, 1967.

[44] S. Nandi, S. Amhed, H. Toliyat, "Detection of Rotor Slot and Other eccentricity Related Harmonics in a Three Phase Induction Motor with Different Cages", IEEE Transactions on Energy Conversion,. vol. 16, n.3, September 2001, pp. 253-260.

[45] Ferrah, A; Hogben-Laing, P.J.; Bradley, K.J.; Asher, G.M.; Woolfson, M.S., "The effect of rotor design on sensorless speed estimation using rotor slot harmonics identified by adaptive digital filtering using the maximum likelihood approach," Industry Applications Conference, 1997. Thirty-Second IAS Annual Meeting, IAS '97., Conference Record of the 1997 IEEE , vol.1, no., pp.128,135 vol.1, 5-9 Oct 1997

[46] Joksimovic, G.M.; Riger, J.; Wolbank, T.M.; Peric, N.; Vasak, M., "Stator-Current Spectrum Signature of Healthy Cage Rotor Induction Machines," *Industrial Electronics, IEEE Transactions on* , vol.60, no.9, pp.4025,4033, Sept. 2013

[47] T. Jokinen and V. Hrabovcova, Design of Rotating Electrical Machines.Hoboken, NJ: Wiley, 2009.

[48] Joksimovic, G.; Riger, J.; Wolbank, T.; Peric, N.; Vasak, M., "Stator line current spectrum content of a healthy cage rotor induction machine," Diagnostics for Electric Machines, Power Electronics & Drives (SDEMPED), 2011 IEEE International Symposium on , vol., no., pp.113,118, 5-8 Sept. 2011

[49] P. Vas, *Parameter Estimation, Condition Monitoring, and Diagnosis of Electrical Machines*. Oxford, U.K.: Clarendon, 1993.

[50] M. M. Liwschitz, "Field harmonics in induction motors," *Trans. Amer.Inst. Elect. Eng.*, vol. 61, pp. 797–803, Nov. 1942.

[51] B. Heller and V. Hamata, *Harmonic Field Effects in Induction Machine*.New York: Elsevier, 1977.

[52] Fitzgerald, A. E., Charles Kingsley, and Stephen Umans. Electric Machinery, 6/e. Ed, 1983.

[53] Ferrah, A.; Bradley, K.J.; Asher, G.M., "An FFT-based novel approach to noninvasive speed measurement in induction motor drives," Instrumentation and Measurement, IEEE Transactions on , vol.41, no.6, pp.797,802, Dec 1992

[54] A. S. Spanias, "Block time and frequency domain modified covariance algorithms for spectral analysis," *IEEE Trans. Acoust., Speech, Signal Processing*, vol. 41, pp. 3138–3152, Nov. 1993.

[55] F. B. Hildebrand, *Advanced Calculus for Applications.* Englewood Cliffs, NJ: Prentice-Hall, 1963.

[56] Hurst, K.D.; Habetler, T.G., "Sensorless speed measurement using current harmonic spectral estimation in induction machine drives," Power Electronics, IEEE Transactions on , vol.11, no.1, pp.66,73, Jan 1996

[57] D. N. Swingler, "A modified Burg algorithm for maximum entropy spectral analysis," *Proc. IEEE,* vol. 67, pp. 1368–1369, Sept. 1979.

[58] Aiello, M.; Cataliotti, A.; Nuccio, S., "An induction motor speed measurement method based on current harmonic analysis with the chirp-Z transform," Instrumentation and Measurement, IEEE Transactions on , vol.54, no.5, pp.1811,1819, Oct. 2005

[59] Ferrah, A.; Bradley, K.J.; Hogben-Laing, P.J.; Woolfson, Malcolm S.; Asher, G.M.; Sumner, M.; Cilia, J.; Shuli, J., "A speed identifier for induction motor drives using real-time adaptive digital filtering," Industry Applications, IEEE Transactions on , vol.34, no.1, pp.156,162, Jan/Feb 1998

[60] Yamamoto, K.; Iimori, K.; Morita, H., "A study of digital filter for rotor speed detection with slot harmonic current for induction motor," TENCON 2010 - 2010 IEEE Region 10 Conference , vol., no., pp.2137,2142, 21-24 Nov. 2010

[61] Zhi Gao; Turner, L.; Colby, R.S.; Leprettre, B., "A Frequency Demodulation Approach to Induction Motor Speed Detection," Industry Applications, IEEE Transactions on , vol.47, no.4, pp.1632,1642, July-Aug. 2011

[62] Vas, Peter. *Electrical machines and drives: a space-vector theory approach*. Vol. 25. Oxford University Press, USA, 1992.

[63] Vas, P., and W. Drury. "Electrical machines and drives: present and future."*Electrotechnical Conference, 1996. MELECON'96., 8th Mediterranean*. Vol. 1. IEEE, 1996.

[64] Bose, Bimal K. "Scalar decoupled control of induction motor." *Industry Applications, IEEE Transactions on* 1 (1984): 216-225.

[65] *K. Rajashekara, A. Kawamura, K. Matsuse, "Sensorless Control of AC Motor Drives", IEEE Press, 1996.*

[66] Bodson, Marc, John Chiasson, and Robert Novotnak. "High-performance induction motor control via input-output linearization." *Control Systems, IEEE*14.4 (1994): 25-33.

[67] Vas, P., and W. Drury. "Electrical machines and drives: present and future."*Electrotechnical Conference, 1996. MELECON'96., 8th Mediterranean*. Vol. 1. IEEE, 1996.

[68] Boys, J. T., and S. J. Walton. “Scalar control: an alternative AC drive philosophy.” *Electric Power Applications, IEE Proceedings B* 135.3 (1988): 151-158.

[69] Wang, Chun-Chieh, and Chih-Hsing Fang. “Sensorless scalar-controlled induction motor drives with modified flux observer.” *Energy Conversion, IEEE Transactions on* 18.2 (2003): 181-186.

[70] Leonhard, Werner. *Control of electrical drives*. Springer, 2001.

[71] Lipo, Thomas A. *Vector control and dynamics of AC drives*. Vol. 41. Oxford University Press, 1996.

[72] Suetake, M.; da Silva, I.N.; Goedtel, A., "Embedded DSP-Based Compact Fuzzy System and Its Application for Induction-Motor V/f Speed Control," Industrial Electronics, IEEE Transactions on , vol.58, no.3, pp.750,760, March 2011

[73] Smith, Andrew, et al. “Improved method for the scalar control of induction motor drives.” *IET Electric Power Applications* 7.6 (2013): 487-498.

[74] D’Azzo J J, Houpis C D. Linear control system analysis and design: conventional and modern[M]. McGraw-Hill Higher Education, 1995.

[75] Ogata K, Yang Y. Modern control engineering[J]. 1970.

[76] Blasco-Gimenez, R.; Asher, G.M.; Sumner, M.; Bradley, K.J., “Performance of FFT-rotor slot harmonic speed detector for sensorless induction motor drives,” Electric Power Applications, IEE Proceedings - , vol.143, no.3, pp.258,268, May 1996

[77] Hurst, K.D.; Habetler, T.G., “A comparison of spectrum estimation techniques for sensorless speed detection in induction machines,” Industry Applications Conference, 1995. Thirtieth IAS Annual Meeting, IAS ’95., Conference Record of the 1995 IEEE , vol.1, no., pp.553,559 vol.1, 8-12 Oct 1995

[78] Nishibata, K.; Ishida, M.; Doki, S.; Masuzawa, T.; Fujitsuna, M., “Speed Estimation Method utilizing Rotor Slot Harmonics Detected from Line Current for Speed Sensorless Drive of Ultra High Speed Induction Machine,” Industrial Technology, 2006. ICIT 2006. IEEE International Conference on , vol., no., pp.1591,1596, 15-17 Dec. 2006

[79] Keysan, O.; Ertan, H.B., “Real-Time Speed and Position Estimation Using Rotor Slot Harmonics,” Industrial Informatics, IEEE Transactions on , vol.9, no.2, pp.899,908, May 2013

[80] Zinger, D.; Profumo, F.; Lipo, T.A.; Novotny, D.W., "A direct field oriented controller for induction motor drives using tapped stator windings," Power Electronics Specialists Conference, 1988. PESC '88 Record., 19th Annual IEEE , vol., no., pp.855,861 vol.2, 11-14 April 1988

[81] Egan, William F. Phase-lock basics. Wiley. Com, 2007.

[82] Guan-Chyun Hsieh; Hung, J.C., "Phase-locked loop techniques. A survey," Industrial Electronics, IEEE Transactions on , vol.43, no.6, pp.609,615, Dec. 1996

[83] Kai Sun; Qiang Zhou; Yilu Liu, "A Phase Locked Loop-Based Approach to Real-Time Modal Analysis on Synchrophasor Measurements," Smart Grid, IEEE Transactions on , vol.5, no.1, pp.260,269, Jan. 2014

[84] Ama, N.R.N.; Martinz, F.O.; Matakas, L.; Kassab, F., "Phase-Locked Loop Based on Selective Harmonics Elimination for Utility Applications," Power Electronics, IEEE Transactions on , vol.28, no.1, pp.144,153, Jan. 2013

[85] Singh B, Arya S R. Implementation of Single-Phase Enhanced Phase-Locked Loop-Based Control Algorithm for Three-Phase DSTATCOM[J]. Power Delivery, IEEE Transactions on, 2013, 28(3): 1516-1524.

[86] Nascimento P S B, de Souza H E P, Neves F A S, et al. FPGA implementation of the generalized delayed signal cancelation—Phase locked loop method for detecting harmonic sequence components in three-phase signals[J]. Industrial Electronics, IEEE Transactions on, 2013, 60(2): 645-658.

[87] Chung S K. Phase-locked loop for grid-connected three-phase power conversion systems[C]//Electric Power Applications, IEE Proceedings-. IET, 2000, 147(3): 213-219.

[88] Rodr ǵuez P, Luna A, Candela I, et al. Multiresonant frequency-locked loop for grid synchronization of power converters under distorted grid conditions[J]. Industrial Electronics, IEEE Transactions on, 2011, 58(1): 127-138.

[89] B. Widrow, S. D. Stearns, Adaptive Signal Processing, Signal Processing Series, Prentice-Hall, Englewood Cliffs, NJ, 1985.

[90] Cirrincione M, Pucci M, Vitale G. A single-phase DG generation unit with shunt active power filter capability by adaptive neural filtering[J]. Industrial Electronics, IEEE Transactions on, 2008, 55(5): 2093-2110.

[91] Cirrincione, M., Pucci, M., Vitale, G., & Miraoui, A. (2009). Current harmonic compensation by a single-phase shunt active power filter controlled by adaptive neural filtering. Industrial Electronics, IEEE Transactions on, 56(8), 3128-3143.

[92] G. Cirrincione, M. Cirrincione, Neural Based Orthogonal Data Fitting: The EXIN Neural Networks, Series: Adaptive and Learning Systems for Signal Processing, Communications and Control, Wiley & Sons, New York, 255pp., November 2010.

[93] S. Van Huffel and J. Vandewalle, Analysis of the Total Least Squares Problem and Its Use in Parameter Estimation. Leuven, Belgium: SIAM, 1987.

[94] Rodríguez, P.; Luna, A.; Muñoz-Aguilar, R.S.; Etxeberria-Otadui, I.; Teodorescu, R.; Blaabjerg, F., "A Stationary Reference Frame Grid Synchronization System for Three-Phase Grid-Connected Power Converters Under Adverse Grid Conditions," Power Electronics, IEEE Transactions on , vol.27, no.1, pp.99,112, Jan. 2012

[95] Golestan, S.; Monfared, M.; Freijedo, F.D.; Guerrero, J.M., "Dynamics Assessment of Advanced Single-Phase PLL Structures," Industrial Electronics, IEEE Transactions on , vol.60, no.6, pp.2167,2177, June 2013

[96] M.R.Kun, F. Ling,D.Zhao-Yang,W.K. Po, B. Z.Qian, andX. H. Bo, "Dynamic phasor and frequency estimators considering decaying DC components," *IEEE Trans. Power Syst.*, vol. 27, no. 2, pp. 671–681, May 2012.

[97] Fedele, G.; Ferrise, A., "A Frequency-Locked-Loop Filter for Biased Multi-Sinusoidal Estimation," Signal Processing, IEEE Transactions on , vol.62, no.5, pp.1125,1134, March1, 2014

[98] He Wen; Siyu Guo; Zhaosheng Teng; Fuhai Li; Yuxiang Yang, "Frequency Estimation of Distorted and Noisy Signals in Power Systems by FFT-Based Approach," Power Systems, IEEE Transactions on , vol.29, no.2, pp.765,774, March 2014

[99] Kia, S.H.; Henao, H.; Capolino, G.-A., "A High-Resolution Frequency Estimation Method for Three-Phase Induction Machine Fault Detection," Industrial Electronics, IEEE Transactions on , vol.54, no.4, pp.2305,2314, Aug. 2007

[100] Dash, P.K.; Hasan, S., "A Fast Recursive Algorithm for the Estimation of Frequency, Amplitude, and Phase of Noisy Sinusoid," Industrial Electronics, IEEE Transactions on , vol.58, no.10, pp.4847,4856, Oct. 2011

[101] Yong-Hwa Kim; Young-Woo Youn; Don-Ha Hwang; Jong-Ho Sun; Dong-Sik Kang, "High-Resolution Parameter Estimation Method to Identify Broken Rotor Bar Faults in Induction Motors," Industrial Electronics, IEEE Transactions on , vol.60, no.9, pp.4103,4117, Sept. 2013

[102] Hayes M H. Statistical digital signal processing and modelling [M]. John Wiley & Sons, 2009.

[103] So H C, Chan K W, Chan Y T, et al. Linear prediction approach for efficient frequency estimation of multiple real sinusoids: algorithms and analyses[J]. Signal Processing, IEEE Transactions on, 2005, 53(7): 2290-2305.

[104] Y. T. Chan, J. M. M. Lavoie, and J. B. Plant, "A parameter estimation approach to estimation of frequencies of sinusoids," IEEE Trans. Acoust. Speech, Signal Process., vol. ASSP-29, no. 2, pp. 214–219, Apr. 1981.

[105] Pisarenko, V. F. (1973). The retrieval of harmonics from a covariance function.Geophysical Journal of the Royal Astronomical Society, 33(3), 347-366.

[106] Stoica, Petre, Jian Li, and Xing Tan. "On spatial power spectrum and signal estimation using the Pisarenko framework." Signal Processing, IEEE Transactions on 56.10 (2008): 5109-5119.

[107] Kay, Steven M., and Stanley Lawrence Marple Jr. "Spectrum analysis—a modern perspective." Proceedings of the IEEE 69.11 (1981): 1380-1419.

[108] P. A. Thompson, "Adaptive spectral analysis technique for unbiased frequency estimation in the presence white noise," in Proc. 13th Asilomar Conf. Circuits, Syst. Comput., 1979, pp. 529–533.

[109] So H C, Chan K W. Reformulation of Pisarenko harmonic decomposition method for single-tone frequency estimation[J]. Signal Processing, IEEE Transactions on, 2004, 52(4): 1128-1135.

[110] J. F. Yang and M. Kaveh, "Adaptive eigen-subspace algorithms for directionor frequency estimation and tracking," IEEE Trans. Acoust., Speech, Signal Processing, vol. 36, pp. 241–251, Feb. 1988.

[111] Chen L H, Chang S. An adaptive learning algorithm for principal component analysis[J]. Neural Networks, IEEE Transactions on, 1995, 6(5): 1255-1263.

[112] Aboulnasr T, Mayyas K. A robust variable step-size LMS-type algorithm: analysis and simulations[J]. Signal Processing, IEEE Transactions on, 1997, 45(3): 631-639.

[113] Cirrincione, G.; Cirrincione, M.; Herault, J.; Van Huffel, S., "The MCA EXIN neuron for the minor component analysis," Neural Networks, IEEE Transactions on , vol.13, no.1, pp.160,187, Jan 2002

[114] G. Cirrincione and M. Cirrincione, "Linear system identification by using the TLS EXIN neuron," Neurocomputing, vol. 28, no. 1–3, pp.53–74, Oct. 1999.

[115] Ljung L. Analysis of recursive stochastic algorithms[J]. Automatic Control, IEEE Transactions on, 1977, 22(4): 551-575.

[116] Yi Z, Ye M, Lv J C, et al. Convergence analysis of a deterministic discrete time system of Oja's PCA learning algorithm[J]. Neural Networks, IEEE Transactions on, 2005, 16(6): 1318-1328.

[117] Zufiria P J. On the discrete-time dynamics of the basic Hebbian neural network node[J]. Neural Networks, IEEE Transactions on, 2002, 13(6): 1342-1352.

[118] Adali T, Haykin S. Adaptive signal processing: next generation solutions[M]. John Wiley & Sons, 2010.

[119] Murata N, Müller K R, Ziehe A, et al. Adaptive on-line learning in changing environments[J]. 1997.

[120] Murata N, Kawanabe M, Ziehe A, et al. On-line learning in changing environments with applications in supervised and unsupervised learning[J]. Neural Networks, 2002, 15(4): 743-760.

[121] Binying Ye; Cirrincione, M.; Cirrincione, G.; Pucci, M.; Vitale, G., "Improved sensorless scalar control by a PLL tracking rotor slotting effects," Sensorless Control for Electrical Drives (SLED), 2012 IEEE Symposium on , vol., no., pp.1,5, 21-22 Sept. 2012

[122] Chan, Y.T.; Lavoie, J.; Plant, J. B., "A parameter estimation approach to estimation of frequencies of sinusoids," Acoustics, Speech and Signal Processing, IEEE Transactions on , vol.29, no.2, pp.214,219, Apr 1981

[123] Terzija V, Cai D, Stanojevic V, et al. Frequency and power components estimation from instantaneous power signal[J]. Instrumentation and Measurement, IEEE Transactions on, 2011, 60(11): 3640-3649.

[124] So, H. C., Chan, K. W., Chan, Y. T., & Ho, K. C. (2005). Linear prediction approach for efficient frequency estimation of multiple real sinusoids: algorithms and analyses. Signal Processing, IEEE Transactions on, 53(7), 2290-2305.

[125] Klein J D. Fast algorithms for single frequency estimation[J]. Signal Processing, IEEE Transactions on, 2006, 54(5): 1762-1770.

[126] Feng D Z, Zhang X D, Chang D X, et al. A fast recursive total least squares algorithm for adaptive FIR filtering[J]. Signal Processing, IEEE Transactions on, 2004, 52(10): 2729-2737.

[127] Leung S H, So C F. Gradient-based variable forgetting factor RLS algorithm in time-varying environments[J]. Signal Processing, IEEE Transactions o*n, 2005, 53(8): 3141-3150.*

[128] Kay S M. Modern spectral estimation[M]. Pearson Education India, 1988.

[129] F. Chatelin, *Eigenvalues of Matrices*. New York: Wiley , 1993.

[130] U. Helmke and J. B. Moore, "Optimization and dynamical systems," in *Communications and Control Engineering*. London, U.K.: Springer-Verlag, 1994.

[131] B. N. Parlett, "The Rayleigh quotient iteration and some generalizations for nonormal matrices," *Math. Comput.*, vol. 28, pp. 679–693, 1974.

[132] -- *The Symmetric Eigenvalue Problem*. Englewood Cliffs, NJ: Prentice-Hall, 1980.

[133] D. Shafer, "Gradient vectorfields near degenerate singularities," in *Global Theory of Dynamical Systems*. Ser. Lecture Notes in Mathematics 819, Z. Nitecki and C. Robinson, Eds. Berlin, Germany: Springer-Verlag, 1980, pp. 410–417.